The application of Eulerian laser Doppler vibrometry to the on-line condition monitoring of axial-flow turbomachinery blades

by

Abraham Johannes Oberholster

Submitted in partial fulfilment of the requirements for the degree Philosophiae Doctor (Mechanical Engineering) in the Faculty of Engineering, the Built Environment and Information Technology, University of Pretoria, Pretoria

2010

Supervisor: Professor P.S. Heyns

The application of Eulerian laser Doppler vibrometry to the on-line condition monitoring of axial-flow turbomachinery blades

by

Abraham Johannes Oberholster

Supervisor: Professor P.S. Heyns

University of Pretoria

Department of Mechanical and Aeronautical Engineering

Degree: PhD (Mechanical Engineering)

Summary

The on-line condition monitoring of turbomachinery blades is of utmost importance to ensure the long term health and availability of such machines and as such has been an area of study since the late 1960s. As a result a number of on-line blade vibration measurement techniques are available, each with its own associated advantages and shortcomings. In general, on-blade sensor measurement techniques suffer from sensor lifespan, whereas non-contact techniques usually have measurement bandwidth limitations. One non-contact measurement technique that yields improvements in the area of measurement bandwidth is laser Doppler vibrometry.

This thesis presents results and findings from utilizing laser Doppler vibrometry in an Eulerian fashion (i.e. a fixed reference frame) to measure on-line blade vibrations in axial-flow turbomachinery. With this measurement approach, the laser beam is focussed at a fixed point in space and measurements are available for the periods during which each blade sweeps through the beam. The characteristics of the measurement technique are studied analytically with an Euler-Bernoulli cantilever beam and experimental verification is performed. An approach for the numerical simulation of the measurement technique is then presented.

Associated with the presented measurement technique are the short periods during which each blade is exposed to the laser beam. This characteristic yields traditional frequency domain signal processing techniques unsuitable for providing useful blade health indicators. To obtain frequency domain information from such short signals, it is necessary to employ non-standard signal processing techniques such as non-harmonic Fourier analysis.

Results from experimental testing on a single-blade test rotor at a single rotor speed are presented in the form of phase angle trends obtained with non-harmonic Fourier analysis. Considering the maximum of absolute unwrapped phase angle trends around various reference frequencies, good indicators of blade health deterioration were obtained. These indicators were verified numerically.

To extend the application of this condition monitoring approach, measurements were repeated on a five-blade test rotor at four different rotor speeds. Various damage cases were considered as well as different ELDV measurement positions. Using statistical parameters of the abovementioned indicators as well as time domain parameters, it is shown that with this condition monitoring approach, blade damage can successfully be identified and quantified with the aid of artificial neural networks.

Keyterms: Laser Doppler vibrometry, Eulerian measurements, Lagrangian measurements, on-line blade vibration, condition monitoring, non-harmonic Fourier analysis, phase angle trends, finite element modelling, artificial neural networks.

Die toepassing van Euler laser Doppler vibrometrie op die operasionele toestandsmonitering van aksiaalvloei turbomasjinerie lemme

deur

Abraham Johannes Oberholster

Studieleier: Professor P.S. Heyns

Universiteit van Pretoria

Departement Meganiese en Lugvaartkundige Ingenieurswese

Graad: PhD (Meganiese Ingenieurswese)

<u>Opsomming</u>

Die operasionele toestandsmonitering van turbomasjinerie lemme is van uiterste belang met betrekking tot die langtermyn integriteit en beskikbaarheid van hierdie masjiene en is 'n gebied wat al sedert die laat 1960's bestudeer word. Gevolglik is daar 'n aantal operasionele lemvibrasie meettegnieke beskikbaar, elk met sy eie sterk- en swakpunte. In die algemeen word sensors wat direk op die lemme geïnstalleer word, hoofsaaklik beperk deur sensorleeftyd. Nie-kontak tegnieke aan die ander kant, het gewoonlik meetbandwydte beperkings. 'n Nie-kontak meettegniek wat verbeterings bied op die gebied van meetbandwydte, is laser Doppler vibrometrie.

Hierdie proefskrif bied resultate en bevindings aan ten opsigte van die implementering van laser Doppler vibrometrie in 'n Euler verwysingsraamwerk, ten einde operasionele lemvibrasies te meet op aksiaalvloei turbomasjinerie. Met hierdie meetbenadering word die laserstraal gefokus op 'n vaste ruimtelike punt en is metings dan beskikbaar vir die periodes waartydens elke lem deur die laserstraal beweeg. Die eienskappe van die meettegniek word analities bestudeer met behulp van 'n Euler-Bernoulli kantelbalk waarna eksperimentele verifiëring uitgevoer word. 'n Metode om die meettegniek numeries te simuleer word dan aangebied.

Gepaardgaande met hierdie meettegniek is die kort periodes waartydens elke lem blootgestel word aan die laserstraal. Tradisionele seinprosesseringstegnieke is as gevolg daarvan nie geskik om bruikbare lemtoestandsaanwysers te lewer nie. Om frekwensiedomein inligting vanaf sulke kort seine te kry, is dit nodig om van nie-standaard seinprosesseringstegnieke soos nie-harmoniese Fourier analise gebruik te maak.

Resultate vanaf eksperimentele toetse op 'n enkellem toetsrotor by 'n vaste rotorspoed word aangebied in die vorm van fasehoek grafieke wat verkry is deur nie-harmoniese Fourier analise. Deur die maksimum van die absolute van ontvoude fasehoek grafieke te evalueer, word goeie aanduiders van lemtoestandsverswakking verkry. Die resultate word numeries geverifiëer.

Om hierdie toestandsmoniteringtegniek verder te verifiëer, word die metings herhaal op 'n vyf-lem toetsrotor teen verskillende rotasiesnelhede. Verskeie lemskade gevalle word beskou so wel as verskillende Euler meetposisies. Deur statistiese karakteristieke van die bogenoemde aanduiders asook tyddomein aanduiders te evalueer, word dit bewys dat met hierdie toestandsmoniteringtegniek lemskade suksesvol geïdentifiseer en gekwantifiseer kan word deur gebruik te maak van kunsmatige neurale netwerke.

Sleutelterme: Laser Doppler vibrometrie, Euler metings, Lagrange metings, operasionele lemvibrasie, toestandsmonitering, nie-harmoniese Fourier analise, fasehoek grafieke, eindige element modellering, kunsmatige neurale netwerke.

Acknowledgements

First and foremost, I thank God for the opportunity to have done this research. I could easily double the number of pages in this document if I had to write about all the grace and favour I received from Him during this project.

I also wish to thank the following people and companies for their contributions to this project:

- Professor Stephan Heyns for his guidance and drive for excellence
- Mark Newby (*Eskom Research and Innovation Division*)
- Kobus Babst, Saluja Ramluckun and Gladman Mkwai (*Eskom Kendal Power Station*)
- Professor Schalk Els, Michael Thoresson and Burkhardt Freyer (*University of Pretoria*)
- Kris Peeraer (*Polytec*)
- Kobus van der Westhuizen (*Ideas Solutions*)
- Professor Steve Vanlanduit (*Vrije Universiteit Brussel*)
- Annamarie Bezuidenhout, Marietjie Calder (*University of Pretoria*)
- The Turbomachinery Technogroup
- Esteq Engineering

Furthermore, I want to thank the following people for their personal support:

- My lovely wife, Karin Oberholster
- My parents, Jan and Magdaleen Oberholster
- Mark and Christina Burger
- Clive and Wendy Willoughby
- Werner and Cindy Steyn
- Dr. Amanda Kotze-Streicher
- Caryn Seago
- All my other friends at Harvest Church International

"The fear of the LORD is the beginning of knowledge" (Proverbs 1:7)

Table of contents

Glossary

Abbreviations

Abbreviation	*Description*
AC	Alternating Current
ADC	Analogue to Digital Converter
AIC	Akaike Information Criterion
ANN	Artificial Neural Network
AR	Autoregressive
ARMA	Autoregressive Moving Average
BLEP	Blade Leading Edge Profile
BPF	Blade Pass Frequency
CLSF-IO	Combined Non-Linear Least Squares Frequency Method On Input Output Spectra
CSLDV	Continuous Scanning Laser Doppler Vibrometry
DC	Direct Current
DEN	Denominator
ELDV	Eulerian Laser Doppler Vibrometry
ESPI	Electronic Speckle Pattern Interferometry
EV	Eigenvector
EVR	Eulerian Vibration Response
FBG	Fibre Bragg Grating
FEM	Finite Element Model
FFT	Fast Fourier Transform
FOD	Foreign Object Damage
FPE	Final Prediction Error
FRF	Frequency Response Function
HCF	High Cycle Fatigue
HFA	Harmonic Fourier Analysis
HI	Holographic Interferometry
HP	High Pressure
INVE	Iterative Noise Variance Estimation
LCF	Low Cycle Fatigue
LDV	Laser Doppler Vibrometer / Vibrometry

LP	Low Pressure
LVR	Lagrangian Vibration Response
LVRM	Lagrangian Vibration Response Matrix
MAUPAT	Maximum Absolute Unwrapped Phase Angle Trend
MBLEC	Mean Blade Leading Edge Curve
MDL	Minimum Description Length
MPC	Multi-Point Constraint
MUSIC	Multiple Signal Classification
MW	Megawatt
mW	milliwatt
NExT	Natural Excitation Technique
NHFA	Non-Harmonic Fourier Analysis
NOM	Nominator
ODS	Operational Deflection Shape
PI	Proportional-Integral
PPCRE	Predicted Percent Reconstruction Error
PPR	Pulses-Per-Revolution
PSD	Power Spectral Density
RBVC	Rigid Body Velocity Component
RC	Rotor Circumferential
RMS	Root-Mean-Square
RPM	Revolutions Per Minute
SCC	Stress Corrosion Cracking
SLDV	Scanning Laser Doppler Vibrometer / Vibrometry
SNR	Signal to Noise Ratio
TLDV	Tracking Laser Doppler Vibrometry
TOA	Time-Of-Arrival
UPA	Unwrapped Phase Angle
VI	Virtual Instrument

Symbols

Symbol	*Description*
A	ELDV measurement position
a	Fourier cosine coefficient

B	ELDV measurement position
b	Blade number
C	Cosine operator
c	Scanning speed
c_{ref}	Reference scanning speed
c_{max}	Maximum scanning speed
D_b	Blade-specific damage level [mm]
d	Fourier sine coefficient
E_j	jth modal constant
F	Force
F_b	Simulated blade force
f	Frequency
f_{actual}	Actual frequency
$f_{aliased}$	Aliased frequency
f_{NQ}	Nyquist frequency
f_R	MAUPAT reference frequency
f_s	Sampling frequency
Δf_{min}	Minimum required ELDV frequency resolution
Δf	Frequency resolution
G	NHFA signal approximation
g	Probe group size
H	Mobility FRF amplitude
h	Vector-loop diagram vector number
J	ELDV RMS run-down peak number
j	Mode / natural frequency number
k	Scanning speed ratio
l	Cantilever beam length
m	Harmonic number
N	Sample length
N_k	Interpolation sample length

N_{ref}	Reference sample length
n	Sample number
P_b	Average nozzle back-pressure waveform
q_j	jth generalized modal coordinate
$\bar{R}_1$	MBLEC offset vector
$\bar{R}_2$	Relative MBLEC measurement position vector
$\bar{R}_3$	Laser orientation vector
$\bar{R}_4$	Laser offset vector
$\bar{R}_5$	Absolute MBLEC measurement position vector
$\bar{R}_h$	Vector-loop diagram vector
R_h	$\bar{R}_h$ amplitude
r	Angular ELDV measurement radius
S	Sine operator
t	Time
t_0	Zero-based time vector
t_N	Sample time span
Δt	Time increment
$\hat{V}_{L,c_{ref}}$	LVRM
$\hat{V}_{L,\psi_{ref}}$	Angular LVRM
v_E	Eulerian vibration velocity
$\vec{v}_E$	EVR vector
v_L	Lagrangian vibration velocity
$\vec{v}_L$	LVR vector
v_{RB}	RBVC
W_j	jth characteristic function
w_E	Eulerian vibration displacement
w_L	Lagrangian vibration displacement
X	X-axis

x_E	Eulerian measurement position
x_L	Lagrangian measurement position
Δx	Measurement position increment
Y	Y-Axis
y	Time signal
Z	Z-axis

Greek symbols

Symbol	*Description*
β_j	j[th] modal root
δ	$\bar{\varepsilon}$ offset
$\bar{\varepsilon}$	Rotor order vector
Φ	NHFA detected phase angle
ϕ	Phase angle
ϕ_d	Damped phase angle
η_h	$\bar{R}_h$ angle
ϑ	Angular measurement range
φ_E	Eulerian angular measurement position
φ_L	Lagrangian angular measurement position
μ_b	Pressure waveform normalization constant
θ	Rotor angle
σ	Standard deviation
σ_{CORR}	Correlation coefficient standard deviation
σ_{MAUPAT}	MAUPAT standard deviation
σ_{RMS}	RMS standard deviation
$\tilde{\sigma}_{MAUPAT}$	Mean MAUPAT standard deviation
τ	Total signal time span
ϖ	Arbitrary frequency
ϖ_0	Signal fundamental frequency
ϖ_{ref}	NHFA reference frequency
$\Delta\varpi$	Frequency offset

Ω_j	j^{th} modulation frequency
$\overline{\omega}$	ω_1 estimate vector
ω_d	Damped natural frequency
ω_j	j^{th} natural frequency
ω_1	Blade first bending mode frequency
$\omega_{1,est}$	ω_1 estimate
$\overline{\Psi}$	Rotation speed vector
ψ	Rotor speed
ψ_{ref}	Reference rotor speed
ζ	Structural damping coefficient

Chapter 1 Introduction and Literature Study

1.1 Introduction

Turbomachinery are critical to various processes and their applications range from micro-turbines to steam turbines and aircraft turbines. Possessing large amounts of kinetic energy, the failure of industrial turbine blades during operation are typically quite severe with regards to subsequent secondary damage. In the recent past, a single blade failure on a steam turbine rotor resulted in the destruction of the entire turbo-generator train leading to a large financial loss (Spicer, 2003a; Spicer, 2003b). It is therefore of great importance to monitor the health of turbomachinery on-line in order to ensure the long term health and availability of these machines.

To monitor blade health in an on-line fashion, it is useful to obtain on-line blade vibration information. Various techniques exist to accomplish this, the two most common techniques using blade strain and blade tip Time-Of-Arrival (TOA) signals respectively. Strain gauges are however limited in life span due to the harsh operating environment whereas a large number of sensors are required to obtain sufficient measurement bandwidths when the TOA technique is implemented. Sufficient sensor life span as well as measurement bandwidth are required for long term, accurate blade condition monitoring. For this reason, laser Doppler vibrometry is a very promising measurement technique. Specifically, Eulerian Laser Doppler Vibrometry (ELDV) enables the high bandwidth vibration measurement of an entire row of blades using a single sensor. It is this technique that this thesis is concerned with, focussing on its application to the condition monitoring of free standing axial-flow rotor blades.

ELDV involves the laser beam being focussed at a fixed point in space and measurements are available for the short periods during which the rotor blades sweep through the beam. Since these sample periods are at most inversely proportional to the Blade Pass Frequency (BPF), frequency domain information is available only for a frequency resolution equal to the BPF using conventional signal processing techniques. This disqualifies these signal processing techniques for useful information pertaining to blade condition monitoring. In order to obtain useful information, Non-Harmonic Fourier Analysis (NHFA) is employed.

The thesis is divided into five chapters. The first chapter contains a literature study focussing on topics such as the causes and influences of blade vibration as well as blade failure modes. Several damage detection parameters are also considered along with different on-line blade vibration measurement techniques and systems.

Thereafter some modelling and experimental testing issues are investigated as well as practical issues with regards to laser Doppler vibrometry. Different signal processing techniques are also considered.

The second chapter deals with an analytical study of the ELDV technique applied to a traversing and vibrating cantilever beam using the Euler-Bernoulli continuous beam formulation. The results are verified experimentally after which an approach is formulated for simulating ELDV numerically in a Finite Element Model (FEM) environment.

Chapter 3 presents results from experimental ELDV and Tracking Laser Doppler Vibrometry (TLDV) testing on a single-blade test rotor at a single rotor speed. Incremental damage is induced in the blade and it is shown that Maximum Absolute Unwrapped Phase Angle Trends (MAUPATs) from NHFA around various reference frequencies are good indicators of blade health deterioration. The results are verified numerically.

The next chapter presents experimental ELDV and TLDV results obtained from a multi-blade rotor at different rotor speeds. Considering various damage cases on multiple blades, Artificial Neural Networks (ANNs) are successfully trained on the statistical properties of MAUPATs as well as two time domain parameter trends. It is shown that measurements from multiple ELDV measurement positions are advantageous.

Chapter 5 presents the conclusions reached in this thesis and proposes work for further studies.

1.2 Blade vibration

1.2.1 Operational blade excitation

Turbine blades are predominantly subjected to periodic nozzle excitation distributed along the blade lengths (Rao and Vyas, 1985; Irretier, 1988; Rieger, 1988). The load on a rotating blade can thus be described as a Fourier-series, the various harmonic coefficients of which are affected by the unevenness of the nozzle spacing as well as partial (i.e. uneven) steam admission. Rao and Vyas (1985) consider three components of the forcing function namely in the rotor-axial and tangential directions as well as a moment acting on the blade.

Additional blade forces result from flow instabilities (Gadala and Byrne, 1986). The flow instabilities are manifested as white random noise, resulting in the excitation of blade natural frequencies.

Ziegler (1994) groups operational blade vibration into resonance, stochastic response and flutter. Resonance vibration occurs when one of the blade natural frequencies coincides with one of the harmonics of rotation speed whereas stochastic vibration is a result of stochastic flow excitation. Ziegler attributes flutter to the coupling of blade natural vibration modes and flow forces.

Kielb and Abhari (2003) present a report of the independent and simultaneous structural and aerodynamic damping effects in a single stage High Pressure (HP) turbine disk at engine-level rotation speeds. According to these two authors, damping in a turbine is one of the most important factors influencing blade forced response and flutter. They identify the three major sources of damping in a rotating blade as material damping (which they state to be negligible), structural damping and aerodynamic damping. Performing tests on the HP turbine disk at different conditions using blade-mounted strain gauges as transducers and blade-mounted piezoelectric actuators, Kielb and Abhari (2003) reach a number of important conclusions. A very interesting observation is that structural damping in the turbine disk decreases as rotation speed increases. The authors attribute this phenomenon to the fact that as the centrifugal load on a rotating blade increases, energy dissipation as a result of friction between the blade/hub interface decreases. Kielb and his co-worker also conclude that aerodynamic damping forms a major part of total blade damping during rotation.

1.2.2 Rotational effects

The most intuitive effect of rotation on a structure is that of rotational stiffening as a result of centrifugal forces. From experimentation on a single-blade rotor, Fan et al. (1994) note that rotational stiffening causes the blade natural frequencies to increase in a nonlinear way, since the blade centrifugal force is proportional to the square of the rotation speed.

Rotating structures are furthermore subjected to additional forces including gyroscopic forces, rotor-stator rub forces, electromagnetic forces, unsteady aerodynamic forces and time-varying fluid forces (Ewins, 2000:80). All of these forces can destroy the symmetry of the rotor system matrices pertaining to the system equations of motion. Being velocity-dependent, gyroscopic effects introduce a skew-

symmetric component in the damping matrix of the system. Gyroscopic forces furthermore cause the natural frequencies of the rotor to be dependent on rotation speed. These frequencies either increase or decrease with speed, depending on whether the corresponding mode shape is a forward or backward whirl mode.

Rao and Sreenivas (2003) state that the forward whirl mode is furthermore affected by centrifugal stiffening effects, whereas the backward whirl mode is additionally influenced by spin softening. Spin softening is another rotational phenomenon where the rotor stiffness matrix becomes speed-dependent (Nikolic et al., 2007).

Sreenivasamurthy and Ramamurti (1981) numerically investigate the Coriolis effect on the vibration of a single rotating blade. In their investigation, the authors include rotational stiffening effects. By varying the rotation speed, stagger angle and aspect ratio of the blade, the influence of the Coriolis effect is observed to change. The authors observe that the Coriolis effect causes the first flapwise blade frequency to decrease as rotation speed increases. Furthermore, the blade aspect ratio determines whether the first torsional blade frequency increase or decrease due to Coriolis acceleration. The authors also found the blade stagger angle to largely influence the extent of the Coriolis effect on the blade frequencies. The authors conclude their article in stating that in general, the Coriolis effect can be ignored for cases where the first blade bending frequency is higher than the rotation frequency. However when the rotation frequency is very high and also higher than the first blade natural frequency, it is recommended to include Coriolis effects.

1.2.3 Blade manufacturing tolerances

1.2.3.1 Blade roots

Singh (1998) discusses the effects of dimensional tolerance of blade roots on the maximum stresses in the blade roots. The dimensional tolerance considered by the author is the gap between the blade root attachment and the supporting structure or rotor. Results show that the maximum stress in a blade root increases as the gap increases. Since blades can be considered as cantilever beams, which means that their dynamic responses is very sensitive to their individual boundary conditions, this factor will influence the blade vibration responses, as confirmed by Bhat et al. (1996).

Orsagh and Roemer (2002) state that connection stiffness within blade-root interfaces and blade-tiewire interfaces, centrifugal effects and thermal effects influence the accuracy and effectiveness of modal test data taken from bladed disk assemblies. The

authors note that differences in measured frequencies of substructures such as blade groups can be anticipated due to dimensional tolerances, manufacturing defects, material processing and installation procedures. The effect of these differences is manifested as scatter of natural frequencies about a mean value. According to the authors, scatter of 5% is normally considered acceptable among the manufacturing community for Low Pressure (LP) steam turbine blades. Orsagh and Roemer note that if an assembly is tested with blade fixity problems such as loose blade-root interfaces (which is an example of dimensional tolerance), the bladed disc natural frequencies will be lower than for rigidly fixed blades. Looseness will also create structural nonlinearities. However according to them, blade-root looseness is eliminated by centrifugal forces during operation to ensure tight blade-root interface fits, making blade and disk essentially an integral structure.

Bhat et al. (1996) also note that due to manufacturing tolerances, some variation can occur with regards to blade natural frequencies of a turbine. Impact test measurements were taken on blades of two stages of a LP turbine of a 235 MW turbo-generator set. Some scatter was observed in these measurements with bands of 76-85 Hz, 125-140 Hz and 155-170 Hz for the first three modes. The authors note that the scatter is probably due to non-uniformity in root fixity and aerofoil cross-section.

1.2.3.2 Mistuning

Afolabi (1988) discusses the modal characteristics of turbomachinery blades in multi-stage rotors. He investigates the effect of inter-stage coupling on the modal characteristics of turbine blades. The author refers to experiments showing that the vibration characteristics of an isolated blade differ a lot from blades of bladed disc assemblies: When a number of identical blades are assembled on a common disc, the previously isolated blade modes are transformed into spectral bands of groups of the same number of modes. Most of these modes are double modes. It is further noted by Afolabi that all the blades within an assembly are not identical due to manufacturing tolerances and are referred to as being mistuned. Although the resulting differences between blades are very small, the effects of mistuning cannot be ignored when coupling (as provided by the blade disc) exists among the blades. If there is mistuning involved among the blades in the assembly, there is a change in the modal characteristics. This has the effect of the system having very high modal densities within the spectral bands. Resulting uneven distribution of blade amplitudes of a given mode shape may cause some blades to possibly fail prematurely due to the high amplitudes of such blades.

Hollkamp and Gordon (2001) give an in-depth discussion on the topic of bladed disc modal analysis and concur on a number of Afolabi's findings. They note that periodic structures are "notoriously sensitive" to mistuning. A number of difficulties are involved with bladed disc modal analysis. Also, multiple inputs and high-resolution techniques are required to separate repeated modes. Thus these structures have multiple closely spaced frequencies, making the task of mode shape estimation extremely difficult. They state that slight variations in blades mistune individual blade natural frequencies and affect the entire system.

1.3 Blade damage and failure modes

Rieger (1988) discusses several important blade failure types and their causes pertaining to steam turbines. The author note that from electrical utility records it is shown that approximately 30% of all steam turbine forced outages can be attributed to blade problems (Rieger, 1988:453). According to the author there are four aspects that influence the life span of a blade. Two of these relate to the magnitudes and distributions of steady mean and alternating stresses. According to Rieger (1988:455) both of these have maximum values at certain locations such as among others, the blade root-disk attachment region. Mathwin (2004) confirms this in stating that cracking in steam turbine blades with fir-tree roots mostly occurs in the region of the roots' top serration. Further literature sources (Gadala and Byrne, 1986; Mazur et al., 2008) also refer to incidents involving the failure of LP turbine blades as a result of crack growth at the blade-root top serration.

Rieger (1988) notes that at each of the locations he mentions, the mean stress value depends on centrifugal and steam loading conditions. Visser (2004) also refers to centrifugal loading as being one of the greatest influences on blade fatigue life. According to Rieger (1988:455) alternating stresses in turbine blades result from dynamic steam stimuli and the corresponding modal response from the entire blade group involved.

Another influence of great importance is the effect of thermal stresses (Visser, 2004; Boutarek et al., 2008). This relates mainly to the rates of heating up and cooling down of turbine blades during run-ups and run-downs respectively.

A large number of possible crack initiation and failure mechanisms pertaining to turbomachinery blades exist. The following sub-sections highlight some of the more predominant mechanisms.

1.3.1 Fatigue

Fatigue in turbine blades is classified as either High Cycle Fatigue (HCF) or Low Cycle Fatigue (LCF) (Rieger, 1988:456). HCF is normally associated with high mean stress levels and moderate dynamic stresses whereas LCF is associated with fewer load cycles of much larger strain ranges. LCF is furthermore frequently associated with corrosion or high temperature. Possible causes of fatigue listed by Rieger (1988:481) are unsymmetrical stage steam flow, nozzle wake excitation resonance, partial admission of steam, torsional transients, generator electrical faults and excessive condenser pressures.

According to Bhat et al. (1996), the main cause of turbine blade failure is vibration-related fatigue. Although turbine blades are designed to have natural frequencies not coinciding with operational frequencies, they still experience resonance excitation during run-up and run-down of the turbine.

Fatigue can furthermore be exacerbated by other factors. Corrosion assisted fatigue is "probably the major source of steam turbine blade fatigue failures" according to Rieger (1988) and confirmed by Beaumont (2004). Rieger (1988:459) notes that corrosion assisted fatigue may occur where large dynamic stresses applied with high steady stress are present in a corrosive environment.

In aero-engines, the interaction of both creep and fatigue mechanisms is one of the main causes of blade failure (Infante et al., 2009).

1.3.2 Stress-corrosion

The mechanism of stress-corrosion is a combination of dynamic stress and a corrosive medium (Boutarek et al., 2008; Rieger, 1988). Rieger (1988:458) does however note that the presence of dynamic stress is not necessarily a requirement for the occurrence of a stress-corrosion failure. According to Beaumont (2004), Stress-Corrosion Cracking (SCC) usually occurs in steam turbine blades of low alloy materials in a wet steam environment at elevated temperatures. Beaumont notes that SCC can occur even when the steam has good chemical qualities.

1.3.3 Foreign object damage

Foreign Object Damage (FOD) occurs when a foreign object impacts a blade during operation. According to Tappert et al. (2001:3287) such an impact momentarily affects the particular blade's vibration, resulting in transient vibration of the blade. Depending on the magnitude of the impact, plastic deformation of the blade may also occur.

Infante et al. (2009) note that FOD due to the impact of small debris results in blade "nicking". These "nicks" then act as stress raisers, which are prone to crack initiation. They furthermore state that FOD tends to compromise the rotor mechanical balance which may lead to aerodynamically induced blade flutter.

1.3.4 Flutter

According to King et al. (2006), blade flutter is a self-excited dynamic instability that may, among others, arise from cracked or damaged blades. It manifests itself as an acoustic phenomenon and as a result may not propagate through the turbine support structure. Traditional monitoring methods such as bearing vibration monitoring may as a result not be sufficient for detecting blade flutter.

Mazur et al. (2006) report on the failure of a number of last-stage LP turbine blades of a geothermal unit. The main contributor to the HCF failure of the blades was identified as unstable flow excitation or stall flutter. They state that flow-induced blade oscillations are in general more prominent in the last 10% of the blade length. They also note that aeroelasticity phenomena with largely increased vibratory stresses in blades can occur while operating the turbine at low load/ low vacuum conditions.

In another paper, Mazur et al. (2008) investigate the failure of last stage LP turbine blades of two 660 MW units. Again one of the main contributors the HCF failure of the blades was flutter that occurred at low load/ low vacuum operational conditions.

1.3.5 Transient load events

Mazur et al. (2008) studied the failure of last stage LP turbine blades. They note that transient load events on the generator due to other sudden transient events on the electricity grid induced transient torsional vibrations of the rotor. This in turn excited the first tangential mode shape of the blades, resulting in high quantities of cycles of high vibratory stresses in the blades.

1.4 Blade health indicators

1.4.1 Natural frequencies

Wu and Huang (1998) consider the vibration of a cracked rotating blade. They consider a single rotating blade that is mathematically modelled as an Euler's beam with constant cross section. Only transverse bending deflection is considered in the paper. The equations of motion were derived by the authors by looking at crack-released energy in conjunction with weighted residuals. Wu and Huang focussed on the effect of crack size and location on the first four natural frequencies of the modelled blade. From their test results, the authors draw a number of conclusions. Firstly, they conclude that the dynamic characteristics of the rotating blade are significantly influenced by the location of the crack. The effect of this is that the sensitivity of blade natural frequency shift to damage increases as the crack is located closer to the blade root. This is Wu and Huang's (1998) second conclusion along with the fact that at some locations for specific modes, the natural frequency is unchanged. They call these locations inflection points, which are more commonly known as nodal points. Their third conclusion is that as the crack depth increases, the natural frequencies decrease. Wu and Huang (1998) finally conclude that natural frequencies and deflective responses of blades are potential indices for crack identification. They advise that in order to develop a sophisticated on-line crack detection technique, quantitative studies of these indices must be studied. In other words, the relationship between crack severity and its effect on blade natural frequencies and deflections need to be established in order to develop such a system.

Yang et al. (2006) show experimentally that decrease in natural frequencies of a turbine blade is related to damage. Their aim was to determine whether damage in a blade could cause sufficient decrease in any natural frequency of the blade for that natural frequency to be close to resonance. The authors experimentally and numerically performed tests on a single clamped blade of the tenth stage of a nuclear power station LP turbine. They induced damage close to the blade root in the form of a crack in a controlled manner, each level for which they performed a modal analysis on the blade.

Kumar et al. (2007) consider the on-line damage detection of rotating turbine blades. From strain energy and kinetic energy equations of a rotating Timoshenko beam with taper and twist, they consider the reduction in a specific frequency of a rotating blade as a health residual which can be tracked for purposes of condition monitoring. The

authors go on to discuss the use of thresholds to make the damage detection technique using the residual more robust.

Maynard et al. (2001) focus on the use of shaft torsional measurements to monitor changes in global blade natural frequencies for damage detection.

1.4.2 Damping

Ziegler (1994) states that the "damping constant" relating to blade vibration is dependent on operational variables such as friction between blade and flow medium and excitation force amplitude. It is also dependent on the blade's material damping but more importantly on the friction between the blade root and the shaft, implying its feasibility as use of a blade damage indicator. Ziegler does however note that determining this parameter from in-service measurements is not straightforward.

Von Flotow et al. (2000) state that damping may be a possible blade damage indicator.

1.4.3 Amplitude

Wu and Huang (1998) state that vibration response amplitudes are affected by damage. Von Flotow et al. (2000) also consider vibration amplitude changes as a possible blade damage indicator.

King et al. (2006) consider the amplitude of rotor tracked orders to be indicative of among others, blade damage.

1.4.4 Phase angle

Changes in natural frequencies, mode shapes and damping values only become noticeable at high damage levels (Hueck, 2004; Jacobs and De Roeck, 2003). One parameter that is a very sensitive damage indicator is vibratory phase angle change, as shown by Jacobs and De Roeck (2003) from dynamic testing on a stationary concrete beam. In comparison with the abovementioned parameters, Jacobs and De Roeck find phase angles to already show significant changes at low damage levels. With regards to rotating blades, the sensitivity of the natural frequency shift to damage in a blade decreases with an increase in rotor speed (Wu and Huang, 1998; Yang et al., 2006). This makes vibratory phase angle change a promising damage indicator for rotating blades.

According to King et al. (2006) the monitoring of the phase and amplitude of a tracked engine order from shaft vibrations can also provide information on crack propagation in turbine blades.

1.4.5 Operational modal analysis

Various literature sources deal with using modal analysis to identify damage in a structure. Modal analysis seeks to characterise a mechanical system in terms of its various vibration modes. In classical modal analysis, measured responses to known input forces render the Frequency Response Functions (FRFs) for this purpose. However in operating machinery (especially turbines) it is difficult to measure all the input forces and hence it is necessary to estimate the modal parameters by other means.

Cauberghe et al. (2003) present the Combined Non-Linear Least Squares Frequency Method On Input Output Spectra (CLSF-IO) to estimate modal parameters from output-only data. The Gauss-Newton method is used to solve the non-linear optimization problem. Cauberghe and his co-authors also briefly draw a comparison between the CLSF-IO method and the Auto Regressive Moving Average (ARMA) method in terms of unknown force estimation.

Shen et al. (2003) review the theoretical aspects of the Natural Excitation Technique (NExT) and also present a frequency domain poly-reference scheme for modal identification using Power Spectral Density (PSD) and cross spectral density functions.

Simani (2005:204) and Brincker et al. (1996:3) refer to a number of order selection indicators. These include the Final Prediction Error (FPE), Akaike Information Criterion (AIC), Minimum Description Length (MDL) and Predicted Percent Reconstruction Error (PPCRE). FPE presents a trade-off between residue variance and model parameter number according to Brincker et al. (1996). Brincker and his co-workers select an ARMA model for an offshore platform based on the lowest FPE.

1.5 Blade vibration measurement techniques

Al-Bedoor (2002) classifies blade vibration measurement techniques as direct or indirect, referring to the transmission path between sensor and blade. What makes

direct techniques attractive is that the transmission path is minimal, thereby reducing signal noise pollution.

1.5.1 Strain gauges

The traditional and popular method of measuring blade vibrations involves strain gauges installed on individual blades. The advantage of this method is that individual blade vibration measurements can be performed over an entire revolution of the rotor. However, this method also has quite a number of drawbacks.

1. Sensor life span

   Kadoya et al. (1995:486) highlight a number of factors reducing the life span of strain gauges operating in steam environments. These include high centrifugal forces and high temperature. Another influence is of course erosion (Al-Bedoor, 2002).

2. Signal transmission

   Transmission of signals from the strain gauges is perhaps the biggest problem associated with the technique. Slip ring assemblies can be used for this purpose, although these present their own problems in terms of life span due to wear as well as installation problems on a large rotor such as a steam turbine. Signal transmission can also be accomplished with radio-telemetry systems, although they are costly and time consuming to set up (Beauseroy and Lengelle, 2007). Due to the presence of rotor seals, grooves furthermore need to be machined in the shaft in order to accommodate the wires leading from the strain gauges (Gloger, 1988:2; Kadoya et al., 1995:486; Fangman et al., 1967:21A).

3. Number of sensors

   The number of sensors that need to be installed to monitor a single turbine rotor stage is large. However, Oberholster and Heyns (2006) show that damage detection on a rotor can be accomplished using less than one sensor per blade by exploiting the blade global mode shapes phenomenon.

4. Rotor interference

   Beauseroy and Lengelle (2007) state that strain gauge instrumentation often interferes with the aerodynamic and mechanical properties of the rotor of concern.

1.5.2 Blade tip TOA

Blade tip TOA is a non-contact blade vibration measurement technique. This technique utilizes a number of stationary probes mounted on the enclosure of a

specific blade row. The probes sense the proximity of passing blades, which makes it possible to measure the times at which each blade tip passes one of the probes. A once per revolution shaft speed sensor is used for the purpose of relating these signals to designated blade numbers (Zielinski and Ziller, 2000:847). Figure 1 shows a typical system setup consisting of two proximity probes and a shaft speed sensor.
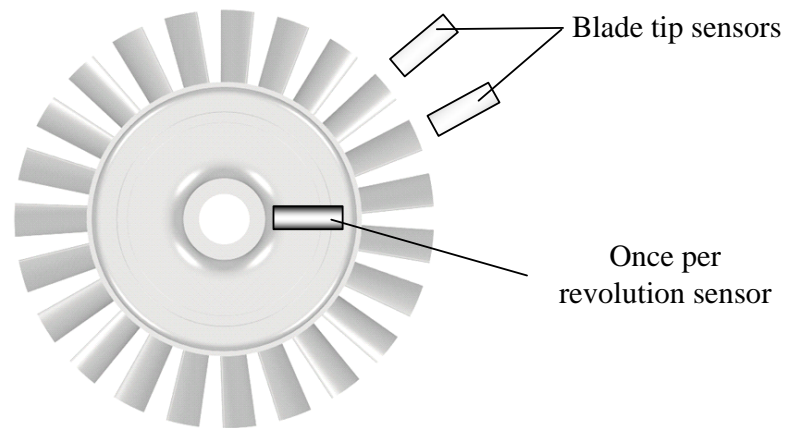

Figure 1: Typical blade tip TOA measurement system setup

Drawing an analogy of a TOA system to a signal processing frame of reference, such a system can be seen as an "optical" Analogue to Digital Converter (ADC) of blade position. Another analogy can be drawn to that of a shaft encoder: Taking measurements utilizing a shaft encoder can be seen as taking TOA measurements on blades with zero lengths.

According to Zielinski and Ziller (2000:853) the shape and magnitude of a resonance curve measured using TOA, is influenced by the exciting engine order, the circumferential position of the probes as well as their spacing.

Beauseroy and Lengellé (2007) introduce a system consisting of a number of individual groups of regularly spaced optical probes for TOA measurements. By simultaneously sampling the signal using different sampling frequencies (as a result of different probe spacing for each group) they are able to analyze multi-component blade vibration signals over a wide frequency bandwidth. According to Beauseroy and Lengellé (2007) the limitation of typical TOA systems is the analysis of blade vibration at only a single frequency. Using two groups of probes, the authors give the following relation to the maximum dynamic range of measurement:

$$\text{Dynamic range} = \frac{g_1 \cdot g_2}{2}\psi$$

with g_1 and g_2 the number of probes in each respective group of sensors and ψ the rotation frequency of the rotor. This implies a large number of probes if a high bandwidth is required at especially low rotation speeds, a shortcoming of TOA that is also implied by Watkins and Chi (1989).

Heath and Imregun (1998) go further to state that this may lead to an impractical number of probes in terms of installation costs. This forces the use of a low number of sensors that in turn necessitates indirect amplitude and frequency extraction techniques from the data. As a result one of the drawbacks of the TOA technique is that the interpretation of the TOA signals is complicated.

1.5.2.1 Probe Types

Zielinski and Ziller (2000) compare optical probes and capacitive probes as sensors and note that the latter are inferior to the former in terms of amplitude resolution and as a result also Signal to Noise Ratio (SNR).

Drumm and Haase (2000) state that light cannot easily be used to measure blade tip clearance or radial vibration (note that the authors are not referring to laser light here). In comparison to capacitive probes, they discuss a number of shortcomings of light probes. One of these is the fact that light probes tend to be bulky. This makes it difficult to place a number of probes in close proximity of each other, which in turn limits the measurement bandwidth of the system. On the other hand, multiple capacitive probes can be closely spaced. According to the two authors, a substantial problem with light is contamination from debris that blocks the light. Although contamination has an effect on the tip clearance measurements by a capacitive sensor, there is no effect on the TOA measurement. Another problem with light probes is their operating temperature limit. According to Drumm and Haase (2000), capacitive sensors can be made for very high temperature applications. With regards to the SNR as mentioned by Zielinski and Ziller (2000), Drumm and Haase refer to the HiBand system from ExSell instruments. This system makes use of a Direct Current (DC) biasing technique in the probe amplifier to overcome this problem.

Kadoya et al. (1995) focus on the blade tip TOA measurement application of laser probes. Aono et al. (1985) make use of laser probes due to their good frequency characteristics in comparison to inductive and capacitive probes.

1.5.2.2 Aliasing

Zielinski and Ziller (2000:849) note that aliasing occurs in a TOA system because the most blade vibration frequencies are above the Nyquist frequency (f_{NQ}) given as:

$$f_{NQ} = \frac{f_s}{2} = \frac{g\,\psi}{2}$$

<div align="right">**Equation 2**</div>

with f_s being the sampling frequency and g the number of circumferentially equally spaced probes.

Balda (2000:680) gives the equation for calculating an aliased frequency ($f_{aliased}$) as:

$$f_{aliased} = f_{actual} - f_s \cdot \text{round}\left(\frac{f_{actual}}{f_s}\right)$$

<div align="right">**Equation 3**</div>

with f_{actual} being the actual frequency that is aliased.

A problem occurs when f_{actual} is an integer multiple of f_s as this will result in $f_{aliased}$ being zero. This means that the specific frequency will not be visible in the spectrum. This will not necessarily be a cause of concern during running up or running down of a turbine, as the aliased frequency can be tracked as a zigzag line in waterfall plots of the measured spectra (Zielinski and Ziller, 2000:849). This is because the sampling frequency varies with the shaft rotation speed and as a result, the aliased frequency also varies as can be concluded from Equation 3. However it may present a problem when this occurs at a steady operating speed. But according to Balda (2000:681) estimates of the resonance frequencies are available from the blade manufacturers, which mean that the TOA system can be designed accordingly.

1.5.2.3 Probe configuration

Zielinski and Ziller (2000) discuss the capabilities of different probe configurations. One of the main considerations with regards to selecting the number of probes relates to aliasing as discussed in Section 1.5.2.2. For three probes, engine order multiples of 3 will not be visible while as for five probes, all engine order multiples of 5 will be invisible. The authors note a shortcoming of using three probes which is that the

measured amplitude of the first torsional blade mode is about 20% smaller than what it actually is. They attribute this to the radial displacement of the rotor axis at higher speeds. Speed-synchronous vibrations can be measured using two probes only with the requirement that "the resonances must be traversed completely (Zielinski and Ziller, 2000:852). A single or average spectrum of all the blades can be obtained using a single probe as well. The assumption here is that all the blades are vibrating at the same amplitude and with a "fixed interblade phase difference" (Zielinski and Ziller, 2000:854). The authors mention in their conclusion that using four probes, comprehensive data on all speed-synchronous vibrations can be obtained.

1.5.2.4 Assumptions

Zielinski and Ziller (2000:848) make the same assumptions that blade tip motion caused by vibration is much slower than that caused by rotation, and that these vibrations are moderately damped. They also ignore any interactions among blades.

1.5.2.5 Signal processing

One of the practical issues of using a proximity probe in TOA measurements is to choose the thresholds that will define when a blade has arrived at and passed a sensor (Newby, 2004). Zielinski and Ziller (2000:848) advise to make use of what they call "constant fraction triggering" on the falling edge of a signal measured with a capacitive probe to define the time of a blade passing the sensor. They note that this is necessary to make the trigger timing largely independent of signal amplitude, which varies with tip clearance.

1.5.3 Pressure signals

Aretakis et al. (1998) use computational fluid dynamics calculations to derive unsteady pressure signals of blade tips sensed by a stationary transducer. These signals are then used to identify certain blade faults. The paper focuses on typical blade damage as a result of FOD. It does not seem that the authors considered blade vibration as part of their signal derivations. Aretakis and his co-workers make use of what they call "enveloping" of the power spectra of the pressure signals for signal classification. Basically what this means is that they use only the values of multiples of rotation speed for classification. Using ANNs, the authors are able to discern between different faults very successfully. In essence, what Aretakis et al. (1998) describe is a variation on blade tip TOA systems.

1.5.4 Shaft torsional vibration measurements

Maynard et al. (2001) performed an investigation into the feasibility of detecting cracks in gas turbine blades using torsional shaft vibration measurements. They use a 60-tooth shaft encoder installed on the HP turbine disk of a jet engine to obtain measurements. From the results of this investigation, the authors note that there is high confidence in the practical applicability of this technique. From the paper, it seems that Maynard and his co-authors used only a single probe to obtain measurements from the shaft encoder.

1.5.5 Audio signals

King et al. (2006) discuss the application of time-frequency analysis to a microphone signal for the purpose of aero gas turbine condition monitoring. Using this type of analysis, FOD as well as blade flutter can be detected. This type of monitoring can be useful as blade flutter may arise from cracked or damaged blades.

1.5.6 Fibre Bragg Grating sensors

Hwang et al. (2006) present a new monitoring technique using Fibre Bragg Grating (FBG) sensors. An FBG sensor is in essence an optical fibre, which is subjected to a grating process resulting in the fibre having a periodic modulation of refraction index. When broadband light is supplied to the sensor while it is subject to either compressive or tensile stress, the wavelength of the reflected light changes accordingly. This change in wavelength can then be used to measure stress in the sensor. A single optical fibre can consist of a number of FBG sensors, each with a different wavelength reflection characteristic. Hwang and his co-workers propose and test a telemetry-free system with FBG sensors installed on two rotating fan blades. The sensors terminate at the shaft centre (indicating shaft machining) and are supplied with broadband light from a source over a gap distance aligned with the shaft centre. Reflected light from the sensors is then measured at the light source location.

1.5.7 Interferometry

Interferometry for the purpose of vibration measurements involves an image of a deformed or vibrating structure being superimposed onto a reference image of the same structure. This can be implemented using either Holographic Interferometry (HI) or Electronic Speckle Pattern Interferometry (ESPI).

Caponero et al. (2000) present the theoretical background for both techniques. HI involves recording a holographic image of the structure at time instant t. The holographic image of the structure at time instant $t + \Delta t$ is then superimposed onto the recorded holographic image, producing an image with fringes relating to the deformation of the structure. Although this technique does yield high spatial resolution results it is time consuming according to the authors and not suitable for industrial application, as it requires chemical or electrostatic processing of holographic plates.

ESPI however does not require analogue recording media and is thus more feasible for industrial implementation. A reference image of the undeformed structure is recorded along with a reference beam. This yields an image with the reference beam interfering with the speckle field of the structure. The same type of image of the deformed structure is then superimposed on this reference image, again yielding a fringe pattern.

Lesne et al. (1985) use an image de-rotator in order to perform HI on a rotating disk.

1.5.8 Laser Doppler velocimetry

Pfister et al. (2006) present a fibre optic laser Doppler position sensor based on laser Doppler velocimetry for the purpose of blade tip clearance and vibration measurements. Using two laser diodes with different wave lengths, it is possible to simultaneously measure object position and velocity. The authors state that the measurement uncertainty of the sensor is not strongly affected by coherent speckle noise. Although Pfister and his co-authors do not state the maximum sensor measurement bandwidth, they refer to measurements on a rotor with a BPF of 21.7 kHz.

From their references, Lv et al. (2003) seem to implement this technique to measure micro-helicopter blade dynamics. The authors perform signal analysis on the samples using Fast Fourier Transform (FFT) analysis, yielding a very coarse frequency resolution.

1.5.9 Laser Doppler Vibrometry

Laser Doppler Vibrometry (LDV) employs the Doppler effect to measure vibrations on an object. By directing a laser beam onto a target, the reflected light is shifted in

frequency in accordance with the target's vibration velocity. By combining the reflected light with a reference beam, the vibration velocity of the target is obtained.

1.5.9.1 Eulerian Laser Doppler Vibrometry

The ELDV measurement technique involves the LDV being directed at a fixed point in space (Castellini and Santolini, 1998:44). This corresponds to definition of the Eulerian reference frame commonly used in fluid dynamics where the coordinates of the reference frame are fixed and a fluid is observed as it passes by (White, 1999:216). Applied to turbomachinery blades, measurements are then taken as the rotor blades sweep through the laser beam.

Sever (2004) mentions a number of articles dealing with this technique. The earliest of these is by Davis and Kulczyk (1969), who attached reflective tape to the blade to obtain adequate back-scattered light for vibration measurement purposes. Because of the measurement approach the measured signals are available in short pulses. In a later article, Kulczyk and Davis (1970) present some results on using the amplitudes of these pulses to represent vibration of the whole turbine blade row, should the particular frequency of interest be too low to be captured in a single pulse. Davis and Kulczyk (1969) attribute the difficulty of interpretation of the signals to the LDV signal strength.

The same authors (Kulczyk and Davis, 1973) go on to discuss the technique in more detail. According to them, this measurement technique has been used successfully on a turbine with blade tip circumferential velocities of 300 m/s. Kulczyk and Davis note that the short pulse nature of the measured signal affects the output bandwidth and accuracy of the measurement. The authors further state that the measured velocity is not a function of the shape of the blades. Kulczyk and his co-author go on to note that the measured signal is closer to narrowband Gaussian noise than pure-harmonic oscillation, thus limiting the accuracy of the measurements. The authors also give a number of equations to obtain an SNR prediction.

Cookson and Bandyopadhyay (1980) use a laser Doppler fibre optic probe to take axial measurements on rotating blades. The authors use a simple eight-blade test rotor of which one of the blades is excited by a piezo-electric exciter at a fixed frequency. Focussing on only one specific point on the blade width, they develop analytical equations for determining the vibration frequency and amplitude of a single point on the blade for low frequencies. Higher frequency information is attainable when

measurements are taken at slightly different rotation speeds. The equations derived by Cookson and Bandyopadhyay (1980) are however only valid for blade vibration resulting from pure-sinusoidal excitation and not from impulse excitation.

Finke and Schmidt (1996) present a measurement technique similar to that of Cookson and Bandyopadhyay. They make use of the Shannon theorem to obtain blade vibrations. Sampling at frequencies much lower than the blade vibration frequency of interest, they exploit the aliasing effect of the measurement setup to obtain the blade natural frequency.

Reinhardt et al. (1995) use least-squares curve fitting to approximate blade vibration amplitude and frequency at very low rotation speeds (80 to 100 RPM). Reinhardt and his co-workers excite the entire rotor assembly axially with an actuator using a sine wave of constant amplitude and frequency. As with Cookson and Bandyopadhyay (1980), the equations derived are not valid for impulse excitation. The proposed method is further limited to frequencies with more than two vibration cycles during the signal length, implying a lower frequency limit. To obtain lower frequency information, they propose a modal filtering method that will allow blade vibration measurement without rotation speed limitations. However in order to implement the proposed filtering technique, several points along the length of the blade need to be measured simultaneously.

1.5.9.2 Lagrangian Laser Doppler Vibrometry

Lagrangian Laser Doppler Vibrometry entails using an LDV to take measurements in a moving reference frame (Castellini and Santolini, 1998:44). The two modes of implementing this measurement approach are known as TLDV and Continuous Scanning Laser Doppler Vibrometry (CSLDV).

1.5.9.2.1 Tracking Laser Doppler Vibrometry

Quite a number of literature resources are available on this subject. This approach to blade vibration measurement involves the synchronous movement of the laser beam with the rotor in order to follow a specific point on a specific blade.

There are two principal ways to implement TLDV. The first is purely mechanical as used by Sever (2004). Sever uses a conical mirror to direct the laser beam reflected from a 45° mirror installed on the shaft end, onto the rotating blade. The second implementation is to control the mirrors of a Scanning Laser Doppler Vibrometer

(SLDV) in such a way as to trace a circular pattern in synchronization with the shaft rotation speed, thereby following a specific point on the blade.

According to Halkon and Rothberg (2006:1295) tracking vibrometry significantly reduces speckle noise in the measurement of a rotating target. This technique does however introduce scan frequency components into the measured spectra. Misalignment between the axis of scanning system and that of the target rotation axis introduces a DC component as well as a $1\times$ scanning frequency component, both of significant amplitudes. Furthermore, the dual mirror configuration of the SLDV introduces a $2\times$ scanning frequency component, the amplitude of which is influenced by the mirror separation distance, the scanning radius as well as the standoff distance from the target. Although other integer multiple components of the scanning frequency are introduced as well the DC, $1\times$ and $2\times$ components are the most significant.

Lesne et al. (1985) use a tracking laser vibrometer to construct an inverse Campbell diagram of the blade tip vibration of a rotating blade.

Jacobs and Grady (1977) make use of servo scanning mirror as well as a parabolic mirror to perform TLDV circumferentially on an axial-flow machine.

1.5.9.2.2 Continuous Scanning Laser Doppler Vibrometry

The term CSLDV refers to the application of an SLDV where the laser beam is moved continuously across a stationary test surface. Sriram et al. (1992:172) note that when using CSLDV, the measured velocity signal is modulated by the structure's Operational Deflection Shape (ODS). Scans can be performed at uniform or sinusoidal scanning rates. Stanbridge and Ewins (1999) demonstrate how modal testing can be accomplished at discrete excitation frequencies using CSLDV. When a uniform scan rate is used, the resulting LDV signal can be demodulated by multiplication of in-phase and quadrature signals at the excitation frequency. When sinusoidal scan rates are considered, the resulting LDV signal spectrum contains sidebands centred around the excitation frequency and spaced at harmonics of the scanning frequency. Fourier coefficients can then be obtained from theses side bands. By repeating the scans for a range of discrete excitation frequencies, it is then possible to perform conventional modal analysis on these measurements.

Schwinshackl et al. (2010) concur, stating that the processing of signals acquired with CSLDV using sinusoidal scan rates occurs in the frequency domain whereas signal processing from uniform rate scanning occurs in the time domain. These authors also note that the uniform scanning rate approach can be used on structures with surface discontinuities whereas the sinusoidal scanning rate approach cannot.

1.5.10 Radar proximity sensors

Chuckpaiwong (2003) presents a technique using phase-based continuous-wave radar that allows high speed, micro scale measurements with the sensor. Chuckpaiwong (2003:10-11) gives an outline of the capabilities of the radar sensor. The sensor's accuracy is comparable to that of eddy current sensors and has an operating range in the order of meters. The bandwidth and operating temperature range of the sensor exceed that of optical sensors and can be used in a contaminated environment as line-of-sight is not necessary. Chuckpaiwong furthermore states the price of the sensor to be comparable to that of normal eddy-current sensors.

Holst (2005) studies the use of the same sensor as a blade tip TOA measurement probe and focuses on geometric factors affecting the spatial filtering by the sensor. Holst notes that microwave reflection by the blade surroundings will influence the measurements.

1.6 Blade vibration measurement systems

1.6.1 Available systems

Von Flotow et al. (2000) review a number of techniques used for blade vibration monitoring. Faults that can be picked up with such measurements include thermal and centrifugal expansion, spool imbalance as well as crack growth damage. Following a patent search on the subject of blade health monitoring, the authors found over 60 such patents, half of which address clearance measurement and a third that are concerned with vibration using blade TOA. Von Flotow and his co-workers note that the worldwide market for these systems was less than $5 million per year in 2000 and did not support product development at that time.

Von Flotow et al. (2000:439) summarize health monitoring and prognostic capabilities of blade vibration measurement systems. According to the authors it may be possible to anticipate HCF failure of blades. They note that resonance, amplitude and damping changes were under investigation (at the time of their publication) as

reliable damage indicators or "failure precursors". Von Flotow and his co-authors furthermore state that development is required in order to have a fully autonomous system. According to them all laboratory systems (current to publishing) require much human intervention.

Drumm and Haase (2000) discuss the HiBand system of ExSell Instruments. This system can be used for the monitoring of several on-line parameters such as HCF blade vibration and LCF disk cracking of turbines. By using multiple element capacitive sensors (called MasterPlex sensors), they are able to measure high-bandwidth vibrations (20 MHz) at a high signal-to-noise ratio. Similar to torsional vibration measurements using shaft encoders, the system in effect digitizes the position of blades passing the sensors. The MasterPlex sensors can be made for permanent installations into rub strips and high temperature applications of over 2000 °F (1093 °C). Accurate installation of the MasterPlex sensors is very important for tip clearance measurements, but this should not have a substantial effect on blade vibration measurements. Very interestingly, Drumm and Haase (2000) note that disc cracks influence the centre of mass of the rotor. Also according to them, rotor cracks distort the disc strain fields, causing minute changes in the unbalance of the system. The authors note that light probes are not suitable for certain applications such as steam turbine blade vibration measurements. However, from Drumm and Haase's discussion, the ExSell Instruments HiBand system is very suitable for large steam turbine applications when use is made of MasterPlex sensors.

1.6.2 Shortcomings of available systems

According to Beaumont (2004) and Hueck (2004) currently no on-line system is available for detecting blade cracks. Furthermore Hueck refers to a case where a 30% crack was present in a blade while the monitoring system (blade tip TOA) only detected a vibratory change of 0.1%. Hueck also states that the system in consideration, which is available from one of the top steam turbine manufacturers internationally, is limited to bandwidth of 100 Hz.

1.7 Experimental related issues

1.7.1 Non-contact blade excitation techniques

Due to the sensitivity of a bladed disc to mistuning (as discussed in Section 1.2.3.2), non-contact excitation of the structure is necessary for operational testing as well as modal analysis.

Mansisidor (2002) uses eddy-current as well as air-jet excitation on the blades of a disc rotating in a vacuum. Although Mansisidor measures the air pressure of the air-jets, no measurement or approximation is made of the force exerted on the blades by the air-jets.

Vanlanduit et al. (2007) do however make use of calibration curves to approximate the exerted forces by an impinging air-jet. Using an on-off control valve, the authors are able to perform modal analyses up to 1 kHz.

Truman et al. (1961) use a siren-type pulsed-air vibrator to excite stationary blades. The vibrator consists of a speed-controlled slotted disk rotating relatively to a stationary slotted disk, allowing the frequency control of resulting air pulses. The authors note that the subsequent vibrations in the stationary blade occur as a result of these pulsations. The amplitude of the blade vibration is determined by the airflow of the pulses. Truman and his co-workers state that airflow, nozzle-to-surface spacing and the air-jet angle-of-attack relative to the target surface are the main factors determining the dynamic behaviour of the forced blade.

Ziegler (1994) makes use of electromagnetic and air-jet excitation for shrouded and non-shrouded blades respectively.

With regards to stationary modal testing, impact hammer excitation is still more desirable in terms of accuracy since the applied force can be directly measured. Although not a non-contact excitation method in the strictest sense, structural modification due to additional mass is minimized.

1.8 Finite element modelling

Gadala and Byrne (1986) discuss some issues with regards to finite element modelling of blades and present a comparative study for various 2-D and 3-D blade root models. The authors state that the incorporation of centrifugal stiffening is crucial for the dynamic analysis of blades as the blade natural frequencies may rise by up to 30% from their unstressed values as a result.

1.8.1 Model updating based on Frequency Response Functions

The most promising technique of model updating is that of the FRF-based technique. This technique of model updating makes use of measured FRFs to directly update a finite element model.

According to Ewins (2000:462) this technique overcomes the need for large numbers of measurement points in order to capture high order mode shapes. This is due to the fact that FRF data contain information on in-range as well as out-of-range modes (Imregun and Visser, 1991) whereas modal data contain approximation information only on in-range modes.

Furthermore, response data represent the actual dynamic behaviour of the test structure more accurately than does the modal data extracted from these measurements due to the identification errors involved with the latter. These errors are caused by approximations and assumptions of modal property extraction. Imregun et al. (1995) list the fact that this technique does not require modal analysis as one of its main advantages.

In his software package, Balmès (1997:2-147) implements iterative FEM updating using the sum of the squared logarithmic differences between the measured and the numerical FRFs as the objective function.

1.9 Issues with regards to Laser Doppler Vibrometry

1.9.1 Speckle noise

Martarelli and Ewins (2006) present an in-depth study into the analysis of speckle noise in the context of CSLDV along with a mathematical model for the effect of speckle noise. The two authors make a number of interesting remarks with regards to the nature of speckle noise. The first of these is that if the test structure is scanned repeatedly along the same line by the laser beam, the speckle patterns will have a constant spatial distribution. This also means that the noise effect will be concentrated in the frequency domain at the scan frequency and its harmonics. Martarelli and her co-author determined experimentally that as the scanning speed increases, the speckle noise in a measurement increases at the scanning frequency and its harmonics. Furthermore as the scanning speed increases, the broadband noise floor resulting from the speckle noise increases.

According to Martarelli and Ewins it is essential that in choosing a scanning frequency, its harmonics do not overlap with a natural frequency of the structure in order to derive a reliable response. When the scanning frequency is chosen accordingly, the authors state that the noise influence can be neglected by performing a targeted Fourier analysis at the scanning frequency and its harmonics.

Rothberg (2006) performs a study into the fundamental mechanisms of speckle noise occurrence in LDV measurements with specific application to out-of-plane vibration of rotating discs. Rothberg also presents a numerical simulation for the purpose of predicting speckle noise levels in a measurement. The author confirms the statement by Martarelli and Ewins (2006:2279) that although speckle noise affects the Doppler signal in terms of amplitude and phase modulation, it is the phase modulation effect that is of major concern.

Rothberg et al. (1989) identify three sources of speckle-noise namely target tilt as well as in-plane motion and rotating motion.

Denman et al. (1996) looks at the reduction of speckle noise in the measurement of vibration on a rotating structure by means of optimization of detector/target separation. The authors show numerically that speckle noise decreases with an increase in number of speckles in the speckle pattern incident on the detector. Since speckle size increases (and thus number of incident speckles decreases) along with detector/target separation due to light dispersion, it is desirable to have a small detector/target separation. However when the detector/target separation is very small, variance in the speckle pattern increases greatly. The aim is thus to find the optimum detector/target separation distance between these extremes. The authors show this experimentally and indirectly suggest the experimental determination of optimum detector/target separation.

1.9.1.1 The nature of speckle noise

From the literature, the characteristics of speckle noise can be summarized as follows:

1. For a recurring speckle pattern change, the speckle noise will be of a pseudo-random nature. (Rothberg, 2006:4526; Martarelli and Ewins, 2006:2279; Halkon and Rothberg, 2006:1294; Rothberg et al., 1989:518). As a direct result of this, the speckle noise will repeat at the rotation frequency in the case of ELDV.

2. In the frequency domain, speckle noise manifest itself as approximate equal amplitudes at the pattern repeat frequency and its higher-order harmonics. (Rothberg, 2006:4526; Martarelli and Ewins, 2006:2279; Halkon and Rothberg, 2006:1294, Rothberg et al., 1989:518)

3. Speckle noise introduces low-level broadband noise to the measurements. (Rothberg, 2006:4525; Martarelli and Ewins, 2006:2279; Halkon and Rothberg, 2006:1294)

4. In the frequency domain, high orders of prevalent harmonics of the pattern repeat frequency and the sharpness of these peaks are classic characteristics of speckle noise. (Halkon and Rothberg, 2006:1294)

5. Denman et al. (1996) refer to speckle noise as "Doppler signal phase modulation" and "frequency broadening"

1.9.1.2 Noise cancellation

Wilmshurst and Halliwell (1993) present an article concerned with speckle-noise cancellation with excellent results. In their application, the authors use a rotating disc in the place of a Bragg cell to facilitate frequency shifting in a LDV for the purpose of determining the vibration direction of a test object. This rotating disc introduces speckle-noise in the reference signal, which Wilmshurst and Halliwell succeed in attenuating. In order to do this, the authors use a second rotating disc much like a shaft encoder for phase-locked loop correction of a measurement with excitation (speckle-noise and vibration information present) as referenced to a 256-sample time averaged measurement without excitation (speckle-noise dominant in signal). According to the authors, the number of time averages in the reference signal reduces the amplitude of random noise in the signal by a factor of the inverse of the square root of the number of averages.

Wilmshurst and Halliwell (1993) continue to describe the effect of number of time averages on the spectrum of the reference signal. As the number of time averages increases, the widths of harmonic peaks of the disc rotation frequency in the spectrum become narrower. Wilmshurst and his co-worker further use a periodic weighting signal proportional to the time derivative of the reference signal to extract useful information from the speckle-noise contaminated signal. The speckle-noise contaminated signal is multiplied by this weighting function and then integrated.

The two authors perform the noise cancellation in the time domain and go to quite an extent to compensate for inaccuracies caused mainly by speed fluctuations in the

rotating disc. However, these inaccuracies should be easy to overcome if the signal conditioning is performed in the angular domain.

Antoni and Randall (2004b) present a frequency domain noise cancellation algorithm. The minimum sequence length is determined by the inverse of the required frequency resolution and the time delay in the algorithm is given to be proportional to the reciprocal of the noise bandwidth (Antoni and Randall, 2004a).

1.9.2 Effect of geometry on measurements

According to a number of papers (Kulczyk and Davis, 1973:1018; Halliwell, 1996:407; Halkon and Rothberg, 2006:1287), the geometry of a vibrating target does not directly influence CSLDV measurements. In an analysis by Bell and Rothberg (2000:247) this is proven analytically for ELDV implemented on a rotating shaft with an arbitrary cross section.

1.9.3 Practical issues

Although Kadoya et al. (1995) focus on the blade tip TOA measurement application of laser probes, they do address a number of very important practical issues with regards to measurement with the probes in a steam turbine environment. To protect the probe from erosion and to maintain air-tightness, the authors use sapphire glass to seal the probe tip. In order to measure with the probe in the presence of water droplets, Kadoya and his co-authors use a 40 mW laser light source. The probe is arranged so that receiving fibres surround the transmitting quarts fibre. The authors also highlight the importance of perpendicularity between the laser beam and the blade surface to ensure sufficient reflectivity.

Aono et al. (1985) also present a paper on laser probes for TOA. They studied the effect of surface condition of compressor blades (in terms of dust and oil deposit) on the signal quality of the reflected light. Test results for a worst case scenario were favourable for TOA measurements.

1.10 Signal processing

Considering the operational speeds of turbomachinery, it is quite clear that the measured ELDV vibration signals from individual blades will be very short. For a typical steam turbine operating at 50 Hz, the signal length of one measurement for an individual blade is about 0.5 ms. Traditional signal processing techniques such as

FFTs and nonparametric PSD estimations are limited in terms of frequency resolution (Lobos et al., 2006:219; Gamba and Shimamura, 2005:702), making them inappropriate for such short signals. For the sample length considered, a minimum frequency resolution of only 2 kHz is attainable with these techniques. This means that traditional signal processing techniques are not effective in this instance for damage detection.

Alternatively, parametric and subspace spectrum estimation techniques can be utilized (The Mathworks, 2006:3-7). As opposed to nonparametric estimation where the PSD is directly estimated from the signal, parametric methods estimate the PSD from a model of the signal using Autoregressive (AR) techniques. Giordano and Hsu (1985) note that these AR techniques make it possible to identify dominant spectral peaks masked in normal periodograms. Typical methods used are the Yule-Walker AR method and the Burg method and can yield higher resolutions for short signals as compared to nonparametric methods. According to Giordano and Hsu (1985) the maximum entropy method formulated by Burg is very well suited particularly for short signals. The Burg method is however prone to frequency splitting and is sensitive to the initial phase of the signal analyzed (Marple, 1987:225,227)

Subspace methods yield spectrum estimates based on eigendecomposition of the correlation matrix of the signal. Examples include the Multiple Signal Classification (MUSIC) method and the Eigenvector (EV) method.

According to Gamba and Shimamura (2005:702) and Fante (1988) however, these alternative methods yield superior results only at high SNRs. Fante (1988) states that at SNRs of lower than ten, ARMA modelling rather than AR modelling should be used to estimate the spectra. According to Marple (1987:231) this is due to the fact that the all-pole model assumed with AR techniques is no longer valid when noise is present.

Gamba and Shimamura (2005:702) propose the Iterative Noise Variance Estimation (INVE) technique based on low-order Yule-Walker equations to improve the results. From analytical results, the authors show this technique to be more noise-robust than the popular spectrum estimation techniques.

Hirata (2005) proposes the use of NHFA for short data records where the frequency resolutions obtainable with Harmonic Fourier Analysis (HFA) are too coarse to yield useful information. As in HFA, the time signal is also considered as the summation

of sine and cosine components. However, these components can be at arbitrary frequencies (i.e. not necessarily at integer multiples of the fundamental frequency). Steele (1999) employs a similar methodology to estimate components in ocean wave data.

Muraoka and Nishioka (2004) investigate the frequency limit of NHFA (which they refer to as generalized harmonic analysis) by considering a signal consisting of two sinusoids at different frequencies. From the conclusions based on their results, it is clear that the minimum resolvable frequency resolution between two sinusoidal waves is still determined to an extent by the $1/t$ limitation as per classic Fourier analysis. The authors also note that the phases of the sinusoids influence the frequency resolution. According to Muraoka and his co-author, rectangular windowing of a signal is most suited for NHFA.

1.11 Scope of research

The literature study covers a broad range of topics related to on-line turbomachinery blade condition monitoring. From this literature study, the scope of this research work is defined in the following paragraphs.

On-line blade vibration information contains crucial information for the on-line condition monitoring of these components. To perform these measurements, a number of options present themselves. The most intuitive approach is to install sensors such as strain gauges on the blades. However the limited life spans of such systems negate their long term use on industrial rotors. Measurements can also be obtained using TLDV or ESPI, with both of these approaches requiring blade line-of-sight over a significant rotor angle. This of course is not feasible for most industrial rotors due to the presence of rotor casings, guide vanes or other structural elements. Blade tip TOA monitoring systems are used in industry. Nevertheless the drawback of these systems is the large number of sensors required to obtain useful measurement bandwidths. An alternative approach is to measure blade vibrations in an Eulerian fashion. This measurement approach requires a non-contact sensor with a high bandwidth and a long stand-off distance. Radar proximity sensors are promising sensors for this application although effects such spatial filtering, blade geometry and microwave reflection by surroundings need to be taken into account.

Measurements acquired by means of ELDV however are not affected by these factors. LDVs are capable of measuring large dynamic ranges from extremely small vibrations to large vibrations up to 30 m/s. These instruments furthermore have measurement bandwidths from 0 Hz up to several MHz. In an industrial environment the laser beam transmission can be accomplished with fibre optics, thus removing the sensor itself from the operating environment. For these reasons, ELDV is the main measurement approach in this thesis using the Polytec PSV300 SLDV at the University of Pretoria.

The two main challenges faced with ELDV as applied to rotating blades, are sufficient laser reflectivity from the blades, as well as the brief nature of the measured vibration signals. The challenge with regards to laser reflectivity could be overcome by either surface treatment of the blades or by increasing the strength of the laser source. Since the latter option is not available on the Polytec PSV300, blade surface treatment is performed in the form of reflective material installed on the test rotor.

The ELDV measurement technique is studied analytically on a vibrating cantilever beam translating longitudinally at constant speeds and the results are verified experimentally. From this study, a numerical simulation approach of ELDV is proposed and evaluated using standard simulation techniques. This approach is then extended to rotating blades.

A simple single stage axial-flow test rotor is used for experimental testing at relative slow rotation speeds up to a maximum of 1500 RPM. The blades are straight and flat and are attached to the rotor hub by means of clamping to ensure repeatable boundary conditions at the blade roots. A single stationary air-jet is used to simulate guide vane excitation of the rotating blades and is controlled to yield repeatable excitation. The test rotor (installed with a high resolution shaft encoder) is driven by speed-controlled motor and various pre-sets are used to ensure repeatable rotor speed settings.

The experimental simulation of cracks is not a trivial exercise. This thesis is however more concerned with the effect of damage on blade vibration than the damage mechanisms themselves. For this reason, damage is simulated in the test rotor by means of slot cuts into the blade leading edges close to the blade roots using a high-speed rotary tool. This option is attractive since it can be performed *in situ*, thus eliminating blade root boundary condition changes due to removal and reinstallation of the blades during the testing phase.

Prior to dynamic testing, stationary modal testing is conducted on the test rotor and blades. A modal hammer is used for excitation and the responses are measured via LDV. The choice of excitation and measurement are to minimize any modification of structural dynamics by additional sensor mass and so ensure accurate FRF measurements.

Initial testing is carried out with a single blade on the rotor to simplify signal processing by eliminating the effects of global modes due to the presence of other blades. Measurements are recorded at a fixed rotor speed and for increasing damage on the blade. The signal processing methodology developed from these measurements is then applied to measurements from a fully bladed rotor with various damage levels on multiple blades. Four different rotor speeds are considered.

The brief nature of ELDV blade vibration signals presents the main challenge of this thesis in terms of signal processing. Various standard and non-standard signal processing techniques are investigated to obtain blade health indicators. NHFA in

particular is well suited to extract information from these short signals and a study of the analysis technique is conducted, showing that care must be taken when performing NHFA due to frequency component cross-talk. A sensitivity analysis shows that this phenomenon can be exploited for frequency shift detection.

NHFA is performed on the single-blade measurements over bands around various reference frequencies. The Maximum Absolute Unwrapped Phase Angle Trends (MAUPATs) over these bands are shown to be robust indicators of blade health deterioration. MAUPATs are calculated on the multi-blade measurements and the progressive standard deviations of the individual blade MAUPATs are demonstrated as useful for distinguishing between healthy and damaged blades. Evaluating also cross-correlation coefficient and RMS value trends of these measurements, an ANN is successfully trained to quantify the conditions of the individual blades.

FEMs of the different test rotor configurations are constructed and updating thereof is performed using FRF-based model updating. To incorporate the proposed numerical simulation approach of ELDV, the FEM mesh nodal resolutions are specified accordingly along the measurement curves. Damage is simulated in the FEMs to represent the experimental damage and centrifugal stiffening is included in simulations while gyroscopic effects are discarded. The FEMs are used to verify experimental results.

1.12 Document layout

Chapter 1 contains a thorough literature study covering a broad range of topics related to on-line turbomachinery blade condition monitoring. In this chapter, the research scope is also defined.

In Chapter 2, an analytical study of ELDV is conducted on an Euler-Bernoulli cantilever beam that translates at a constant velocity relative to a stationary LDV. A numerical simulation approach of ELDV is then proposed using a Lagrangian Vibration Response Matrix (LVRM) for a reference scanning speed. The feasibility of using interpolation on this LVRM to estimate responses for other translation velocities is also investigated. This simulation approach is extended to axial-flow rotating blades and the findings of the analytical ELDV study are verified experimentally.

Chapter 3 investigates the feasibility of using ELDV as an on-line blade vibration measurement technique a single-blade experimental rotor. ELDV and TLDV measurements are presented for increasing damage levels on the blade and vibratory phase angle shift is illustrated to be a valuable blade health indicator. NHFA is utilized to obtain phase angle information from the ELDV measurements and MAUPATs over bands around reference frequencies are established as robust blade health indicators. After FEM validation, the experimental results are verified with the aid of FEM simulations.

ELDV measurements on a multi-blade test rotor are considered in Chapter 4 with the tests conducted at different rotor speeds and increasing damage levels on various blades.

Considering the progressive standard deviations of MAUPATs as well as some time domain parameters, it is proven that individual blade conditions can be quantified via ANN implementation. Individual blade natural frequencies are also accurately approximated from ELDV rundown signatures.

Chapter 5 concludes the work in this thesis and additional work for future research is proposed.

1.13 Publications

This work forms part of a research initiative consisting of two parts. The first part is contained within the master's dissertation of the author and was concerned with the development of an on-line fan blade damage detection methodology using piezoelectric strain sensors and accelerometers installed on the blades of a four-blade test rotor. Using ANNs it was shown experimentally that on-line blade condition monitoring can be performed using less than one sensor per blade. ANNs were also trained on FEM results and successfully applied to experimental measurements. The outputs from the author's master's work are as follows:

1. Oberholster, A.J. (2004). *The development of an on-line fan blade damage detection methodology.* Master's dissertation. Pretoria: University of Pretoria.
2. Heyns, P.S., Oberholster, A.J. (2004). *On-line fan blade damage detection.* Proceedings of the 11th International Congress on Sound and Vibration: St. Petersburg, Russia, 2921-2928.
3. Oberholster, A.J., Heyns, P.S. (2006). On-line fan blade damage detection using neural networks. *Mechanical Systems and Signal Processing*, 20(1), 78-93. (DOI 10.1016/j.ymssp.2004.09.007).

4. Heyns, P.S., Stander, C.J., Oberholster, A.J., Schön, P.P., Ngwangwa, H.M. (2007). *Machine and structural health monitoring: Some recent developments.* Proceedings of the 3rd International Conference on Structural Engineering, Mechanics and Computation: Cape Town, South Africa, 124-129.

This thesis contains the second part of the research initiative and focuses on using a non-contact measurement approach. The following conference papers and articles were produced during the course of this thesis:

1. Oberholster, A.J., Heyns, P.S. (2007). *The application of Eulerian laser Doppler vibrometry to on-line damage detection of axial-flow turbomachinery blades*. Proceedings of the 20th International Congress on Condition Monitoring and Diagnostic Engineering Management: Faro, Portugal, 637-645.

2. Oberholster, A.J., Heyns, P.S. (2008). *A study of the non-harmonic Fourier analysis technique*. Proceedings of the 21st International Congress on Condition Monitoring and Diagnostic Engineering Management: Prague, Czech Republic, 361-370.

3. Oberholster, A.J., Heyns, P.S. (2009). Online condition monitoring of axial-flow turbomachinery blades using rotor-axial Eulerian laser Doppler vibrometry. *Mechanical Systems and Signal Processing*, 23(5), 1634-1643. (DOI 10.1016/j.ymssp.2009.01.001).

4. Oberholster, A.J., Heyns, P.S. (In press). Eulerian laser Doppler vibrometry: Online blade damage identification on a multi-blade test rotor. *Mechanical Systems and Signal Processing*. (DOI 10.1016/j.ymssp.2010.03.007).

5. Oberholster, A.J., Heyns, P.S. (In progress). On the measurement of circumferential vibration on rotating blades using laser Doppler vibrometry. *Experimental Techniques*.

Chapter 2 Eulerian Laser Doppler Vibrometry

2.1 Introduction

This chapter studies the ELDV measurement technique as applied to translating targets. To demonstrate the most salient characteristics of ELDV, an analytical study is conducted on a translating Euler-Bernoulli cantilever beam and ELDV is defined accordingly. The analytical ELDV equations are then expressed in numerical form and an approach for the simulation of ELDV is proposed. The effects of translation speed on ELDV measurements are studied as well and the feasibility of using the measurement technique as a condition monitoring tool is determined. The numerical and analytical results are confirmed experimentally after which the interpolation approach is extended to rotating axial-flow blades.

2.2 Analytical and numerical study

2.2.1 Cantilever beam theory

It is useful for understanding the characteristics of ELDV to consider a cantilever beam of length l, vibrating under the influence of an arbitrary concentrated load F, while translating at a constant speed c, perpendicular to a stationary LDV (see Figure 2). This is in effect an application of CSLDV with a uniform scanning rate. Torsional, sideways and axial vibrations are not taken into account for this demonstration.

By considering the Lagrangian (i.e. the moving reference frame) vibration of the beam as a function t, the Lagrangian vibration displacement w_L can be obtained at an arbitrary discrete Lagrangian measurement position x_L using the well-known Euler-Bernoulli formulation:

$$w_L(x_L, t) = \sum_{j=1}^{\infty} W_j(x_L) \cdot q_j(t)$$

Equation 4

where W_j and q_j respectively are the characteristic function and generalized coordinate for the jth mode of the cantilever beam with corresponding natural frequency ω_j (Rao, 1995).
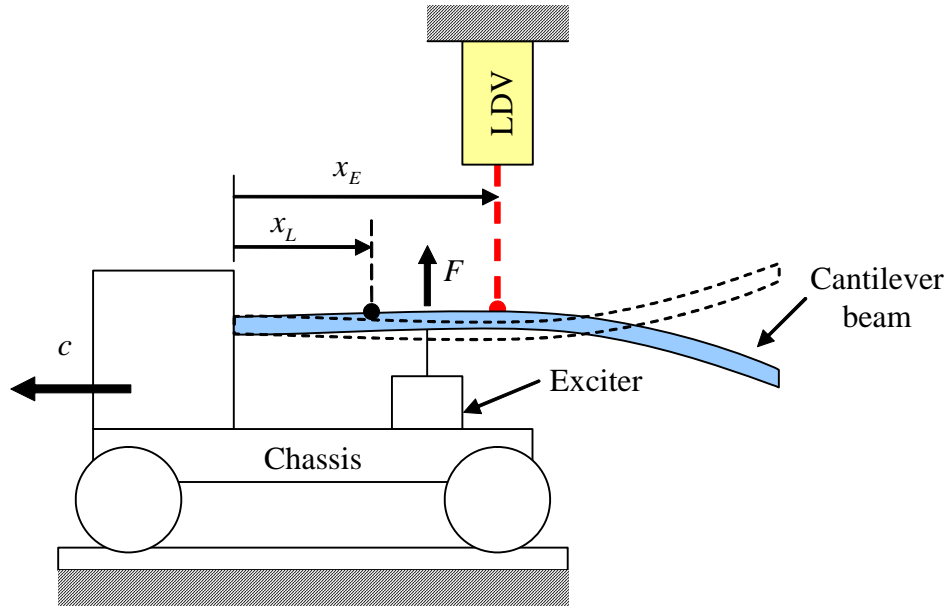
Figure 2: Longitudinally translating cantilever beam

Since LDVs measure vibration velocity it is desirable to find the Lagrangian vibration velocity v_L which obtained by appropriate differentiation of Equation 4:

$$v_L(x_L, t) = \frac{\partial w_L(x_L, t)}{\partial t} = \sum_{j=1}^{\infty} W_j(x_L) \cdot \frac{dq_j(t)}{dt}$$

Equation 5

2.2.2 ELDV analytical formulation

If the beam vibration is considered in the Eulerian (i.e. the stationary) reference frame, the Eulerian measurement position x_E is a function of c and t (i.e. $x_E = ct$) and consequently does W_j become time dependent:

$$W_j(x_E) = W_j(ct)$$

Equation 6

Since both W_j and q_j are now functions of t, the contribution of the jth mode to the observed vibration response is effectively the result of amplitude modulation of q_j by W_j. The Eulerian vibration velocity v_E is thus expressed by extending Equation 5 to the Eulerian reference frame:

$$v_E(c,t) = \sum_{j=1}^{\infty} W_j(ct) \frac{d}{dt} q_j(t) \text{ for } 0 \leq t \leq \frac{l}{c}$$

<div align="right">**Equation 7**</div>

Since the setup in Figure 2 is effectively CSLDV with a uniform scanning rate, the amplitude modulation observation from Equation 7 is confirmed by Schwingshackl et al. (2010) who state that the ODS modulates the excitation signal.

2.2.3 Numerical simulation of ELDV

The main difference between Equation 5 and Equation 7 is the way in which the measurement positions are defined. Since c is assumed to be constant, it is possible to obtain v_E for discrete time instants t_n and discrete measurement positions $x_{E,n}$ by simply considering the values of discrete v_Ls at the corresponding times and measurement positions (i.e. $x_{L,n} = x_{E,n}$). It is therefore possible to define an Eulerian Vibration Response (EVR) vector as:

$$\begin{aligned}
\vec{v}_E &= [v_E(c,t_0), \quad v_E(c,t_1), \quad ..., \quad v_E(c,t_{N-1}), \quad v_E(c,t_N)] \\
&= [v_L(x_{L,0},t_0), \quad v_L(x_{L,1},t_1), \quad ..., \quad v_L(x_{L,N-1},t_{N-1}), \quad v_L(x_{L,N},t_N)]
\end{aligned}$$

<div align="right">**Equation 8**</div>

for $x_{L,n} = x_{E,n} = ct_n$ with $n = 0, 1, ..., N$ and where N is the number of samples.

Equation 8 implies that it is necessary to have a Lagrangian Vibration Velocity Response (LVVR) vector $\vec{v}_{L,n}$ available for each $x_{L,n} = x_{E,n}$ over the entire measurement period:

$$\vec{v}_{L,n} = [v_L(x_{L,n},t_0) \quad v_L(x_{L,n},t_1) \quad \cdots \quad v_L(x_{L,n},t_N)]$$

<div align="right">**Equation 9**</div>

If a fixed sampling frequency is used with a corresponding time interval $\Delta t = t_n - t_{n-1}$, and sampling is performed over the total length of the cantilever beam from root to tip, N is determined by the time required for the laser to traverse the full length of the cantilever beam (i.e. l/c) divided by Δt. Since N must be an integer, the floor function is applied (rounded towards minus infinity):

$$N = \left\lfloor \frac{l}{c \cdot \Delta t} \right\rfloor$$

<div align="right">**Equation 10**</div>

Equation 8 and Equation 10 have a number of implications since $x_{L,n} = x_{E,n} = ct_n$. Firstly, a new EVR has to be calculated for every different value of c. Secondly, if a FEM is used to calculate $\vec{v}_E$, $\vec{v}_{L,n}$ has to be extracted for each of the element nodes with locations corresponding to $x_{E,n}$. This implies that a different mesh density is required for every value of c.

This requirement can however be alleviated by utilizing an appropriate interpolation scheme on a Lagrangian Vibration Response Matrix (LVRM). This LVRM ($\hat{V}_{L,c_{ref}}$) consists of row vectors with each row the $\vec{v}_{L,n}$ for $x_{L,n}$ corresponding to an arbitrary reference speed c_{ref}:

$$\hat{V}_{L,c_{ref}} = \begin{bmatrix} \vec{v}_{L,0} \\ \vec{v}_{L,1} \\ \vdots \\ \vec{v}_{L,N_{ref}} \end{bmatrix} = \begin{bmatrix} v_L(x_{L,0},t_0) & v_L(x_{L,0},t_1) & \cdots & v_L(x_{L,0},t_{N_{ref}}) \\ v_L(x_{L,1},t_0) & v_L(x_{L,1},t_1) & \cdots & v_L(x_{L,1},t_{N_{ref}}) \\ \vdots & & \ddots & \vdots \\ v_L(x_{L,N_{ref}},t_0) & v_L(x_{L,N_{ref}},t_1) & \cdots & v_L(x_{L,N_{ref}},t_{N_{ref}}) \end{bmatrix}$$

Equation 11

with $x_{L,n} = c_{ref}t_n$ and the reference sample length $N_{ref} = \lfloor l/(c_{ref} \cdot \Delta t) \rfloor$.

If a speed ratio k is defined as the ratio of the desired c to c_{ref}, i.e. $k = c/c_{ref}$ and if $k = 1$ (i.e. $c = c_{ref}$), the Eulerian measurement positions $x_{E,n}$ are identical to $x_{L,n}$. Thus Equation 8 holds for $k = 1$ and can be expressed in terms of the LVRM:

$$\vec{v}_{E,c_{ref}} = \left[\hat{V}_{L,c_{ref}}^{0,0}, \quad \hat{V}_{L,c_{ref}}^{1,1}, \quad ..., \quad \hat{V}_{L,c_{ref}}^{N_{ref}-1,N_{ref}-1} \quad \hat{V}_{L,c_{ref}}^{N_{ref},N_{ref}} \right]$$
$$\therefore \vec{v}_{E,c_{ref}}^{\,n} = \hat{V}_{L,c_{ref}}^{n,n} \quad \text{for all} \quad n = 0, 1, ..., N_{ref}$$

Equation 12

where the superscripts indicate element numbers. In other words if $k = 1$, the EVR is obtained directly from the diagonal of the LVRM.

Similarly for other integer values of k:

$$\vec{v}_{E,k\cdot c_{ref}} = \left[\hat{V}_{L,c_{ref}}^{k\cdot 0,0}, \quad \hat{V}_{L,c_{ref}}^{k\cdot 1,1}, \quad ..., \quad \hat{V}_{L,c_{ref}}^{k\cdot(N_k-1),N_k-1} \quad \hat{V}_{L,c_{ref}}^{k\cdot N_k,N_k} \right]$$
$$\therefore \vec{v}_{E,k\cdot c_{ref}}^{\,n} = \hat{V}_{L,c_{ref}}^{kn,n} \quad \text{for all} \quad n = 0, 1, ..., N_k$$

Equation 13

with $x_{E,n} = x_{L,kn}$ and $N_k = \lfloor N_{ref}/k \rfloor$ compensating for the reduction in number of samples from $\hat{V}_{L,c_{ref}}$ to $\vec{v}_{E,k\cdot c_{ref}}$.

Equation 12 and Equation 13 are represented graphically by Figure 3 for different integer values for k. The LVRM and the various EVRs are shown for a vibrating cantilever beam (Table 1) excited with a 0.5 ms half-sine pulse.

When k is a not an integer it is necessary to perform interpolation. Satisfactory interpolation requires a careful choice of both Δt and position intervals Δx in $\hat{V}_{L,c_{ref}}$. Δt should be small enough to capture the vibration response at each position properly, whereas Δx should be small enough to capture the spatial variation in the vibration responses adequately.

Table 1: Cantilever beam properties

Young's modulus	223 GPa
Density	7770 kg/m^3
Length	112.5 mm
Width	25 mm
Thickness	2 mm
Excitation force location from beam root	35.25 mm
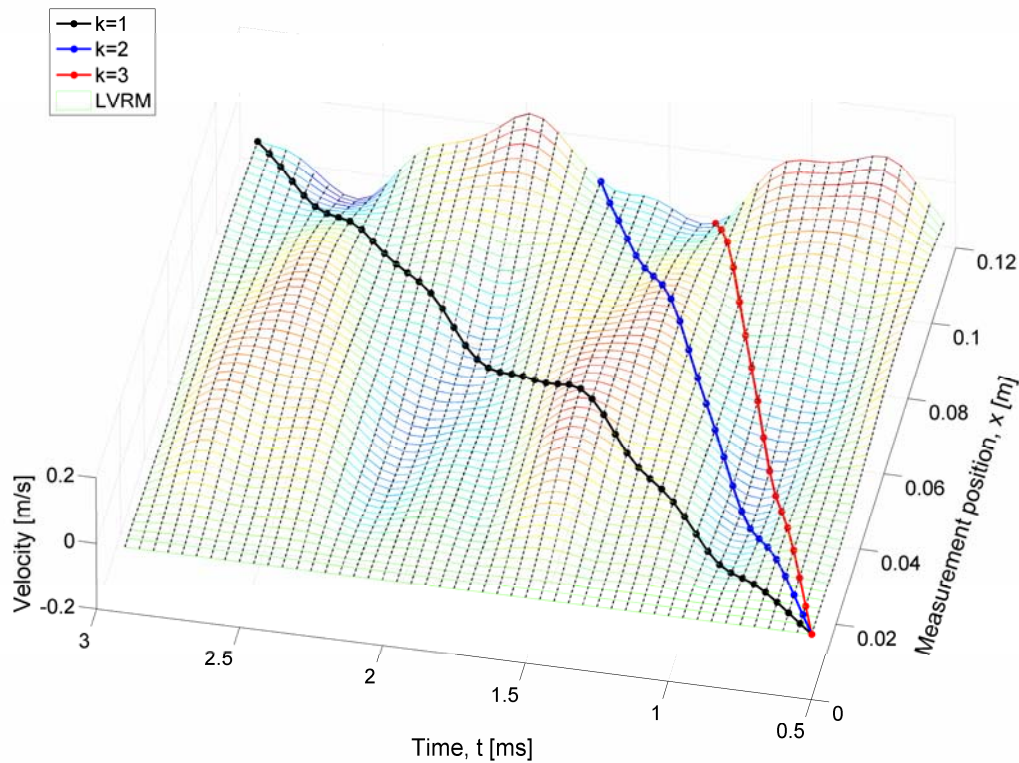
Figure 3: LVRM and EVRs for integer values of k

To evaluate the accuracy of obtaining $\vec{v}_E$ from $\hat{V}_{L,c_{ref}}$ via interpolation for non-integer values of k, simulations were done in Matlab for a cantilever beam with the same properties as listed in Table 1, again excited with a 0.5 ms half-sine pulse. The time interval was fixed for a sampling frequency of 12 kHz, allowing the accurate simulation of the beam's first four natural frequencies.

An arbitrary c of 13.798 m/s was chosen to obtain the interpolated EVRs. Different LVRMs were calculated for integer values of c_{ref} ranging from 1 m/s to 20 m/s, so effectively varying k. The interpolated $\vec{v}_E$s were obtained from each of these LVRMs and compared with an $\vec{v}_E$ for $k = 1$ (i.e. $c_{ref} = 13.798$ m/s) to evaluate the accuracies of the interpolations. Linear and cubic spline interpolation methods were evaluated to determine the most suitable approach.

Figure 4 shows how the value of k affects the mean absolute error between the interpolated $\vec{v}_E$s ($k \neq 1$) and the direct $\vec{v}_E$ ($k = 1$). Clearly it is beneficial to have a low value for c_{ref} (i.e. high k) for $\hat{V}_{L,c_{ref}}$. It can also be observed that the cubic spline interpolation scheme provides results which are several orders of magnitude better than those obtained from linear interpolation.

Schwingshackl et al. (2010) also use interpolation in simulating uniform scan rate CSLDV measurements on a cylindrical FEM. In accordance with the observed advances of having a high k value, the authors use a high mesh density to obtain a LVRM. They do however not state which interpolation scheme they employ.

2.2.4 Effect of scanning speed

Since ELDV measurements are dependent on scanning speed, it is necessary to determine the extent of this influence. In this section the cantilever beam considered in Section 2.2.3 is subjected to a half-wave sine pulse of amplitude 10 N with duration of 0.5 ms. This choice of excitation was made to simulate an impulse force, allowing the simultaneous excitation of all the natural frequencies considered. The pulse duration was chosen to have an excitation bandwidth that encompassed the relevant natural frequencies. A sampling frequency of 12.8 kHz allowed sufficient measurement bandwidth to detect the beam's fourth natural frequency in the frequency spectra. In this section, the scanning direction will be from beam tip to root starting from $t = 0$ s. When the initial displacements and velocities of the beam are set to zero, spectra can be calculated from the EVRs without having to use windowing

functions. This is an advantage as windowing functions may introduce distortions in the spectra.
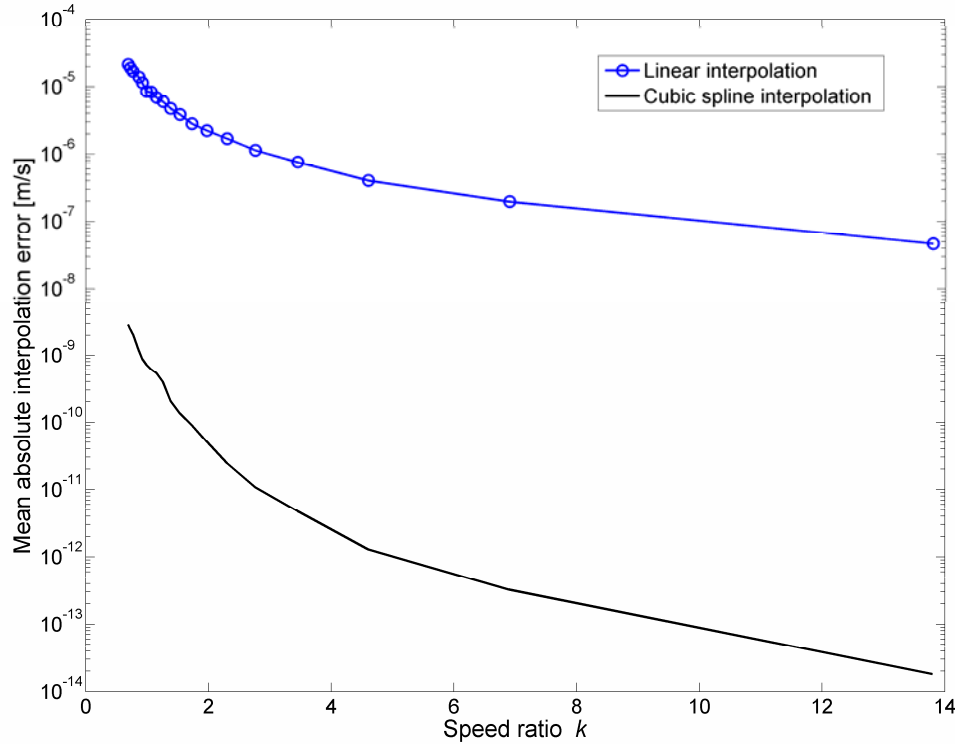
Figure 4: LVRM interpolation scheme evaluation

The ω_j s of the cantilever beam were calculated analytically and are listed in Table 2:

Table 2: Euler-Bernoulli cantilever beam natural frequencies

j	ω_j [Hz]
1	136.8
2	857.0
3	2339.7
4	4702.5

2.2.4.1 Modulation frequency

Consider the PSD of the $\bar{v}_E$ for $c = 0.1125$ m/s (i.e. the sample length is 1 s) as depicted in Figure 5 with the red lines indicating the beam's ω_j s. When a closer look is taken at the peaks, clear sidebands are visible around ω_2, ω_3 and ω_4. Figure 6

shows this for ω_4 and verifies the observation of Section 2.2.2 with regards to amplitude modulation of q_j by W_j (Equation 7).
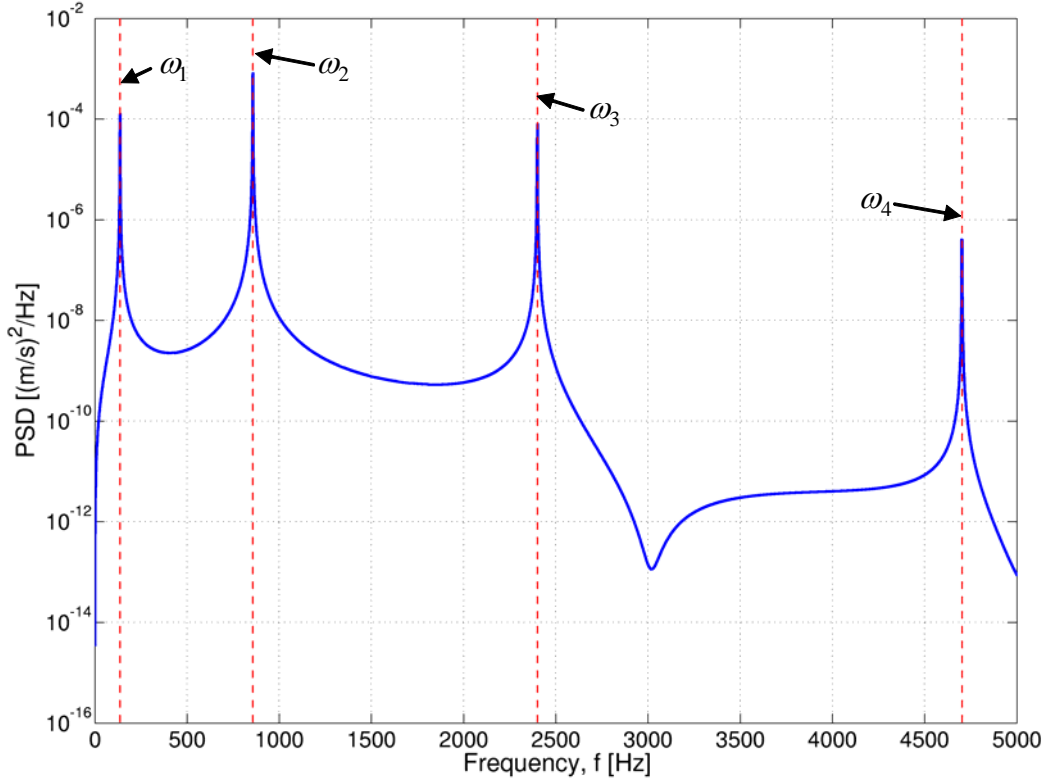
Figure 5: PSD of $\vec{v}_E$ for $c = 0.1125$ m/s

Since W_j is a function of c, its modulation frequency Ω_j should be affected by c as well and the sideband separation in the spectrum should thus be proportional to c. To verify this, EVRs were calculated for different values of c. To increase the frequency resolution of the EVR spectra, each EVR was padded with zeros to yield a 0.1 Hz spectral resolution. The PSDs are shown in Figure 7 from which it is clear that Ω_j increases with c. From this figure, the negative effects of zero padding are evident by the manifestation of decrease in peak amplitudes, increase in peak damping as well as the introduction of fundamental frequency harmonics. These effects were not of concern since only the frequencies of the modulation peaks were considered here.

To analytically determine the relationship between Ω_j and c, it is necessary to study the definition of W_j as given by Rao (1995). In the context of ELDV, W_j is expressed as:
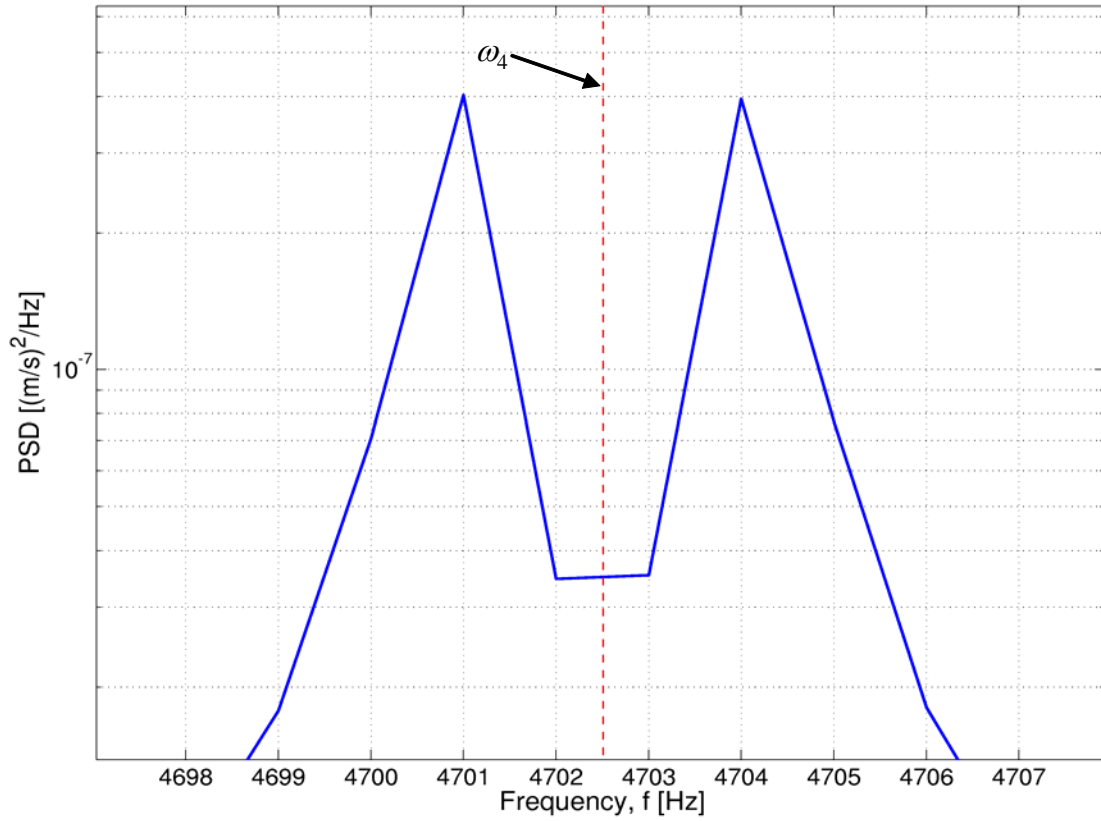
Figure 6: Sidebands around 4th natural frequency
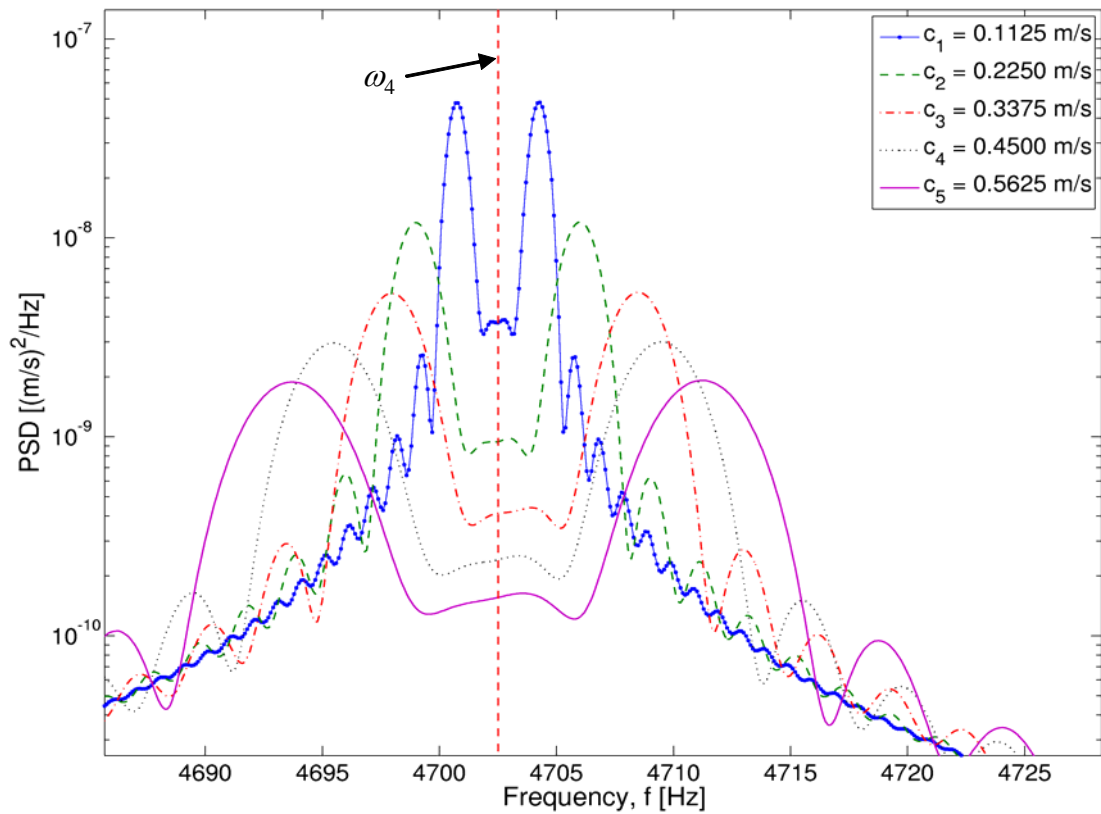
Figure 7: Effect of scanning speed on modulation sidebands separation

$$W_j(ct) = E_j \left[\sin\beta_j ct - \sinh\beta_j ct - \left(\frac{\sin\beta_j l + \sinh\beta_j l}{\cos\beta_j l + \cosh\beta_j l} \right)(\cos\beta_j ct - \cosh\beta_j ct) \right]$$

Equation 14

with $\cos\beta_j l \cdot \cosh\beta_j l = -1$. The first four W_js of the considered cantilever beam are shown in Figure 8.
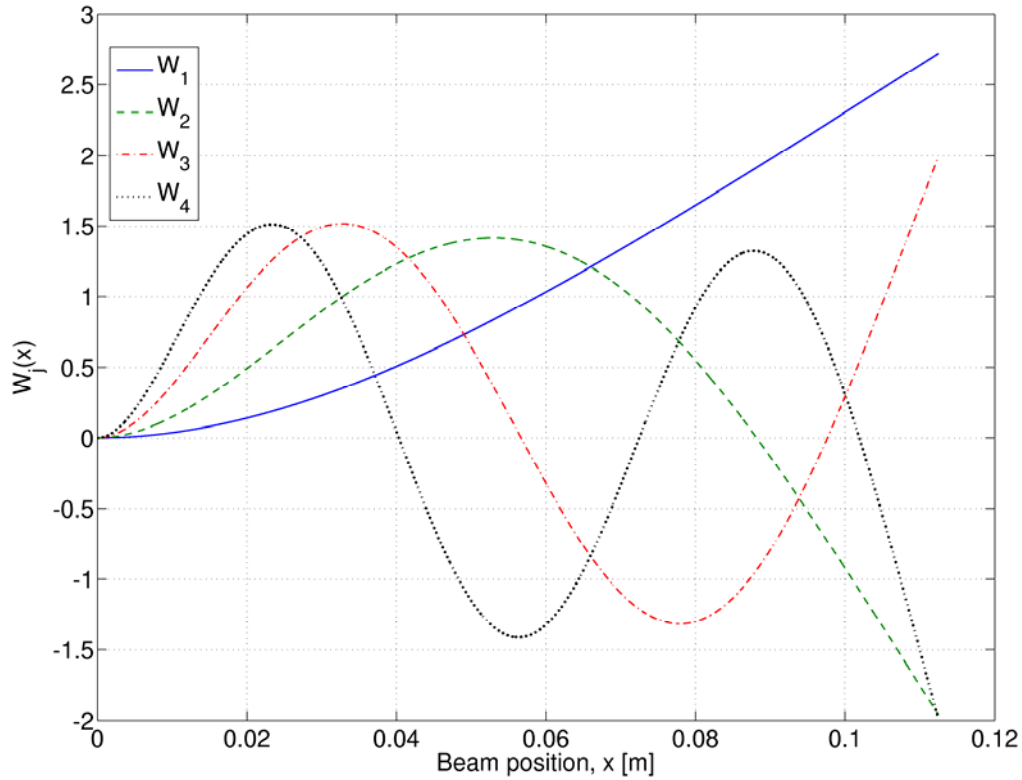
Figure 8: Characteristic functions W_j

Since E_j and $(\sin\beta_j l + \sinh\beta_j l)/(\cos\beta_j l + \cosh\beta_j l)$ are constants and both $(\sinh\beta_j ct)$ and $(\cosh\beta_j ct)$ are not periodic functions (i.e. non-oscillating), Ω_j is thus mainly dependent on the $(\sin\beta_j ct)$ and $(\cos\beta_j ct)$ terms.

Ω_j can thus be approximated in Hz as

$$\Omega_j(c) \approx \frac{\beta_j c}{2\pi}$$

Equation 15

Figure 9 compares the predicted values of Ω_j from Equation 15 with the values obtained from the $\bar{v}_E$ PSDs for different values of c. From Figure 9 excellent

correlation exist between the predicted and actual values of Ω_j for $j = 2,3,4$. However Equation 15 is clearly not valid for $j = 1$. When referring to Figure 8 it is clear that W_1 never crosses zero. Thus strictly speaking, W_1 does not amplitude modulate q_1 but rather amplifies q_1 in an increasing fashion. For this reason $\Omega_1 = 0$, as verified by the spectral results of Figure 9.
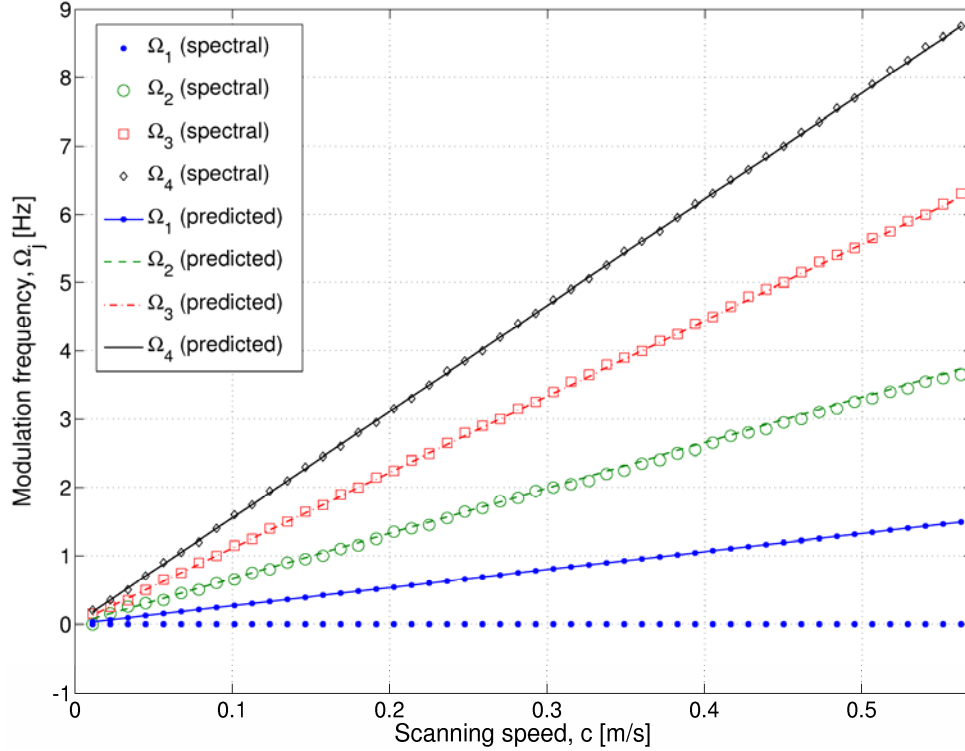
Figure 9: Comparison of actual and predicted values of Ω_j for various values of c

2.2.4.2 Frequency resolution

In order to accurately measure the vibration at a certain frequency, at least one complete vibration cycle at that frequency needs to be sampled at a sufficient sampling frequency. This has an important implication for EVR spectra, specifically with regards to the scanning speed.

The time it will take to perform a constant speed scan of the beam, is given as $t_N = l/c$ and subsequently the frequency resolution is:

$$\Delta f = \frac{1}{t_N} = \frac{c}{l}$$

Equation 16

Equation 16 can be rearranged to find the maximum scan speed c_{max} for which the minimum required frequency resolution Δf_{min} can be obtained.

$$c_{max} = l \cdot \Delta f_{min}$$

Equation 17

Consider ω_1 = 136.8 Hz of the cantilever beam. The maximum scanning speed for which this frequency can be accurately detected is given by Equation 17 as $c_{max} = 15.39\,\text{m/s}$. Figure 10 shows the FFTs for five different scanning speeds expressed as fractions of this c_{max}. It can be shown that ω_1 is detected within 1 % for scanning speeds lower than $0.17\,c_{max}$ and that at c_{max}, the detected peak frequency has a 36% error. Thus although signal activity can be detected using a c_{max} value as defined by Equation 17, to accurately obtain peak frequency from ELDV measurements requires the value of c_{max} to be further reduced by a factor of 10:

$$c_{max} = \frac{l \cdot \Delta f_{min}}{10}$$

Equation 18
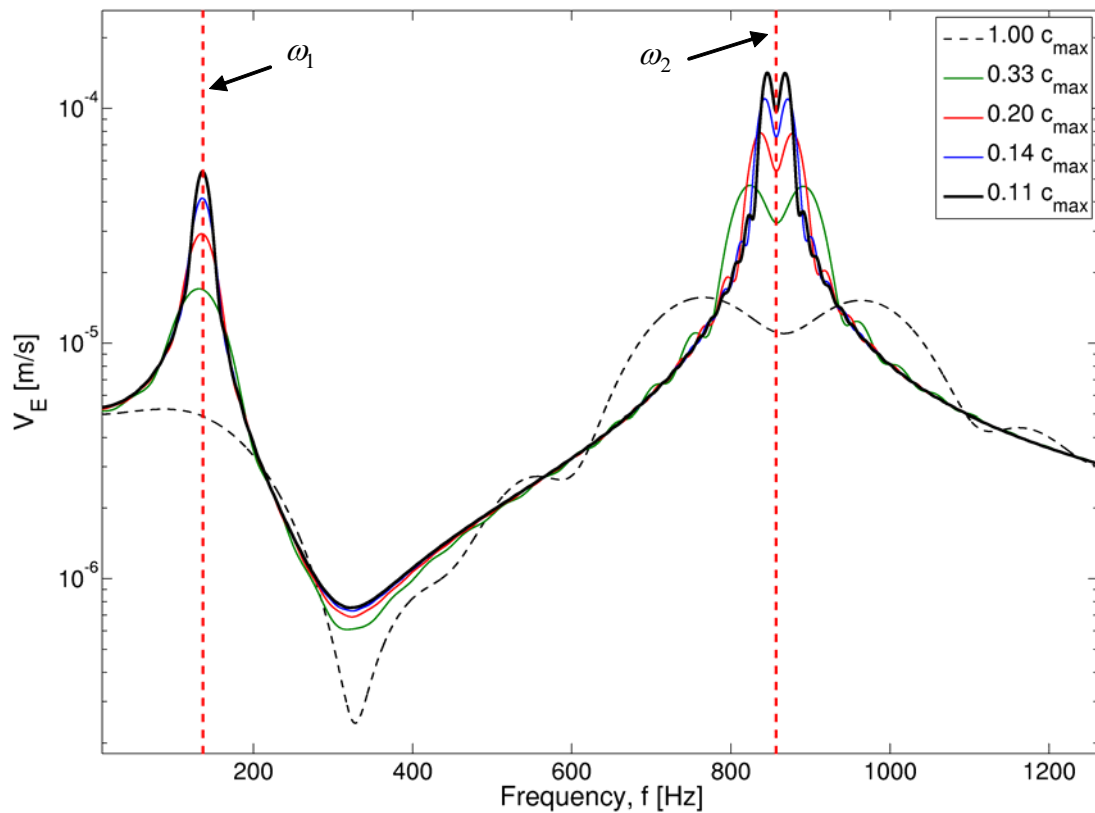
Figure 10: Observed vibration FFTs for different scanning speeds

2.2.5 Condition monitoring feasibility study

One of the main premises of condition monitoring using vibration signals is that damage as in the form of cracks reduces the stiffness of the structure, thereby leading to a decrease in structural natural frequencies. Although it would be desirable to simulate this type of damage in the FEM, it is computationally very expensive to obtain $\hat{V}_{L,c_{ref}}$ with c_{ref} low enough to obtain a good spectral frequency resolution for the purpose of accurate peak shift detection.

To simulate crack-type damage in an Euler-Bernoulli beam on the other hand, is no small task, although it is definitely possible. However, since a decrease in natural frequencies is associated with a decrease in stiffness, natural frequency shifts can be induced in an Euler-Bernoulli beam by simply varying Young's modulus of the beam.

This was done for the beam of Section 2.2.3 with the Young's modulus decreasing from 223 GPa to 211.85 GPa (i.e. a 5% reduction). Figure 11 shows the results of these simulations in terms of the EVR PSDs in the vicinity of ω_3 for $c = 0.1125$ m/s. The various EVRs were again padded with zeros to obtain a sufficient frequency resolution.
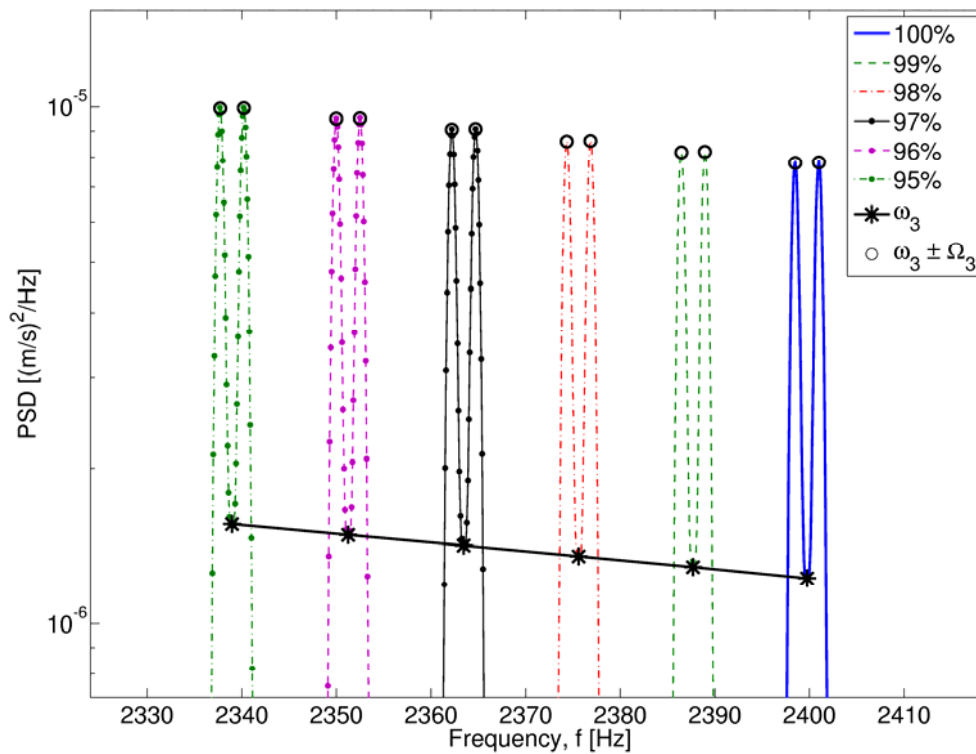
Figure 11: Influence of Young's modulus on EVR PSD around ω_3

From Figure 11 it is clear that natural frequency shifts can indeed be detected with ELDV, making the measurement approach suitable for condition monitoring purposes. Furthermore it is noted that Ω_3 remains constant as W_3 is independent of the Young's modulus of the beam. Slight changes can be expected in Ω_j when structural damage is considered as this may alter the shape of W_j.

2.3 Experimental study of ELDV

Now that ELDV has been thoroughly studied analytically and numerically, it is desirable to confirm the obtained results experimentally. The verification of Equation 7 was done with the use of a simple test setup that consisted of a cantilever beam mounted with a VibroPet electrodynamic shaker on a chassis running on rails. A load cell was also installed at the excitation point and translation of the chassis was accomplished via a draw wire assembly. This piece of equipment was chosen as it contains a torsional spring which provided an approximate constant pulling force. The draw wire assembly further gave feedback of the chassis position on the rails and the translational velocity of the chassis could subsequently be obtained. The translation speed of the chassis was controlled with the aid of counterweights and out-of-plane vibration of the cantilever beam was measured with an Ometron LDV. The LDV was positioned over a section of the rails where the translation speed of the cantilever beam was approximately constant. Figure 12 shows the experimental setup along with the diagram given in Figure 13.

The natural frequencies and matching mode shapes of the cantilever beam was obtained from static modal testing during which the VibroPet shaker was used for excitation while a Polytec SLDV was used as a transducer. The first six ω_js are listed in Table 3 along with descriptions of the matching mode shapes.

Table 3: Identified beam natural frequencies

j	*Frequency [Hz]*	*Description*
1	120	1st lateral
2	546	2nd lateral
3	1184	1st torsional
4	1900	3rd lateral
5	6197	4th lateral
6	15090	2nd torsional
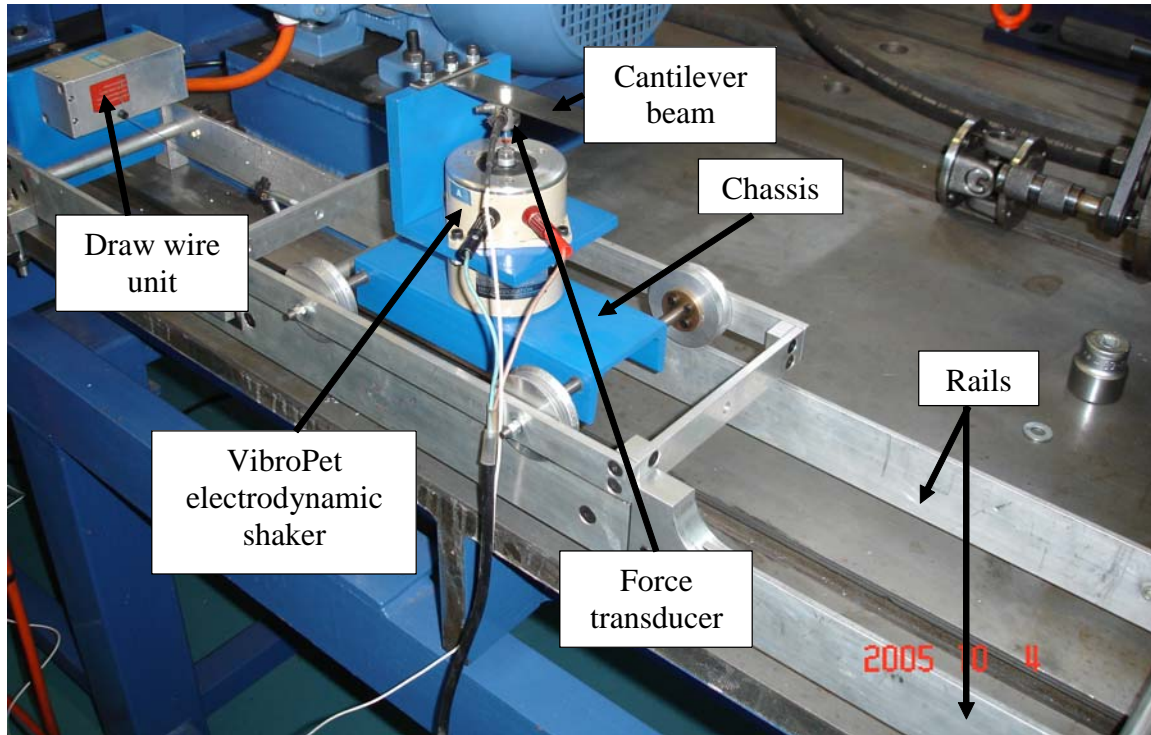
Figure 12: Experimental setup of translating cantilever beam
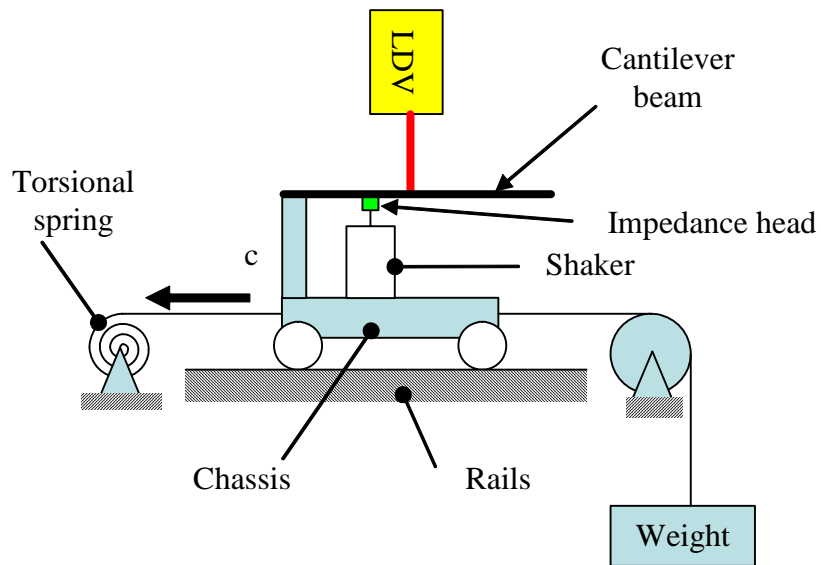
Figure 13: Experimental setup diagram

2.3.1 Discrete frequency excitation

To verify the amplitude modulation phenomenon of ELDV, the beam was excited discretely at several frequencies close to its natural frequencies while translating at approximate constant scanning speeds within 3% of 0.463 m/s. Figure 14 shows the EVRs at excitation frequencies of 200 Hz, 500 Hz, 1900 Hz and 6300 Hz. By simple amplitude demodulation of the EVRs by their respective excitation frequencies, the approximate ODSs of the beam are obtained at these frequencies as seen in Figure 14. These ODSs correspond very well with the W_js of Figure 8. The discrepancy close to the second nodal point of the ODS at 6300 Hz is present as the excitation location was close to this nodal point. It can also be observed from Figure 14 that the effects of speckle noise become more prominent as the structural response frequencies increase and the response amplitudes decrease accordingly. Since the speckle noise level will remain unchanged at the different frequencies, a decrease in structural response amplitude will result in a reduction of the SNR as is observed from the figure.
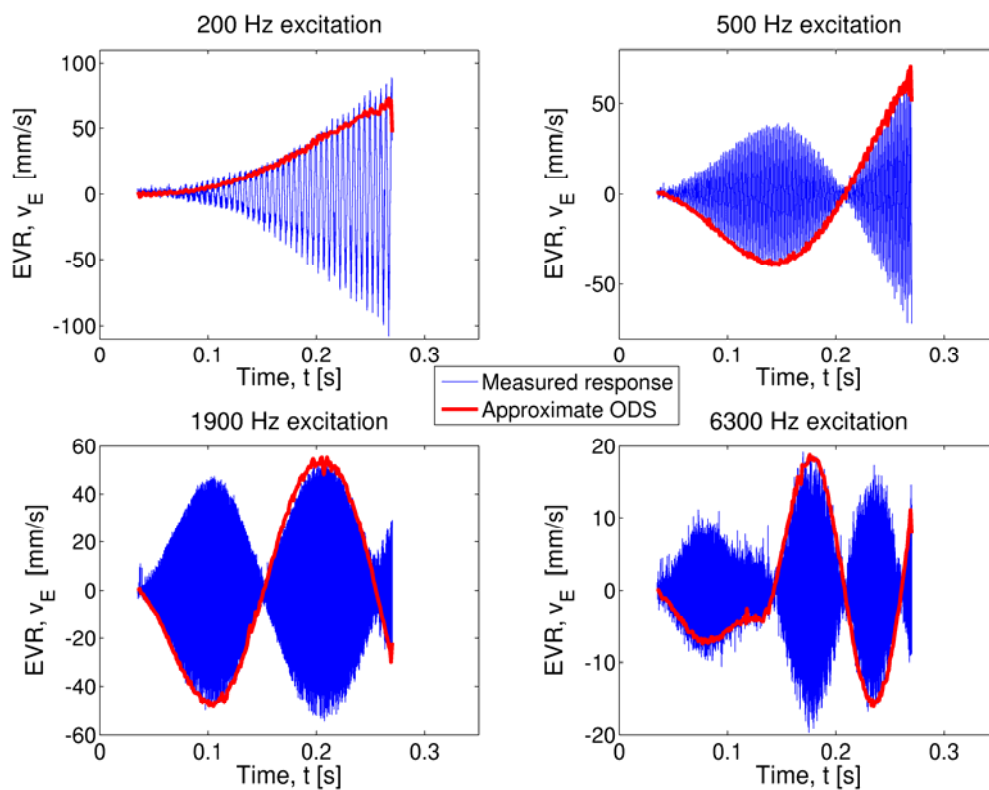
Figure 14: Approximate beam ODSs at discrete frequencies using discrete frequency excitation

The ODSs could also have been obtained by multiplying each EVR with an in-phase and quadrature signal at the relevant excitation frequency (Stanbridge and Ewins, 1999). Modal analysis can furthermore be conducted on these measurements if so required.

2.3.2 White noise excitation

Next, to determine whether structural natural frequencies can be identified directly from ELDV measurements, measurements were taken on the test setup using white noise excitation. The scanning speed of the beam was kept within 6 % of 0.539 m/s. Figure 15 depicts the EVR mobility FRF amplitude (H) and phase angle (ϕ) for 25 averages. Several peaks are evident in the FRF amplitude curve in correspondence with phase angle jumps. These peaks correspond well with the identified natural frequencies of Table 3. However, Stanbridge and Ewins (1996) infer that this FRF cannot be used for modal analysis purposes. According to these two authors, sinusoidal scan rates are required for this purpose along with narrow-band excitation. Wideband excitation cannot be used in this application for modal testing purposes as it will result in sideband overlap.
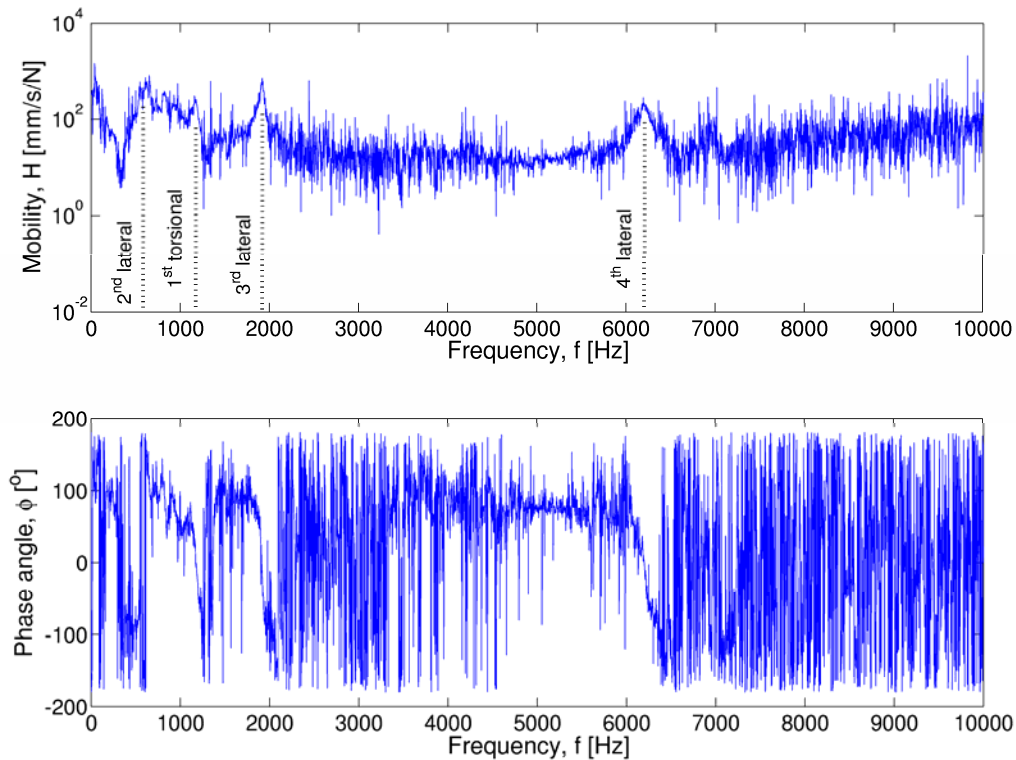
Figure 15: Spatial averaged frequency response function

When the time domain measurements are amplitude demodulated in bands of 50 Hz, the average ODSs over these bands can be extracted as shown in Figure 16. The ODSs corresponding to the various mode shapes are clearly visible in the vicinity of the corresponding natural frequencies. The first torsional mode shape exhibits itself as a first bending mode shape as seen from the ODSs in Figure 16 in the vicinity of the beam's first torsional natural frequency.
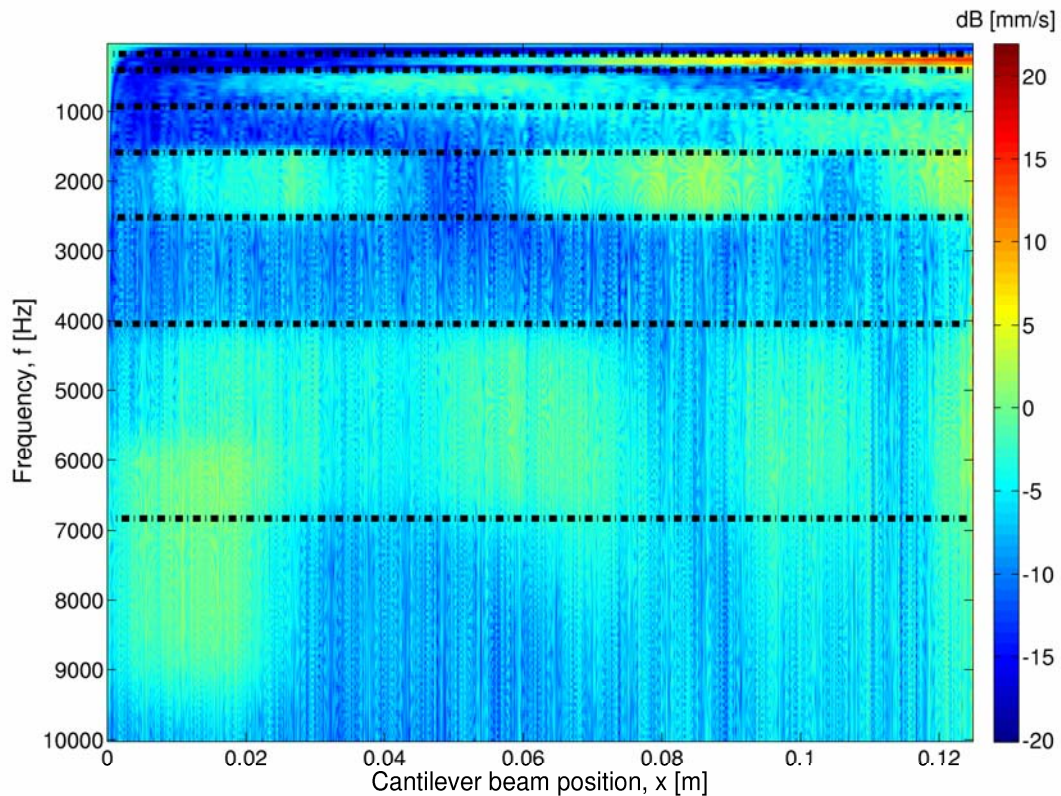
Figure 16: Approximate ODS amplitudes over 10 kHz with white noise excitation

Thus not only can structural natural frequencies be obtained from constant scanning speed ELDV measurements when white noise excitation is employed, but it is also possible to extract ODSs over the entire measurement bandwidth from these measurements.

2.4 ELDV on rotating axial-flow blades

Section 2.2 and Section 2.3 were concerned with ELDV on longitudinally translating cantilever beams. In this section, ELDV on rotating axial-flow blades is studied. This can be accomplished by measuring either sideways blade vibration in the rotor-circumferential direction, or flapwise blade vibration in the rotor-axial direction. These two approaches are discussed below.

2.4.1 Rotor-circumferential ELDV

With this measurement approach the laser beam is aligned parallel to the rotation plane of the rotor, thereby measuring blade sideways vibration as depicted in Figure 17. However, the ELDV scanning speed will no longer be constant as can be shown

mathematically with the aid of a vector-loop diagram of the measurement setup (Figure 18).
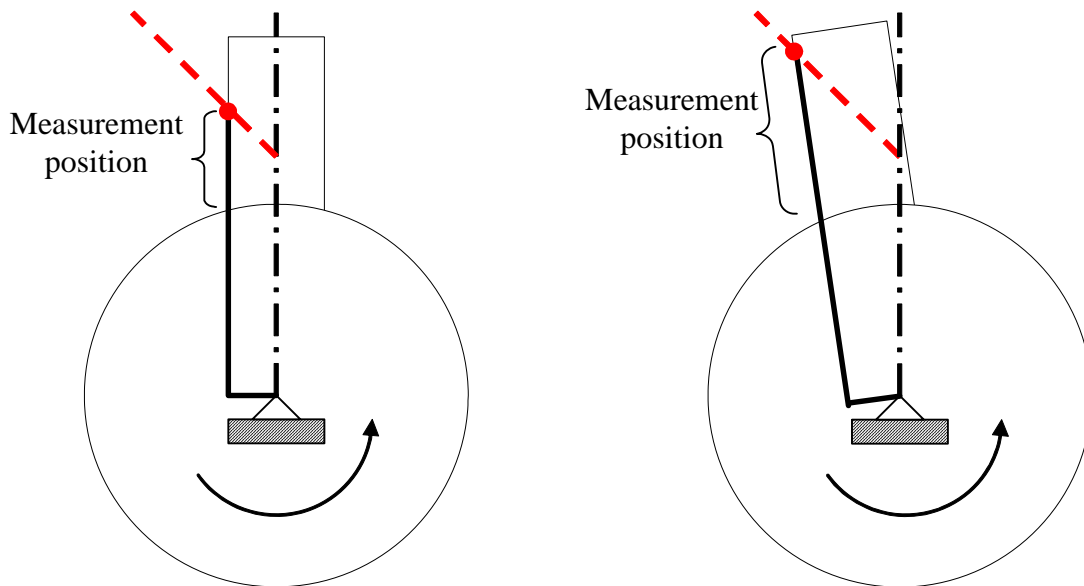
Figure 17: Effect of blade rotation on ELDV measurement position
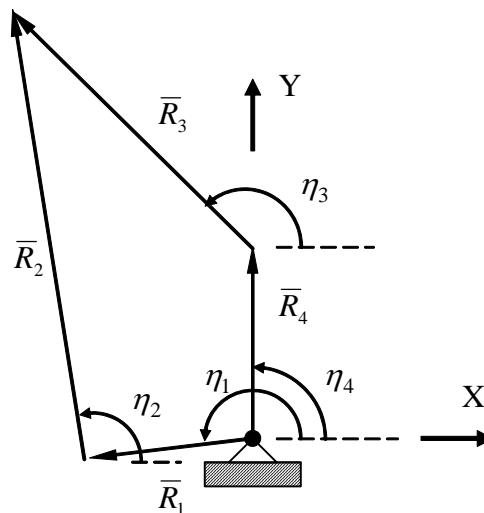
Figure 18: Rotor-circumferential ELDV: Vector-loop diagram

In Figure 18, $\overline{R}_1$ is defined as the perpendicular vector from the blade leading edge to the rotor centre and $\overline{R}_2$ describes the ELDV measurement position on the blade leading edge relative to $\overline{R}_1$. $\overline{R}_3$ and $\overline{R}_4$ describe the laser beam orientation. Using vector-loop equations (Appendix A), it is shown the scan speed $\dot{R}_2$ is affected by the shaft rotation angle:

$$\dot{R}_2 = \frac{2\dot{\theta}_1 R_1 - \dot{\theta}_1 R_4 \sin\theta_1 - \dot{\theta}_1 R_4 \sin(\theta_1 - 2\theta_3)}{\cos(2\theta_1 - 2\theta_3) + 1}$$

Equation 19

It can furthermore be shown analytically and experimentally that this measurement approach introduces a Rigid Body Velocity Component (RBVC) into the measurements. This RBVC v_{RB} manifests itself as a DC offset in the measurement which depends on the rotor frequency ψ as well as the LDV orientation:

$$v_{RB} = -2\pi\psi \cdot R_4 \cos\theta_3$$

Equation 20

Experimental measurements on a single blade rotor are shown in Figure 19 and a lower limit DC drift can be observed. This phenomenon is most likely caused by the control system characteristics of the SLDV used. Further work is necessary to determine whether this measurement approach is feasible.

2.4.2 Rotor-axial ELDV

A simpler approach to perform ELDV on rotating axial-flow blades is to align the LDV parallel to the shaft rotation axis, thereby measuring blade flapwise vibration. In this measurement approach the rotating blade needs to be considered as a cantilever plate undergoing angular translation. Equation 5 and Equation 7 will change to represent the vibration of a plate (Leissa, 1969), whereas the interpolation procedure remains largely unchanged.

To extend the interpolation scheme to a rotating plate, it is convenient to construct a LVRM in a polar coordinate system consisting of LVRs at angular measurement positions $\varphi_{L,n}$ corresponding to a reference rotor speed ψ_{ref} :

$$\hat{V}_{L,\psi_{ref}} = \begin{bmatrix} \vec{v}_{L,\varphi_0} \\ \vec{v}_{L,\varphi_1} \\ \vdots \\ \vec{v}_{L,\varphi_{N_{ref}}} \end{bmatrix} = \begin{bmatrix} v_L(\varphi_0, t_0) & v_L(\varphi_0, t_1) & \cdots & v_L(\varphi_0, t_{N_{ref}}) \\ v_L(\varphi_1, t_0) & v_L(\varphi_1, t_1) & \cdots & v_L(\varphi_1, t_{N_{ref}}) \\ \vdots & & \ddots & \vdots \\ v_L(\varphi_{N_{ref}}, t_0) & v_L(\varphi_{N_{ref}}, t_1) & \cdots & v_L(\varphi_{N_{ref}}, t_{N_{ref}}) \end{bmatrix}$$

Equation 21
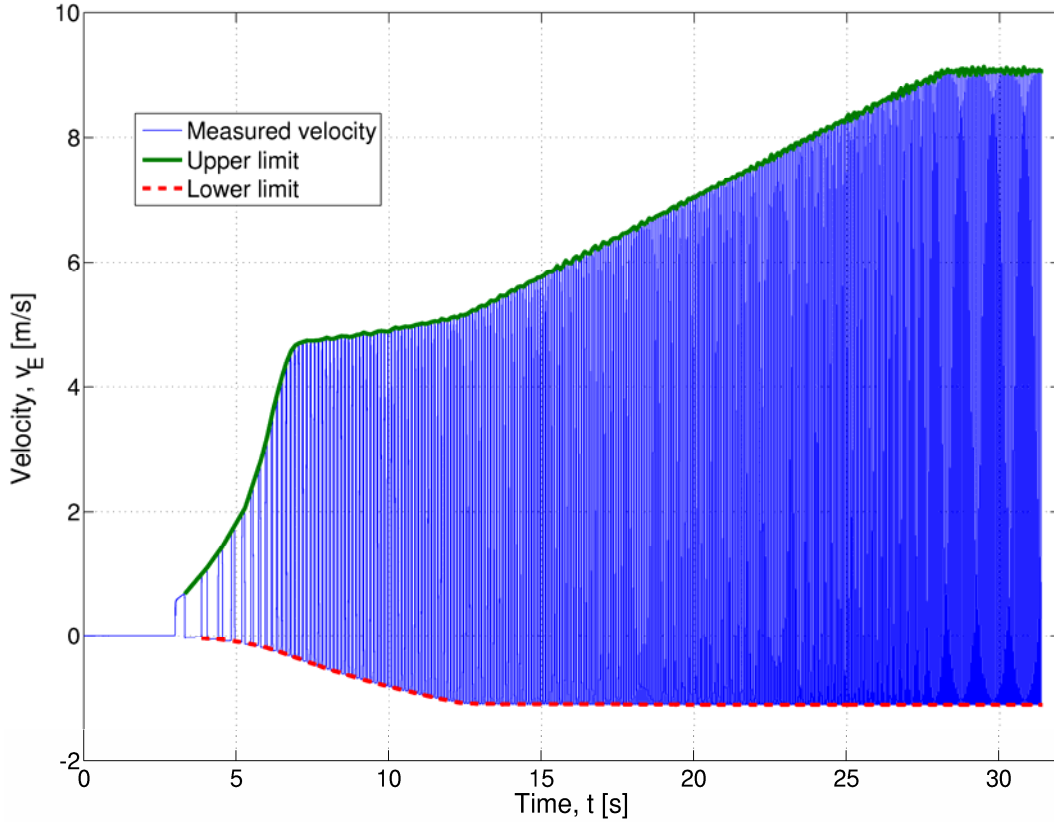
Figure 19: Rotor-circumferential ELDV: Lower limit DC drift

with $\varphi_{L,n} = \psi_{ref} t_n$ and $N_{ref} = \lfloor \vartheta / (\psi_{ref} \cdot \Delta t) \rfloor$. The measurement radius is given by r and the angular measurement range on the blade is represented by ϑ .

The polar coordinate EVR vector $\vec{v}_{E,k\cdot\psi_{ref}}$ can then be obtained at angular positions $\varphi_{E,n} = k \cdot \omega_{ref} t_n$ by appropriate interpolation on $\hat{V}_{L,\psi_{ref}}$ for $k = \psi / \psi_{ref}$ and $N_k = \lfloor N_{ref} / k \rfloor$ (see Figure 20).

2.5 Conclusions

In this chapter, the characteristics of ELDV were studied in depth for longitudinally translating cantilever beams. Using the continuous beam Euler-Bernoulli formulation, it was shown that measurements obtained with ELDV consist of the combined effects of the amplitude modulation of the various cantilever beam generalized coordinates by their respective (and now time-dependent) characteristic functions. This was verified experimentally.
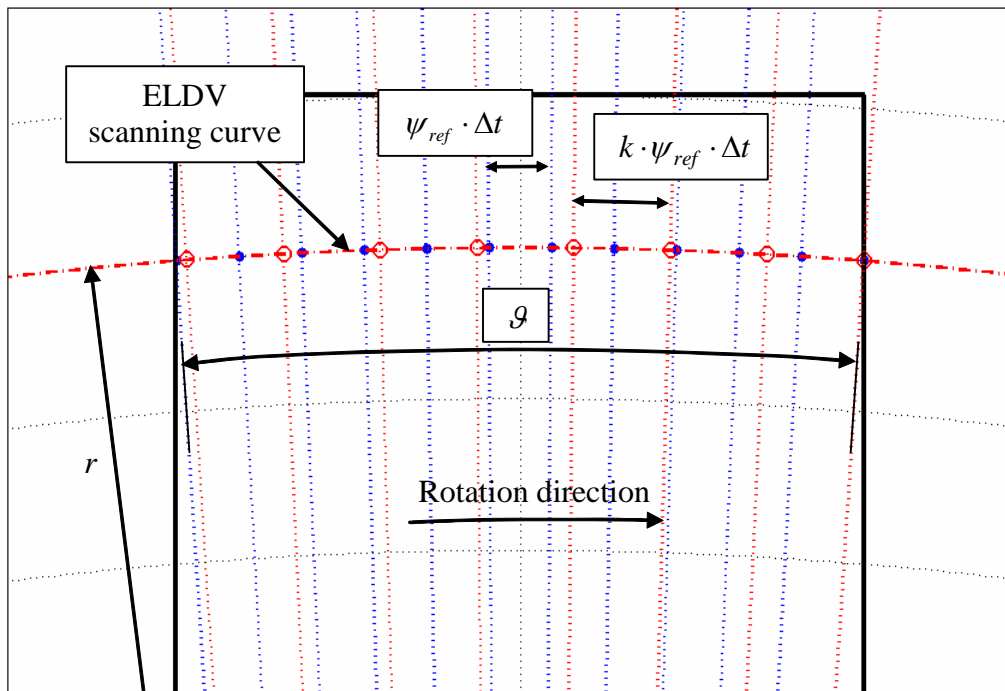
Figure 20: LVRM and EVR measurement positions for a rotating blade

The numerical simulation of ELDV was studied next. It was shown that an ELDV signature can directly be obtained from a LVRM when the ELDV scanning speed is an integer multiple of the LVRM scanning speed. When the scanning speed is not an integer multiple, it was shown that the ELDV signature can be approximated accurately with the aid of cubic spline interpolation on the LVRM.

Two approaches for the implementation of ELDV on rotating axial-flow blades were studied namely rotor-circumferential and rotor-axial ELDV. The first approach results in a non-constant ELDV scanning speed and a rotor speed dependent offset is inherent to the measurements. Rotor-axial ELDV however is a much simpler approach as the scan speed remains constant for a fixed rotor speed and no additional components are introduced into the measurements. Using polar coordinates, the interpolation scheme proposed in Section 2.2.3 is easily applied to this measurement approach. It is this measurement approach that this thesis is concerned with.

The work of this chapter is summarized in the article titled *"Online condition monitoring of axial-flow turbomachinery blades using rotor-axial Eulerian laser Doppler vibrometry"* (Oberholster and Heyns, 2009).

Chapter 3 Rotor-axial Eulerian Laser Doppler Vibrometry applied to a single-blade axial-flow test rotor

3.1 Introduction

In this chapter, the application of rotor-axial ELDV to the condition monitoring of axial-flow blades is studied using a single-blade test rotor. ELDV as well as TLDV measurements were recorded at a fixed rotor speed for various damage levels, simulated by means of slot cuts into the blade leading edge close to the blade root. Various signal parameters were considered as possible damage indicators and with the aid of the TLDV measurements, it was found that vibratory phase angle change is indicative of blade damage. After this phenomenon is studied with the aid of FEM simulations, Non-Harmonic Fourier Analysis (NHFA) is studied in depth as a signal processing technique applicable to the ELDV measurements.

NHFA is then applied to the experimental ELDV measurements and is compared with NHFA results from FEM ELDV simulations. It is shown both experimentally and numerically that NHFA applied to rotor-axial ELDV measurements is capable of providing indicators of blade health deterioration.

3.2 Experimental setup

The test rotor depicted in Figure 21 was used to investigate the condition monitoring capabilities of the ELDV measurement technique described in Section 2.4.2. The rotor was driven with a speed-controlled motor and consisted of a solid shaft (supported by two bearings) with a hub and a single flat, straight blade. A Heidenhain ERN 120 shaft encoder provided accurate rotor angular position feedback during testing and the blade was dynamically perturbed during rotation by means of a compressed air-jet. A piezoelectric dynamic pressure sensor installed close to the nozzle, measured the back-pressure at the nozzle arising from the airflow blockage caused by the blade during rotation. Stationary modal testing was performed on the rotor prior to testing for the purpose of FEM updating.

During testing the blade vibrations were measured with a Polytec PSV300 SLDV which was axially aligned with the shaft centre as shown in Figure 22. A sensitivity of 125 mm/s/V was used and the tracking filter option was disabled due to the nature of the measured signals. A 100 kHz low-pass filter was selected on the controller. High-efficiency reflective material was attached to the blade near the blade tip, to

ensure a sufficiently strong LDV signal (Figure 23). Damage was simulated in the test rotor using a slot cut *in situ* into the leading edge of the blade close to the blade root, with slot depth increments of 1 mm, using a 1-mm thick cutting disc on a high-speed rotary tool. This of course is a worst case scenario in terms of blade damage. Since the focus of this thesis is to demonstrate the ELDV measurement technique as a condition monitoring tool, the effects of the location and nature of the damage (i.e. damage simulation that represents cracks more closely) is reserved for further work.
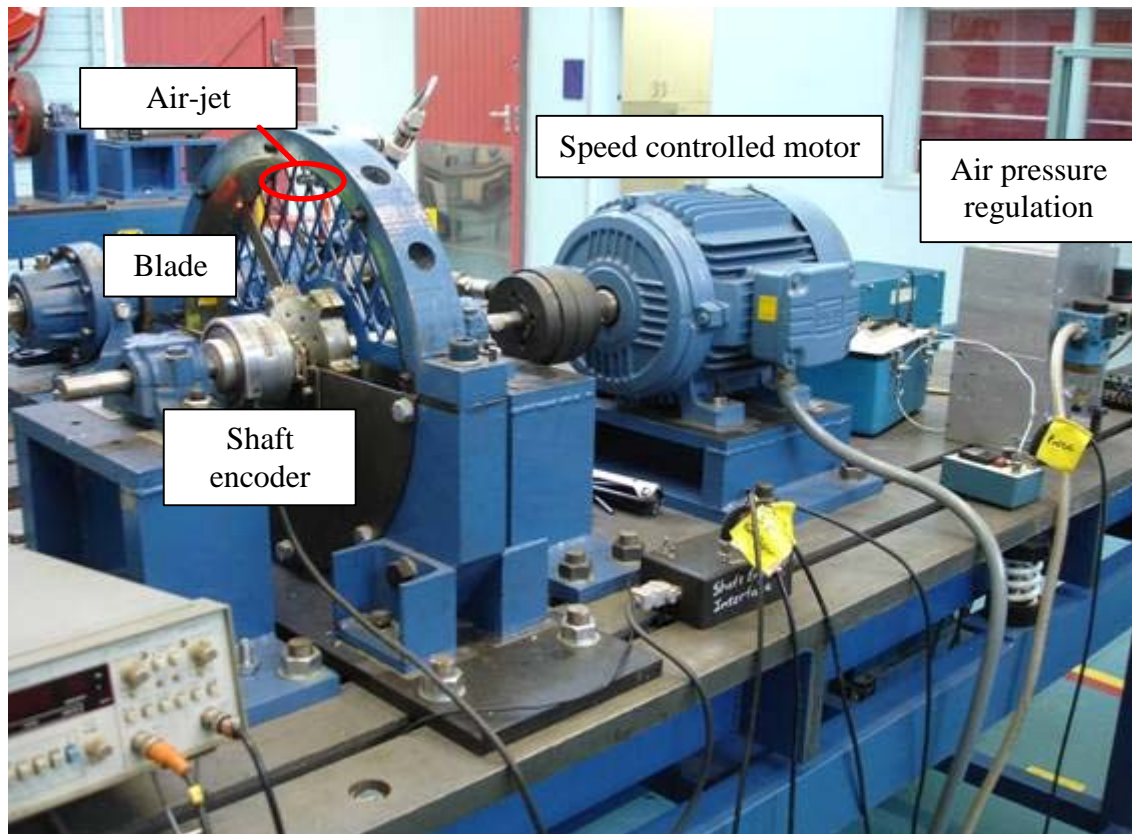
Figure 21: Experimental setup
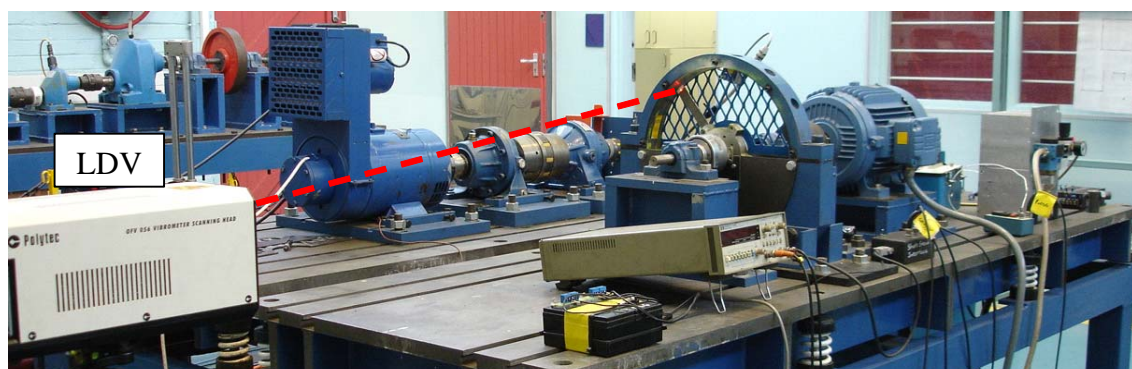
Figure 22: LDV orientation
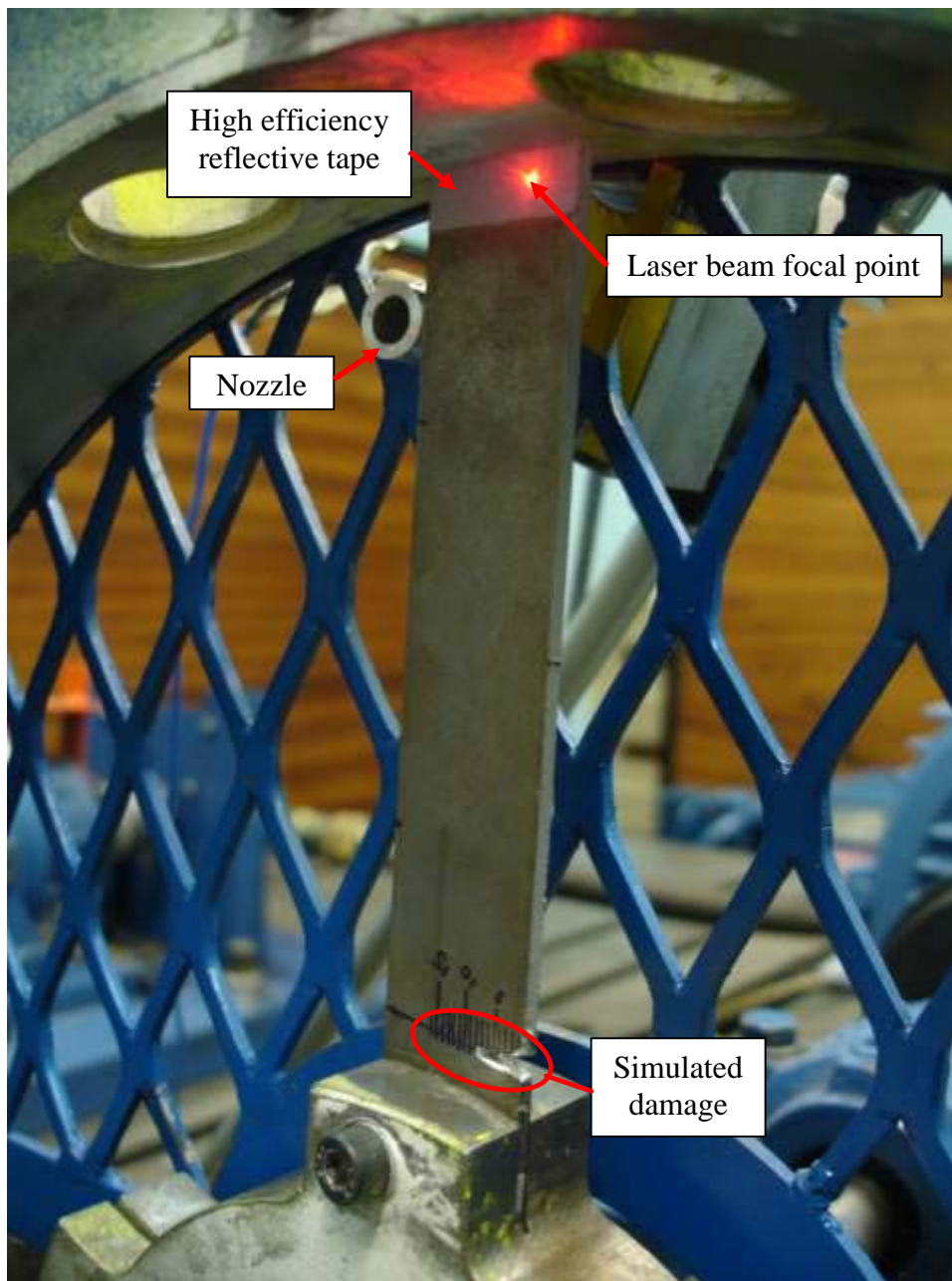
Figure 23: Test setup detail and typical ELDV measurement location

Initial testing was conducted on the rotor at 600 RPM during which only ELDV measurements were recorded. Various signal processing techniques were applied to the measurements, although repeatable results could not be found. These techniques included Burg spectrum estimation, ARMA modelling and AR modelling. Also a frequency domain filter technique was evaluated (Antoni and Randall, 2004a; Antoni and Randall, 2004b).

As the short time span of the ELDV measurements creates difficulties in interpreting the measurements (2.24 ms for 600 RPM resulting in a frequency resolution Δf = 446 Hz), it was decided to record TLDV measurements on the blade during subsequent testing. TLDV is a Lagrangian implementation of laser Doppler vibrometry where the two perpendicular scanning mirrors of the SLDV are controlled to follow a specific point on the rotor during rotation. Thus a vibration signal is yielded over a longer period, giving insight into the dynamic behaviour of the blade during rotation. This furthermore allows the calculation of FFTs and PSDs on the TLDV data with satisfactory frequency resolutions.

3.2.1 Measurement and control

The two scanning mirrors of the Polytec PSV300 vibrometer are mounted on independently controlled servo motors, allowing the mirrors to be tilted on axes perpendicular to each other. The scanning mirror tilt angles (and subsequently the laser beam orientation) can be externally controlled by applying voltage signals to the servo motors. This was performed with a National Instruments PCI-6110 card using the 5000 Pulses-Per-Revolution (PPR) shaft encoder pulses to increment the position of two 90° out-phase sine wave lookup tables, thereby allowing the description of a circular scanning curve as can be seen in Figure 24.

Due to the mechanical response characteristics of the servo-mirror assemblies, it was necessary to adjust the phases and amplitudes of the two control signals for various rotation speeds. In order to streamline the experimental testing procedure, the 1 PPR shaft encoder signal was used to determine the shaft rotation speed. A look-up table containing the various phase angles and amplitudes at predefined rotation speeds was then used for the relevant adjustments.

Control of the National Instruments PCI-6110 card was accomplished with LabView 8, allowing the simultaneous control of the servo motors and the recording of data. A summary of the terminal configuration of the National Instruments connector used is given in Table 4. A sampling frequency of 1 MHz was used to enable the sufficient capturing of the shaft encoder 5000 PPR signal waveform, which had a frequency of about 60 kHz at 720 RPM. The layout of the LabView Virtual Instrument (VI) that was designed consisted of three main sections namely servo motor control, data acquisition and data management as depicted in Figure 25.
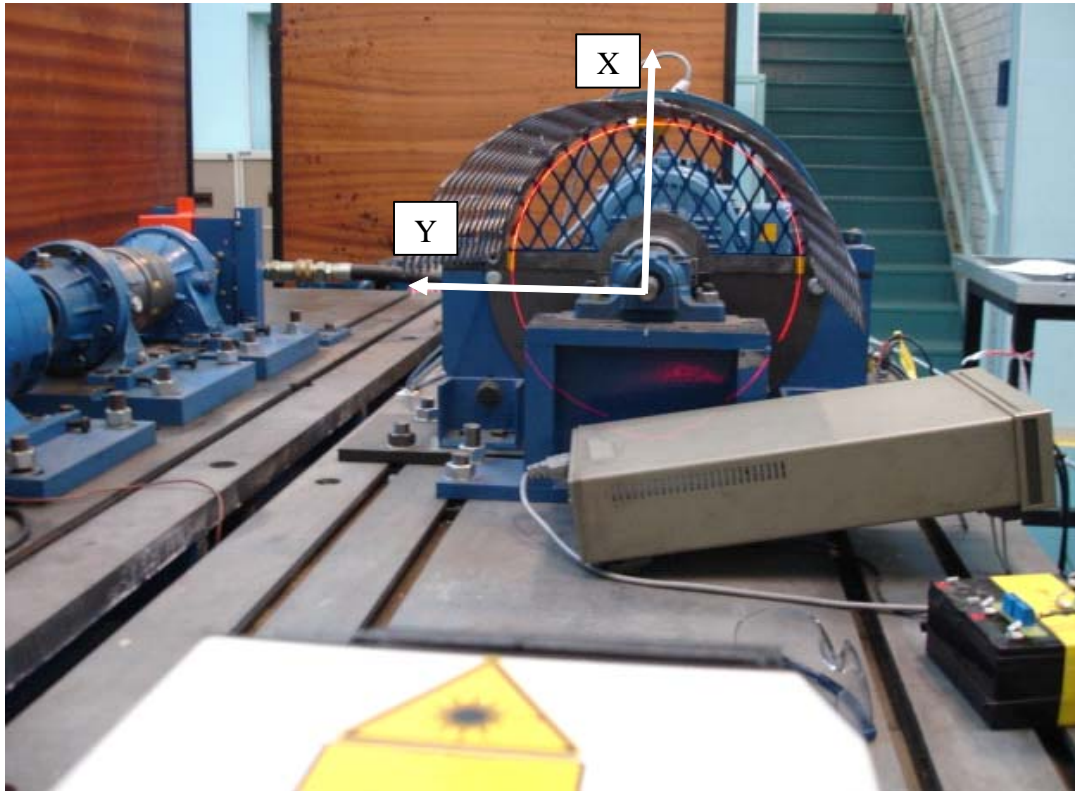
Figure 24: TLDV mirror control

Table 4: National Instruments BNC-2110 terminal configuration

Analogue Inputs
• Dynamics pressure signal
• SLDV signal
• Shaft encoder 5000 PPR signal
• X mirror control signal
Analogue Outputs
• X mirror control signal
• Y mirror control signal
Digital Inputs
• Shaft encoder 1 PPR
o Measurement trigger: Analogue inputs
o Trigger: Mirror control signals
o Rotation speed measurement
• Shaft encoder 5000 PPR
o Clock signal: Mirror control signals
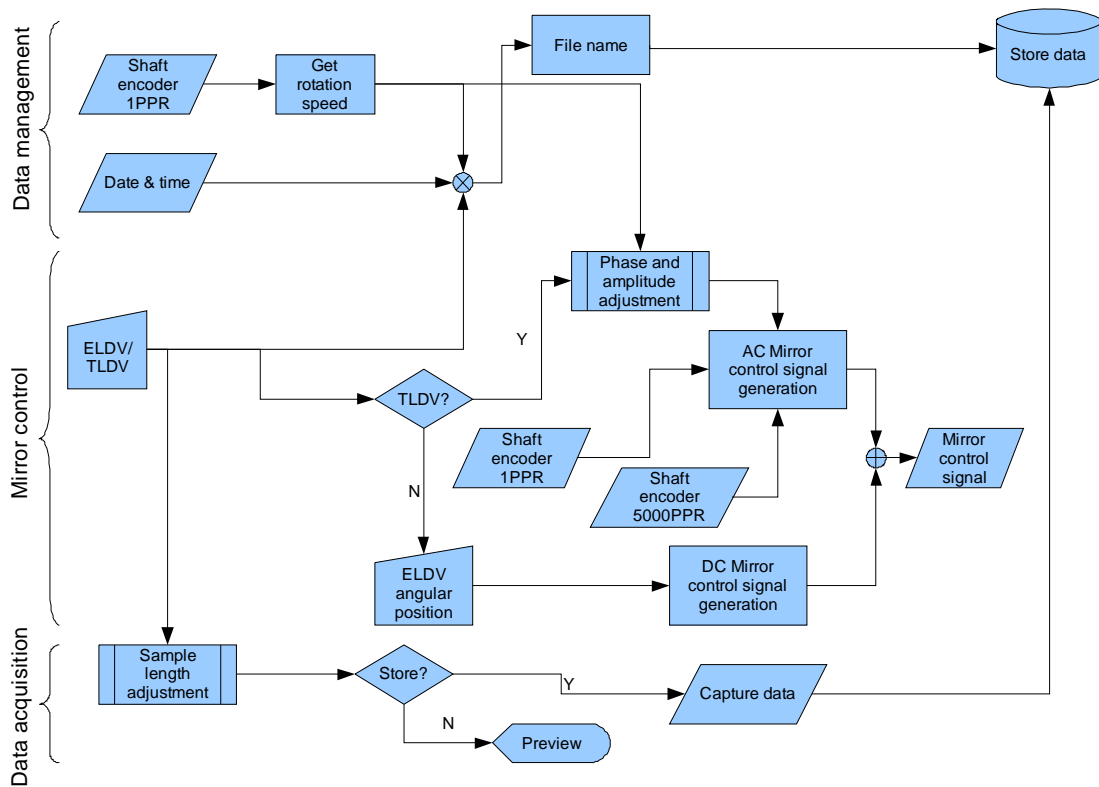
Figure 25: LabView VI flow diagram

An open-loop control methodology was implemented for TLDV control (Figure 25) and as a result the VI was found to have varying lower rotation speed control. Accurate control was possible from 720 RPM and upwards, and for this reason testing was conducted at 720 RPM to obtain the maximum sample lengths. For ELDV measurements DC output signals were supplied to the mirror servo motors corresponding to the desired measurement location. During ELDV measurements, the laser beam was orientated as such as to allow for the measurements to coincide with the positive slopes of the pressure pulses as shown in Figure 26.

3.2.2 Laser alignment

To minimize any TLDV misalignment effects, care was taken in aligning the SLDV with the rotor (Halkon and Rothberg, 2006:1295). Alignment was performed in terms of SLDV pitch, roll and yaw using two approaches. Firstly angular alignment between the SLDV XY-plane and the shaft rotation plane was achieved by controlling the SLDV mirrors to describe a circle with the laser. When misalignment exists, an elliptical scanning curve is observed on the rotor reference plane whereas a circular scanning curve is visible when alignment is sufficient. When the SLDV mirrors are controlled in order to describe a crosshair pattern, it is then possible to align the

SLDV zero position with the shaft centre. The ZX and ZY- planes were also aligned in this way.
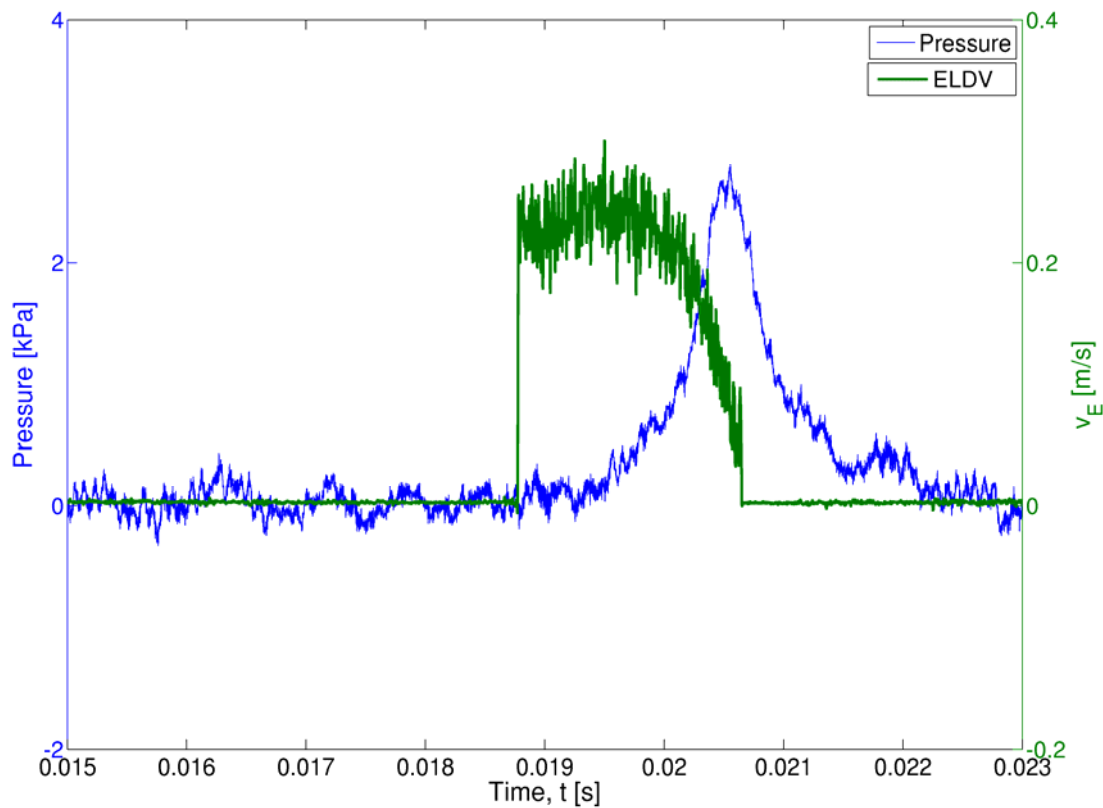
Figure 26: ELDV signature and pressure pulse time histories

Some degree of misalignment is however unavoidable even if great care is taken during the alignment process. According to Halkon and Rothberg (2006) the DC, 1× and 2× components of the scanning frequency (in this case, rotor speed) will be most affected by the misalignment effects. Since these components were well below the first blade bending natural frequency, the TLDV signals were high-pass filtered using a 2nd order Butterworth filter with a cut-off frequency at 50 Hz. Zero-phase digital filtering was employed to eliminate signal phase distortion.

The small misalignment effects will also influence ELDV measurements by introducing a DC component proportional to the rotor speed. Due to the very short nature of the signals considered, it was not possible to high-pass filter the signals without causing signal distortion. Since testing was conducted at a fixed rotor speed, this DC component will be the same in all the measurements. By calculating trends relative to a reference signal, it should be possible to minimize this effect.

3.3 Experimental measurements

The experimental ELDV and TLDV measurements recorded at 720 RPM are depicted in Figure 27(a) and Figure 27(b) respectively for the different damage levels (D_b) considered. Although some amplitude and phase angle changes are visible in the ELDV measurements, it is otherwise difficult to visually interpret the measurements. The TLDV measurements in Figure 27(b) however give further insight into the ELDV measurements. The TLDV measurements are clearly dominated by the first natural frequency of the blade. A systematical change in the vibration phase angle can be observed with increasing damage level except at the 10 mm and 15 mm damage levels. At these two damage levels, phase discontinuities are observed along with sudden amplitude increase (corresponding well with the ELDV measurements). It is shown in Chapter 4 that at both these damage levels, the first blade bending natural frequency has decreased to such extent as to coincide with rotation orders.
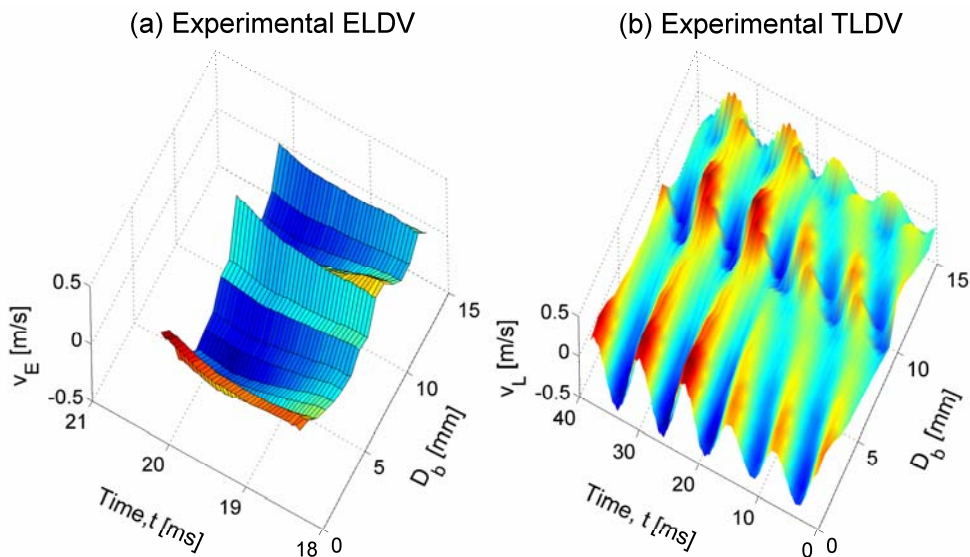
Figure 27: Experimental ELDV and TLDV measurements

3.4 Finite element model

An accurate FEM is required to fully understand the vibration behaviour of the test rotor in terms of its transient responses and natural frequencies. Figure 28 shows the FEM that was constructed using mainly shell and beam elements. A very fine nodal resolution was specified along the corresponding ELDV scanning curve on the FEM for ELDV measurement simulation as depicted in Figure 29(a).
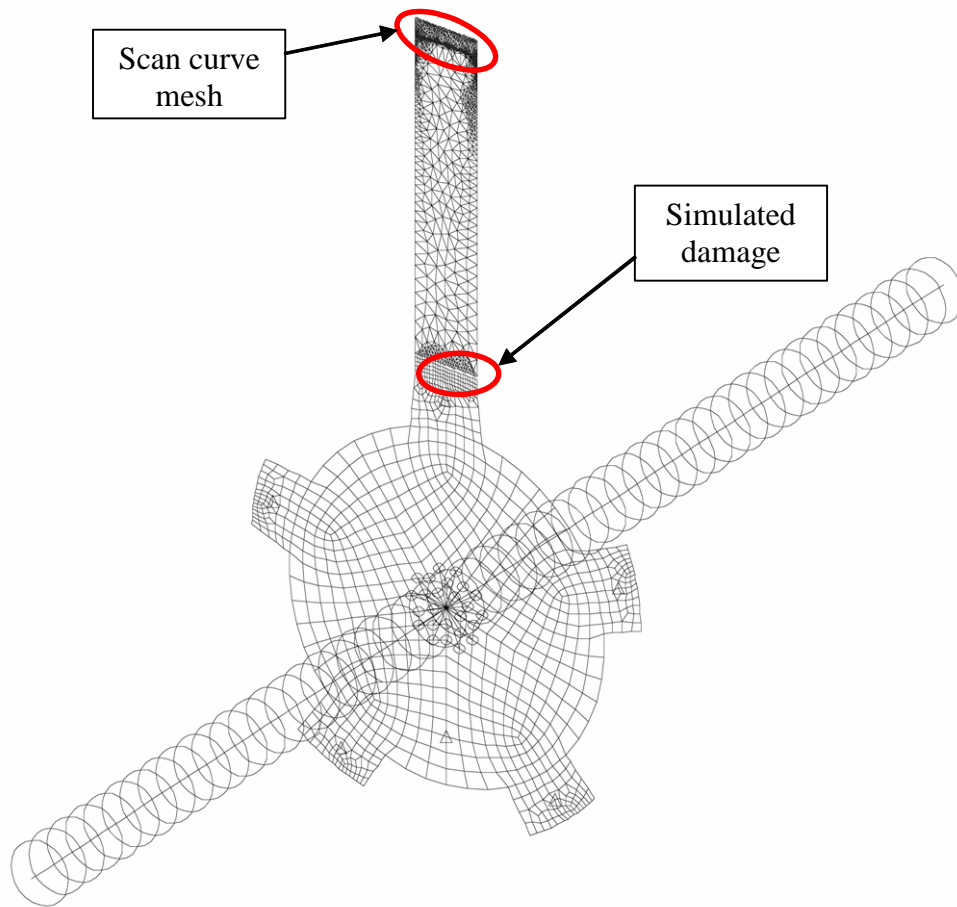
Figure 28: Test rotor FEM

A total of 500 nodes were used along this curve in order to yield an LVRM from which an EVR, containing at least one full period of the blade's first natural frequency, could be directly obtained. To represent the different damage levels induced in the test rotor blade, the element sizes of the FEM at the damage location were chosen so as to allow damage simulation in the FEM by simply deleting the appropriate elements, as shown in Figure 29(b).

Stationary experimental modal testing was conducted on the test rotor using a modal hammer for excitation and a Polytec PDV100 laser vibrometer for measurement of the responses. Following this, FRF-based model updating over a bandwidth of 10 kHz was performed and the results are shown in Figure 30 for the excitation point FRF. The noise that is present in the experimental FRF is attributed to the surface preparation that was used, i.e. developer spray. Opto-reflective material would have

decreased the noise level. The FRF quality was however of sufficiently good quality for the modal updating approach used.

a) Scan curve mesh b) Simulated damage
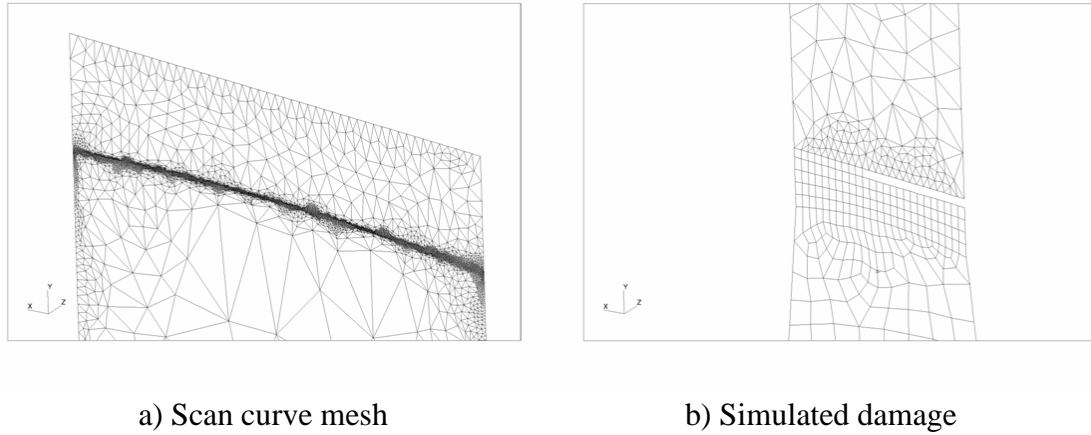
Figure 29: Mesh resolution at scanning curve
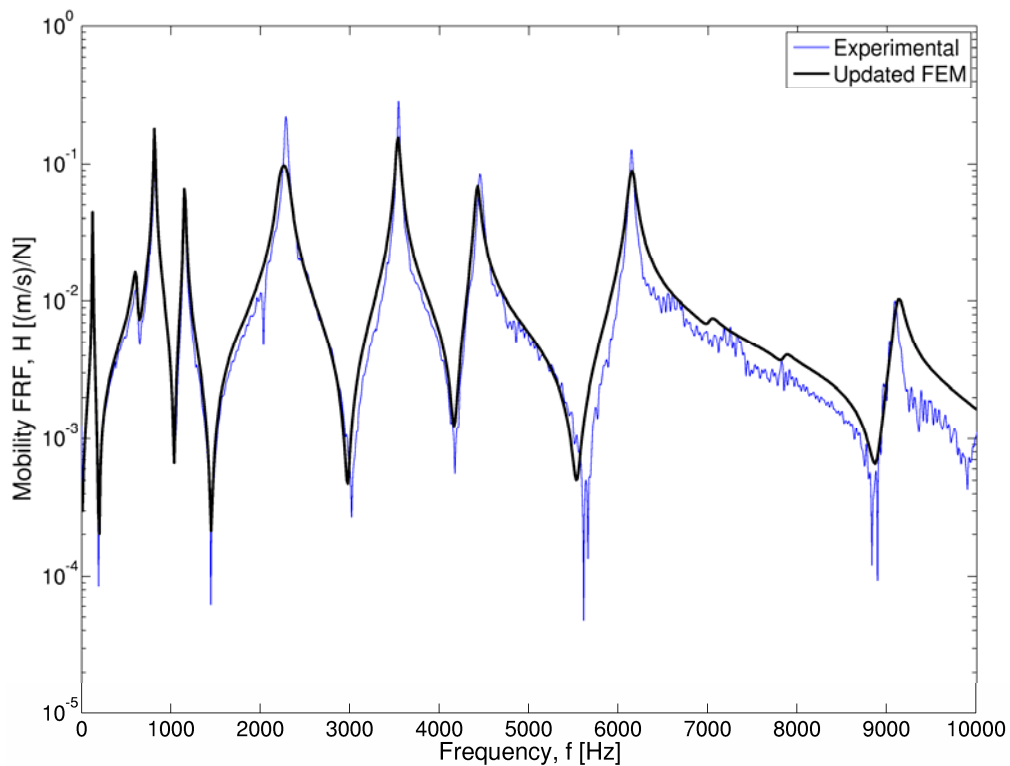
Figure 30: Experimental and FEM FRF comparison

The damage modelling approach in the FEM was also verified by comparing the FEM natural frequencies with the peak frequencies from experimental TLDV PSDs at the various damage levels (Figure 31). This figure shows clear correlation in terms of

frequency shifts, indicating that the FEM was successfully updated and that the FEM damage modelling was representative of experimental damage.
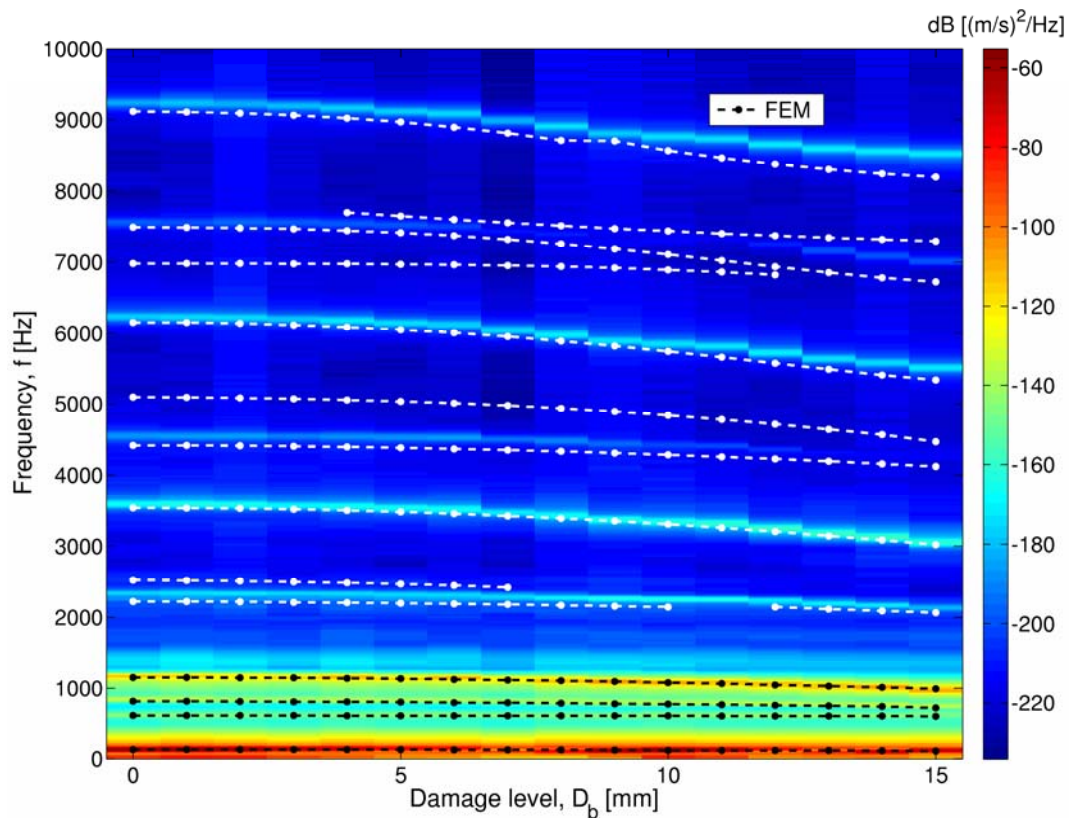
Figure 31: Validation of the FEM damage simulation technique

A linear relationship was found between the air-jet and impact hammer excited responses with the aid of appropriate experimental FRF measurements. Since only linear analysis was used in the FEM calculations, the responses obtained from the FEM could easily be scaled in amplitude to match the experimental measurements. The excitation provided by the air-jet nozzle during rotation was approximated by a single force at a location on the FEM blade, matching the angular position at which the experimentally measured nozzle back-pressure peaked.

Two approaches were evaluated to obtain TLDV and ELDV simulations. The first approach was to perform transient analyses using an average measured nozzle pressure signal as an input force with the FEM initially at rest. The results of the transient analyses on the FEM exhibited the participation of sideways blade vibration modes in the rotor-axial direction. This phenomenon is an artefact of the angular offset between the blade-bending neutral axis and the measurement plane. Since the LDV in use only measures out-of-plane vibrations (within a $\pm 20^{o}$ angular offset

range), these modes have to be discarded to facilitate comparison with the experimental results.

When calculating the FRFs directly from the FEM in the rotor-axial direction, it is possible to suppress the participation of the sideways vibration modes. Using impulse response function calculations on the FRFs, PSDs can be subsequently calculated and scaled. Figure 32 compares the PSD of FEM-simulated TLDV with that from experimental TLDV measurements for an undamaged blade. Good correlation with regards to peak frequency location is observed.
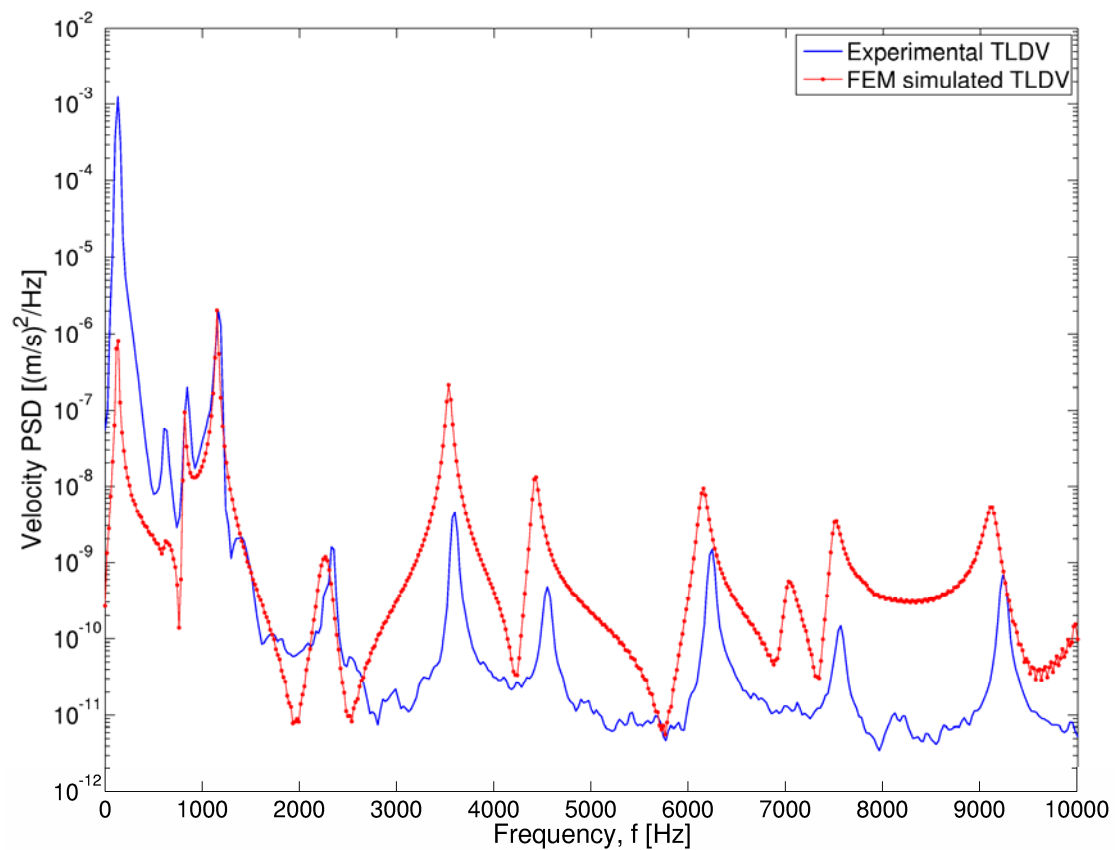
Figure 32: Comparison of experimental and FEM TLDV PSDs

To compare the simulated ELDV time responses with experimental measurements, amplitude-normalized response surfaces are constructed as indicated in Figure 33. Although the correlation is not particularly strong, similar trends are visible. The discrepancies may be attributed to the FEM ELDV simulation approach, which constitutes of impulse responses from calculated FRFs. Thus in comparison to the experimental measurements, the FEM results contain transient vibration behaviour more strongly. Although the damage modelling approach has been validated, small

differences between experimental and FEM damage levels were unavoidable. This will also cause discrepancies between the results.
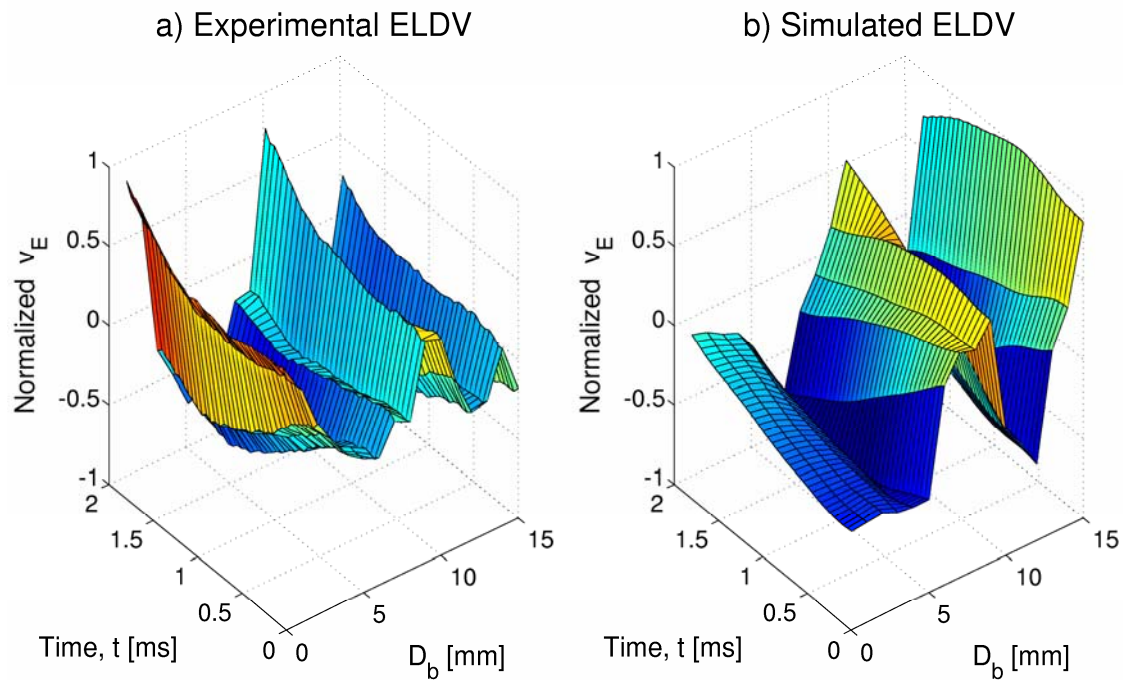

Figure 33: Response surface comparison

3.5 Phase angle as a damage indicator

A systematical change in the vibration phase angle with increasing damage level was observed from the experimental TLDV measurements (Figure 27). Although the applications differ, various literature sources report on using vibratory phase angle as a damage indicator (Jacobs and De Roeck, 2003; King et al., 2006). To investigate this phenomenon for the application this thesis is concerned with, FFTs of simulated TLDV responses were calculated for various damage levels.

Figure 34 shows the FFTs for the first bending natural frequency of the blade. Frequency shifts with increasing damage level are observed albeit small, while the phase angles at the various peak frequencies remain relatively constant. A clear trend is present when the various phase angles are considered at a fixed reference frequency (in this case the peak frequency for the undamaged case). Figure 35 compares the peak frequency and phase angle trend shifts with the latter expressed as a percentage of the total phase angle change around a natural frequency, i.e. 180$^{\text{o}}$.
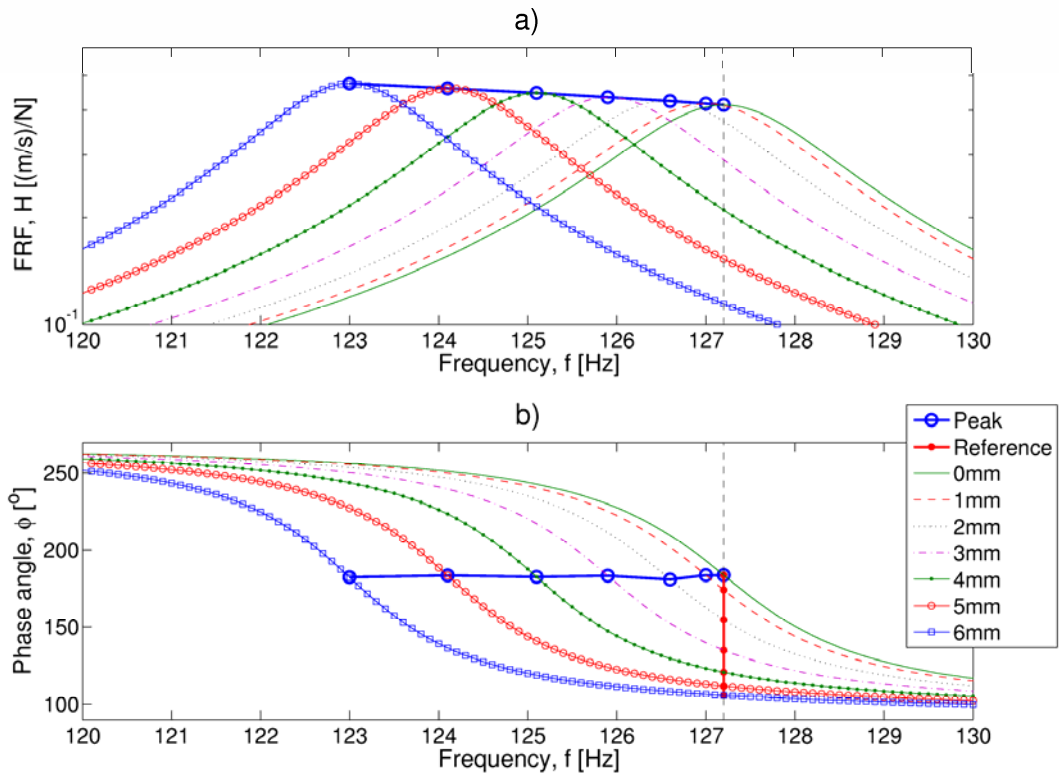
a)

b)

Figure 34: Influence of damage level on peak frequency and phase angle
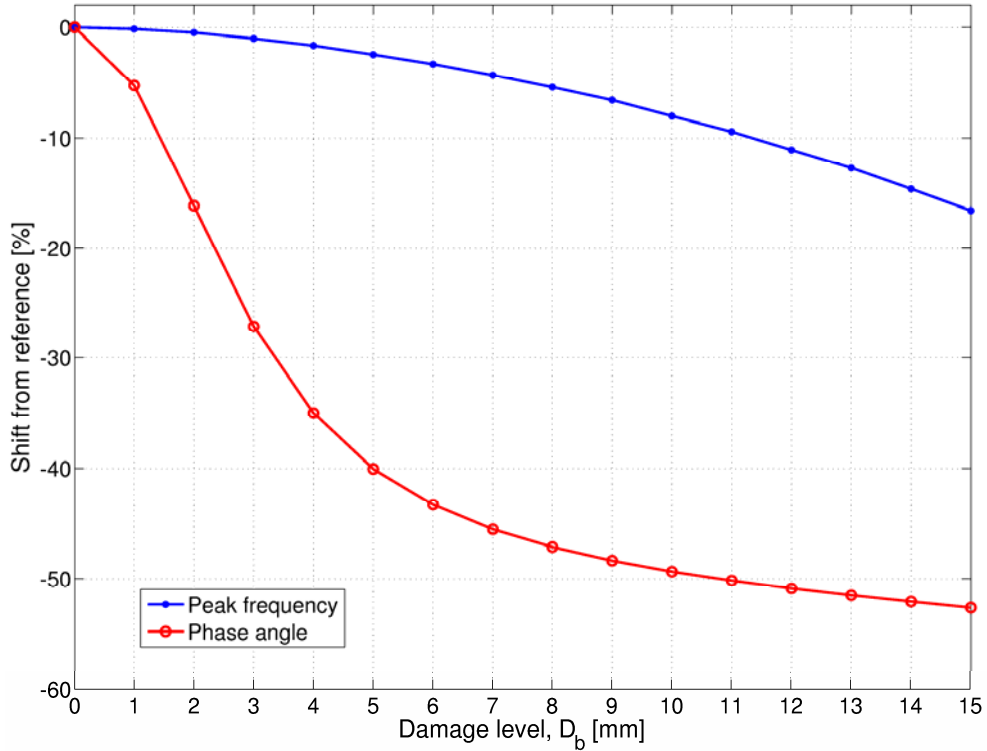

Figure 35: Comparison between peak frequency shift and phase angle shift

From these results and the experimental TLDV measurements, it is clear that phase angle trends of blade vibration signals can indeed be used for condition monitoring purposes. It is thus desirable to extract phase-related information from the ELDV measurements. However the problem remains as how to obtain this information from such short signals. One signal processing technique suitable for this task is NHFA which is discussed in detail in the following section.

3.6 Non-Harmonic Fourier Analysis

Similarly to HFA, NHFA approximates the signal with sine and cosine components although NHFA requires additional normalization components (Hirata, 2005). It is necessary to perform signal component separation to obtain accurate results, although signal components need to be separated by up to 1.6 of the fundamental frequency of the signal to be able to do this (Muraoka and Nishioka, 2004). This requirement renders the signal separation approach proposed by Hirata (2005) impractical for the experimental ELDV measurements based on the stationary modal analysis results. However as shown in this section, this lack of signal separation can be exploited for the purpose of condition monitoring, as it is possible to use the NHFA phase angle at a reference frequency as an indicator of both signal phase angle and frequency shifts.

In HFA, Fourier components are expressed at integer multiples m of the signal fundamental frequency ϖ_0 (in radians per second) in terms of cosine and sine coefficients as shown for an arbitrary time signal y (Rao, 1995:58):

$$y(t) = \frac{a_0}{2} + \sum_{m=1}^{\infty} \left(a_m \cos m\varpi_0 t + d_m \sin m\varpi_0 t \right)$$

Equation 22

with the respective cosine and sine coefficients

$$a_m = \frac{2}{\tau} \int_0^\tau y(t) \cos m\varpi_0 t \, dt = \frac{2}{\tau} \int_{-\tau/2}^{\tau/2} y(t) \cos m\varpi_0 t \, dt$$

$$d_m = \frac{2}{\tau} \int_0^\tau y(t) \sin m\varpi_0 t \, dt = \frac{2}{\tau} \int_{-\tau/2}^{\tau/2} y(t) \sin m\varpi_0 t \, dt$$

Equation 23

and $\varpi_0 = 2\pi/\tau$ radians while τ is the total signal time span. The $2/\tau$ constant in Equation 23 serves to normalize the integrals in terms of τ.

Consider a monotone signal with a harmonic frequency $m\varpi_0$ and arbitrary phase angle ϕ:

$$y(t) = \cos(m\varpi_0 t + \phi)$$

Evaluating Equation 23 at $m\varpi_0$, the coefficients reduce to:

$$a_m = \cos\phi$$
$$d_m = -\sin\phi$$

When NHFA is considered, the signal under investigation is also described in terms of cosine and sine coefficients. At an arbitrary frequency ϖ, the signal under examination is then approximated in terms of n as shown by Hirata (2005):

$$G(n,\varpi) = a(\omega) \times C(n,\varpi) + d(\varpi) \times S(n,\varpi)$$

with the respective cosine and sine coefficients

$$a(\varpi) = \sum_{n=0}^{N} y(n) \times C(n,\varpi) \bigg/ \sum_{n=0}^{N} C(n,\varpi)^2$$
$$d(\varpi) = \sum_{n=0}^{N} y(n) \times S(n,\varpi) \bigg/ \sum_{n=0}^{N} S(n,\varpi)^2$$

and

$$C(n,\varpi) = \cos\left[(n - N/2)\varpi/f_s\right]$$
$$S(n,\varpi) = \sin\left[(n - N/2)\varpi/f_s\right]$$

Since $n = 0,1,...,N$ corresponds to the time signal data sequence, Hirata (2005) effectively considers the signal over a time span of $t = -\tau/2,...,\tau/2$.

To gain insight into the NHFA technique, it is useful to consider Equation 27 analytically (Oberholster and Heyns, 2008):

$$a(\varpi) = \int_{-\tau/2}^{\tau/2} y(t)\cos(\varpi\, t)dt \left/ \int_{-\tau/2}^{\tau/2} \cos^2(\varpi\, t)\, dt \right.$$

$$d(\varpi) = \int_{-\tau/2}^{\tau/2} y(t)\sin(\varpi\, t)dt \left/ \int_{-\tau/2}^{\tau/2} \sin^2(\varpi\, t)\, dt \right.$$

Equation 29

When the nominators of Equation 29 are evaluated for a monotone signal $y(t) = \cos(\varpi t + \phi)$:

$$a(\varpi)_{NOM} = \int_{-\tau/2}^{\tau/2} y(t)\cos(\varpi\, t)dt = \cos\phi\left[\frac{\varpi\tau + \sin\varpi\tau}{2\varpi}\right]$$

$$d(\varpi)_{NOM} = \int_{-\tau/2}^{\tau/2} y(t)\sin(\varpi\, t)dt = -\sin\phi\left[\frac{\varpi\tau - \sin\varpi\tau}{2\varpi}\right]$$

Equation 30

The evaluation of the denominators yield:

$$a(\varpi)_{DEN} = \int_{-\tau/2}^{\tau/2} \cos^2(\varpi\, t)\, dt = \frac{\varpi\tau + \sin\varpi\tau}{2\varpi}$$

$$d(\varpi)_{DEN} = \int_{-\tau/2}^{\tau/2} \sin^2(\varpi\, t)\, dt = \frac{\varpi\tau - \sin\varpi\tau}{2\varpi}$$

Equation 31

and thus

$$a(\varpi) = a(\varpi)_{NOM} / a(\varpi)_{DEN} = \cos\phi$$

$$d(\varpi) = d(\varpi)_{NOM} / d(\varpi)_{DEN} = -\sin\phi$$

Equation 32

which is identical to the result of HFA in Equation 25.

The component phase angle obtained with NHFA Φ is given by:

$$\Phi(\varpi) = \tan^{-1}\left[\frac{-d(\varpi)}{a(\varpi)}\right]$$

Equation 33

3.6.1 Signal shift detection using NHFA

As discussed in Section 3.5, phase angle can be used as a frequency shift indicator when tracked at a fixed reference frequency. To study this application using NHFA, consider a signal with an arbitrary frequency removed $\Delta\varpi$ from a reference frequency ϖ_{ref} and an arbitrary phase angle ϕ:

$$y(t_0) = \cos\left[\left(\varpi_{ref} + \Delta\varpi\right)t_0 + \phi\right]$$

<div align="right">**Equation 34**</div>

with $t_0 = 0, ..., \tau$ as with an actual measured signal.

As the time span used in NHFA is defined as $t = -\tau/2, ..., \tau/2$, Φ yields the phase angle of the component under consideration at the mid-span of the time vector, i.e. at $t = 0$. When a signal is expressed in terms of $t_0 = 0, ..., \tau$, Φ thus gives the component phase angle at $t_0 = \tau/2$. In order to obtain Φ at $t_0 = 0$, two phase angle correction steps are necessary when analytical NHFA is employed.

Firstly to transform the signal from t_0 to t, it is necessary to compensate for the resulting phase lag that is introduced. This phase lag is simply given by half the product of the signal frequency and time span:

$$\phi_{lag} = \left(\varpi_{ref} + \Delta\varpi\right)\tau/2$$

so that

$$y_{t_0 \Rightarrow t}(t) = \cos\left[\left(\varpi_{ref} + \Delta\varpi\right)\cdot t + \phi + \phi_{lag}\right] = \cos\left[\left(\varpi_{ref} + \Delta\varpi\right)\cdot t + \phi + \left(\varpi_{ref} + \Delta\omega\right)\tau/2\right]$$

<div align="right">**Equation 35**</div>

Evaluating Equation 29 for this case:

$$a(\varpi_{ref}) = \left(\frac{2\varpi_{ref}}{\varpi_{ref}\tau + \sin\varpi_{ref}\tau}\right)\left[\frac{\sin(\Delta\varpi\tau/2)}{\Delta\varpi} + \frac{\sin(2\varpi_{ref} + \Delta\varpi)\tau/2}{2\varpi_{ref} + \Delta\varpi}\right]\cos\left[\phi + \left(\varpi_{ref} + \Delta\varpi\right)\tau/2\right]$$

$$d(\varpi_{ref}) = -\left(\frac{2\varpi_{ref}}{\varpi_{ref}\tau - \sin\varpi_{ref}\tau}\right)\left[\frac{\sin(\Delta\varpi\tau/2)}{\Delta\varpi} - \frac{\sin(2\varpi_{ref} + \Delta\varpi)\tau/2}{2\varpi_{ref} + \Delta\varpi}\right]\sin\left[\phi + \left(\varpi_{ref} + \Delta\varpi\right)\tau/2\right]$$

<div align="right">**Equation 36**</div>

and

$$\Phi_{\varpi_{ref}} = \tan^{-1}\frac{-d(\varpi_{ref})}{a(\varpi_{ref})}$$

Equation 37

Secondly, $\Phi_{\varpi_{ref}}$ also needs to be adjusted:

$$\Phi_{\varpi_{ref},t_0} = \Phi_{\varpi_{ref}} - \varpi_{ref}\,\tau/2$$

Equation 38

Only the second correction step is required when NHFA is employed numerically.

From Equation 36 and Equation 37, it is observed that $\Phi_{\varpi_{ref}}$ (and thus Φ_{ϖ_{ref},t_0} as well) is influenced by both frequency and phase shifts in the signal. It is thus indeed possible to detect vibration changes in a signal by monitoring $\Phi_{\varpi_{ref}}$.

3.6.2 Sensitivity analysis

To determine the sensitivity of Φ_{ϖ_{ref},t_0} to phase and frequency shifts in a signal, a sensitivity analysis was performed.

Firstly, phase angle shift is considered in a monotone signal while the signal's frequency is kept constant. Figure 36(a) shows the results for both analytic and numeric NHFA for a phase angle shift from -180° to 180° in a 10.1 Hz sinusoidal signal with $\tau = 1$ s. Figure 36(b) provides the phase angle error of the analytic and numeric approach relative to the actual signal phase angle, showing both formulations to be accurate.

Figure 37 to Figure 39 present results for various cases. In these three figures, the (a) subplots depict the numerical formulation results. The (b) subplots show the difference of the analytical formulation phase angles from those of the numerical formulation, thereby evaluating the validity of the analytical formulation at each of these cases.

When only frequency shift is considered (i.e. the signal phase angle is kept constant), Figure 37 is obtained for two ϖ_{ref}s at 10 Hz and 10.25 Hz respectively, with the actual signal frequency ranging from 6.5 Hz to 13.5 Hz. The horizontal axes express $\Delta\varpi$ in terms of ϖ_0, which for the analyzed signal is 1 Hz. Figure 37(a) shows that the relationship between Φ_{ϖ_{ref},t_0} and $\Delta\varpi$ is approximately linear for sections in bands of integer values for $\Delta\varpi/\varpi_0$. In fact for $-\varpi_0 < \Delta\varpi < \varpi_0$, Φ is approximately $\pi \cdot \Delta\varpi/\varpi_0$. When $\Delta\varpi = m\varpi_0$, 180° phase angle jumps are visible and upon further investigation it is observed that both the sine and cosine coefficients either approach

or cross zero in this vicinity. Also, it is shown that when ϖ_{ref} is not an integer multiple of ϖ_0, the phase angle jumps are not as abrupt.
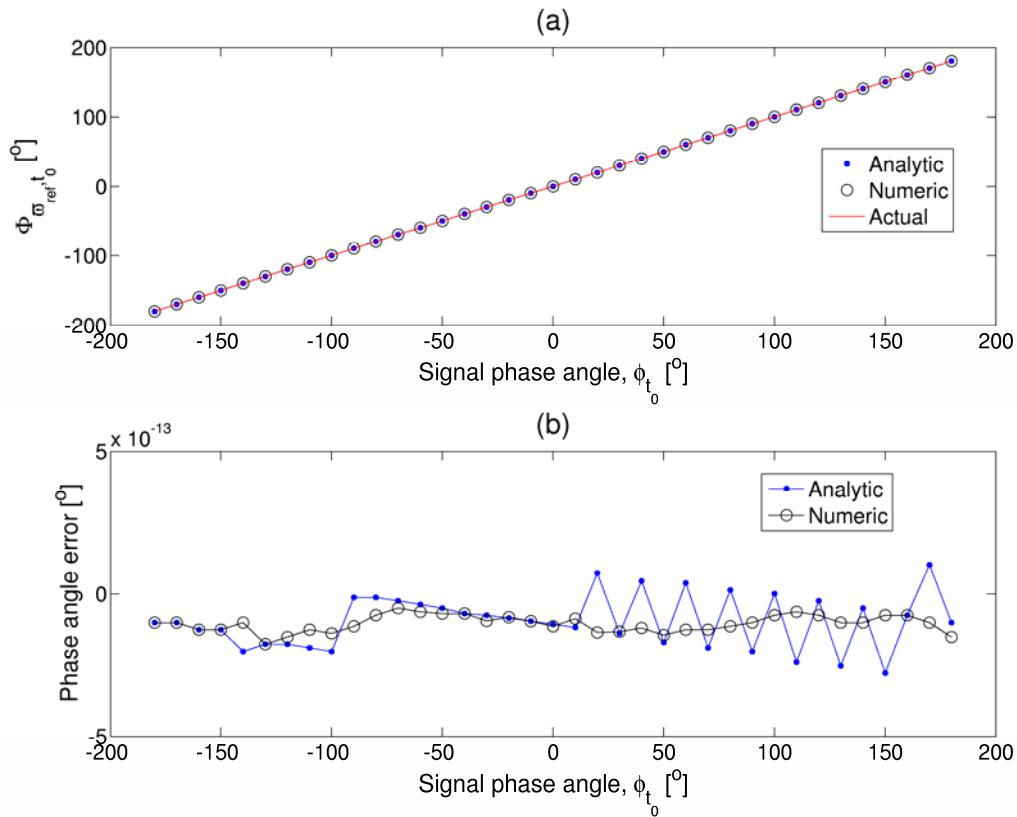

Figure 36: Phase angle shift

In Figure 37(b), the phase angle differences between the analytical and numerical results are shown to increase with frequency offset. Furthermore it is noted that at harmonics of the fundamental frequency, these differences are largely influenced by the reference frequency.

For more extreme values of $\Delta\varpi$, it is clear that Φ loses its linear relationship to $\Delta\varpi/\varpi_0$ as shown in Figure 38(a). In this figure the legend indicates the various signal frequencies that need to be added to the normalized frequency offset factor in order to give the actual signal frequency, e.g. the signal frequency for the 50 Hz curve ranges from 50 Hz to 51 Hz. Noted from Figure 38(b) is that the analytical form of NHFA becomes less and less representative of the numerical form as $\Delta\varpi$ increases.
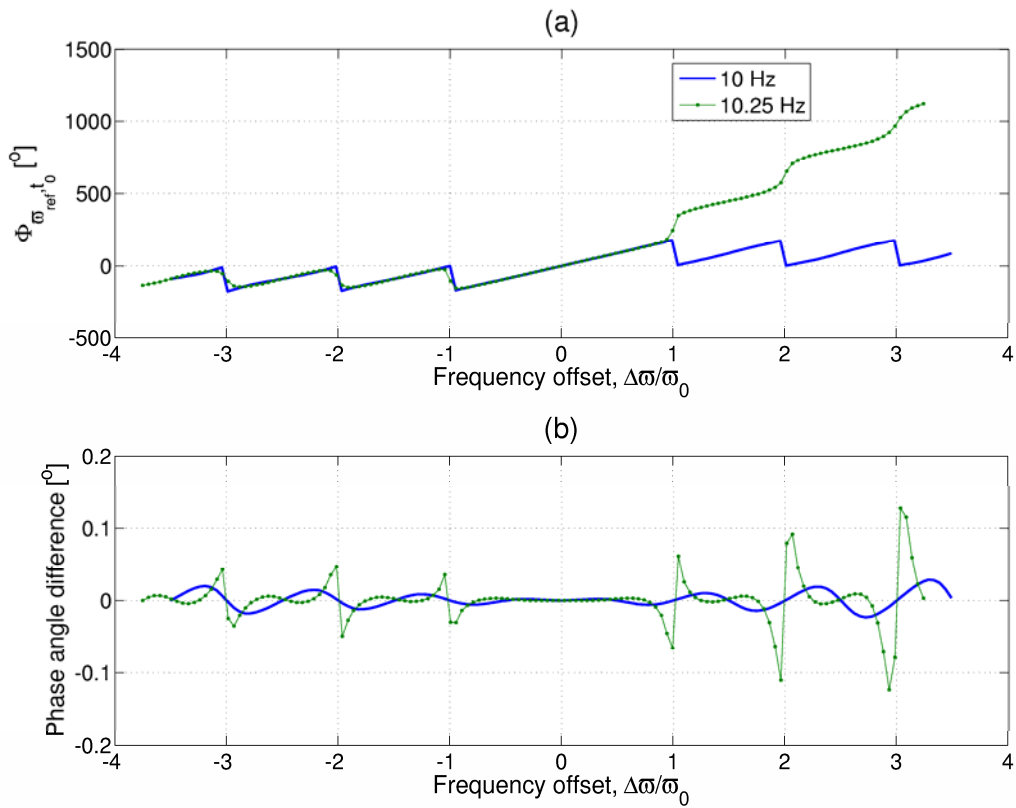
Figure 37: Effect of frequency shift
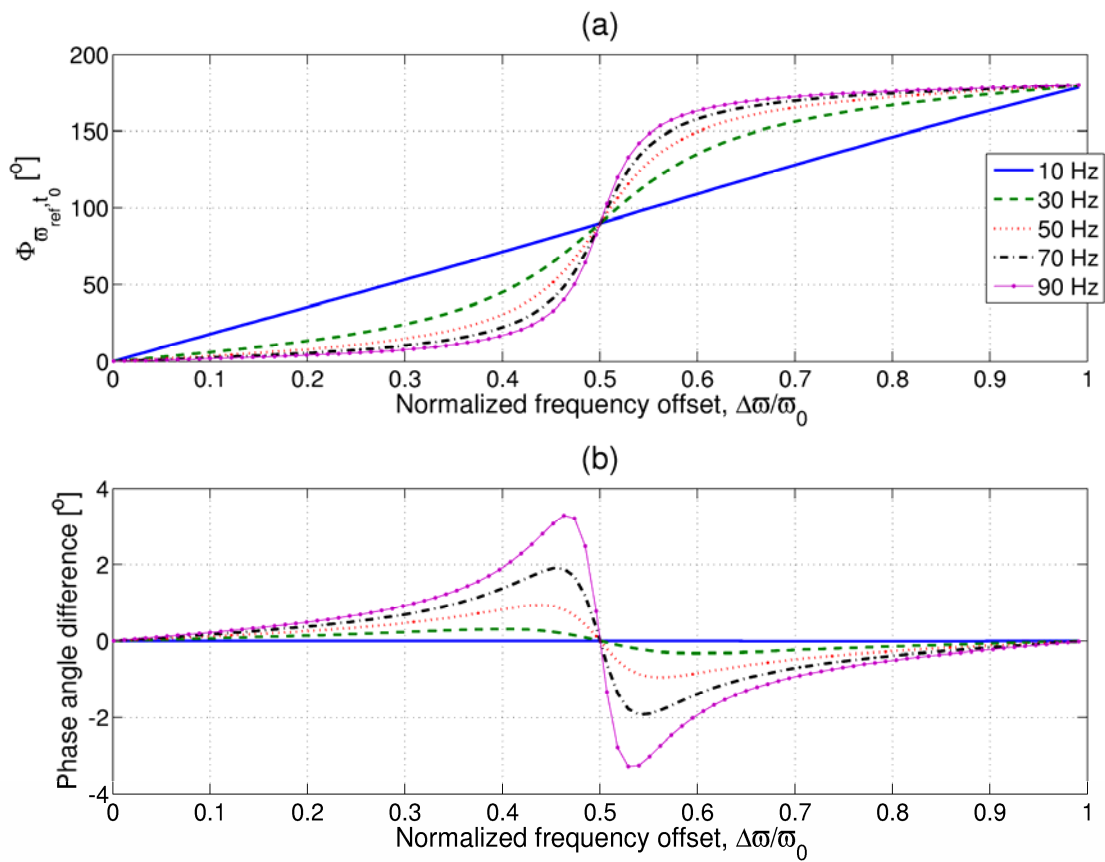
Figure 38: Effect of frequency shift at higher frequency offsets

Figure 39(a) depicts the effect of $\Delta\varpi$ on the accuracy of phase angle detection. As can be noted from this figure, a sign error may occur (although not always) in Φ when $\Delta\varpi = m\varpi_0$. Figure 39(b) shows a more acceptable deviation of the analytical results from the numerical results.

From Figure 37(b), Figure 38(b) and Figure 39(b) the analytical formulation is shown to be representative of the numerical formulation only for low frequency offsets, excluding situations where $\Delta\varpi$ is close to an integer multiple of ϖ_0. The existence of these discrepancies can be ascribed to the different integration techniques used in the numerical and analytical formulations.
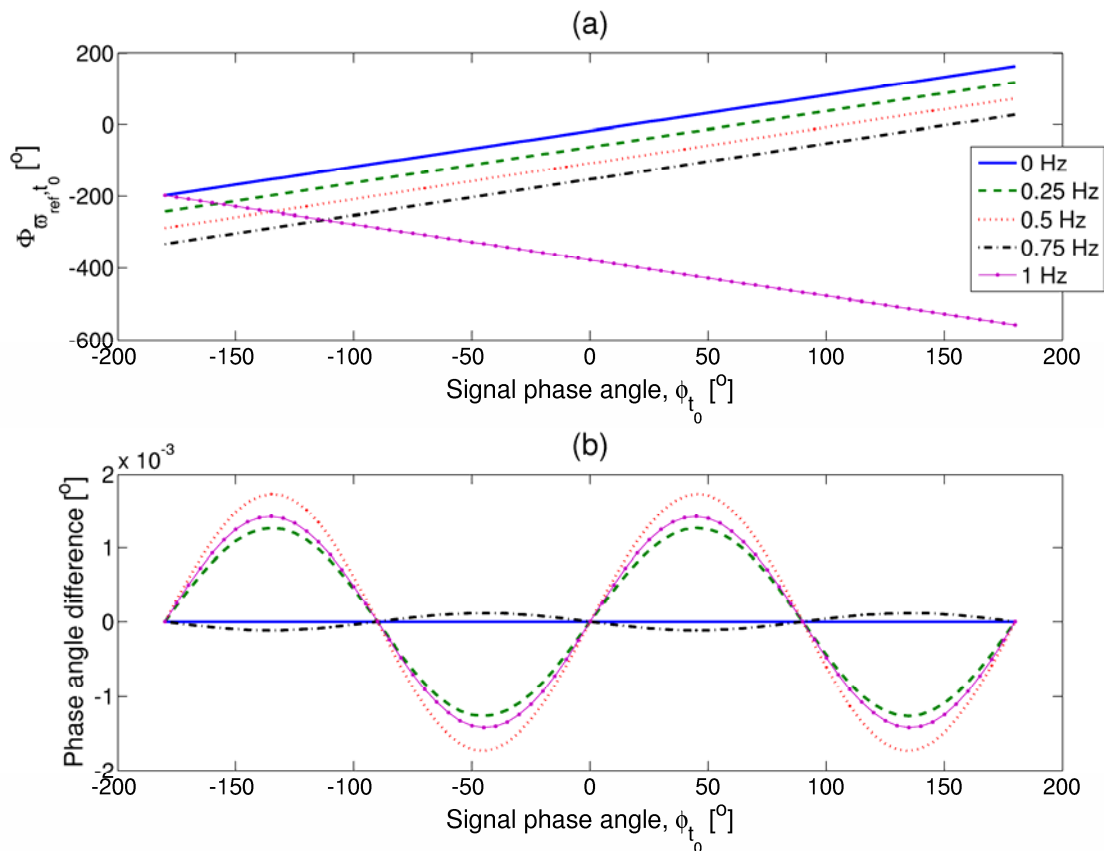
Figure 39: Phase angle detection at different frequency offsets

3.6.3 Damping

Increase in damping of a structure results in simultaneous shifts of frequency and phase. To study this phenomenon, the free vibration responses of a single degree-of-freedom mass-spring system are considered. The undamped natural frequency of the system is 35.6 Hz.

When the structural damping coefficient ζ is varied, the damped natural frequency ω_d and its corresponding phase angle ϕ_d can be calculated for free vibration responses as (Rao, 1995):

$$\omega_d = \omega_j \sqrt{1 - \zeta^2}$$

<div align="right">**Equation 39**</div>

and

$$\phi_d = \tan^{-1}\left(\frac{\zeta}{\sqrt{1 - \zeta^2}}\right)$$

<div align="right">**Equation 40**</div>

Since the introduction of structural damping also results in exponential decay of the time responses, the individual responses were normalized for comparison with results for non-normalized responses in order to study the possible effect of the decay on Φ_{ϖ_{ref}, t_0}.

Figure 40 shows Φ_{ϖ_{ref}, t_0} for a number of scenarios. For normalized responses with $\omega_{ref} = \omega_d$ (i.e. $\Delta\omega = 0$), Φ_{ϖ_{ref}, t_0} correlates with Equation 40 and thus depicts the isolated effect of the phase angle shift. When $\varpi_{ref} = \omega_j$ (i.e. $\Delta\varpi \leq 0$), the true effects of combined phase angle and frequency shifts are observed from the normalized responses. However when the responses are not normalized, it is quite clear that the resulting exponential decays due to damping does effect Φ_{ϖ_{ref}, t_0} for ϖ_{ref} at both ω_d and ω_j. In the latter case the effect is particularly pronounced. From Figure 40 it is seen that exponential decay serves to desensitize Φ_{ϖ_{ref}, t_0} to frequency shift so that it mainly exhibits changes in ϕ_d.

NHFA phase angles are thus clearly affected by structural damping changes which in turn can be influenced by various operational variables such as aerodynamic damping and temperature. It will thus be necessary to keep operational variables in consideration when this condition monitoring approach is followed in an industrial environment.
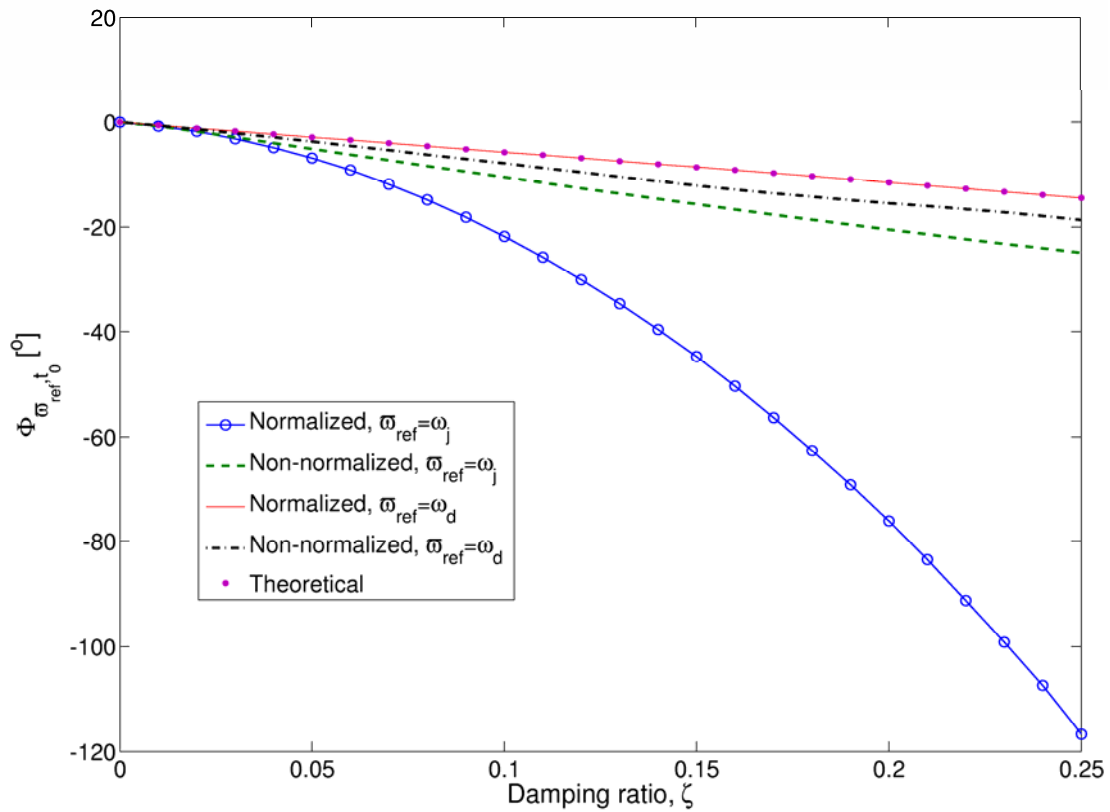
Figure 40: Effect of damping ratio on NHFA phase angle trends

3.7 Results comparison

As an initial approach, the trends of Φ are compared for the simulated ELDV results and the experimental ELDV measurements at frequencies determined from both TLDV spectral peaks and stationary modal analysis, as shown in Figure 41 in terms of Unwrapped Phase Angle (UPA) trends. Different reference frequencies were considered so as to investigate whether it is necessary to perform TLDV measurements on a rotating rotor in order to set up a condition monitoring approach, or whether the results from a simple stationary modal analysis on the rotor will suffice.

Of course, the latter approach is more desirable as it is significantly easier to perform. This does however imply the necessity of consulting FEM results when blade stiffening and/or Coriolis effects have to be taken into account, in order to adjust the stationary modal frequencies for inputs in trend calculations. Since the measurements considered in this thesis are at low rotation speeds, these rotation effects have been discarded. The various frequencies considered in this section are listed in Table 5, the numbering of which corresponds to those of the subplots in Figure 41 to Figure 44.

Table 5: Frequencies used for trend calculations

	FEM frequencies [Hz]	Experimental frequencies [Hz]	
	Nozzle FRF peaks	Spectral peaks	Stationary modal
(a)	124.9	131.8	126.8
(b)	624.6	620.1	628.4
(c)	818.2	844.7	820.2
(d)	1155.5	1171.9	1153.0
(e)	2273.6	2338.9	2279.3
(f)	3535.3	3588.9	3538.2
(g)	4422.2	4550.8	4447.8
(h)	6146.2	6235.4	6140.6
(i)	7495.3	7563.5	7413.1
(j)	9119.3	9238.3	9075.6
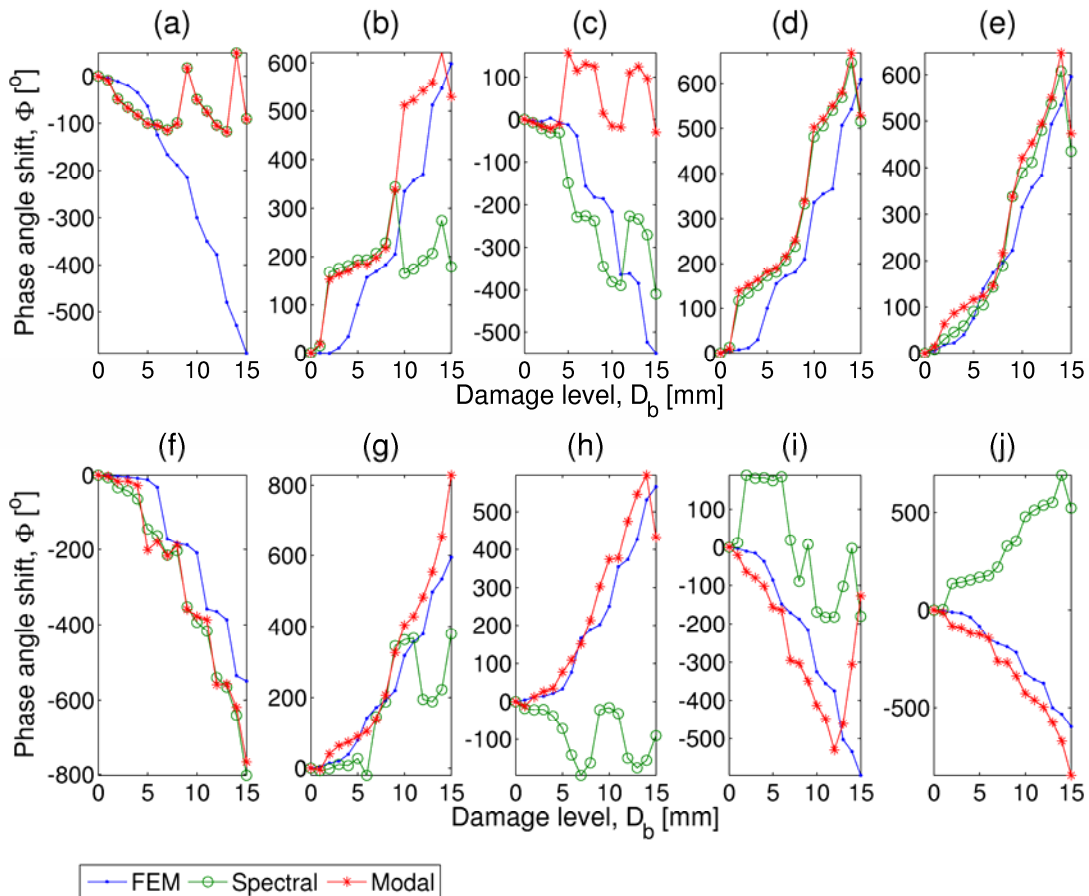
Figure 41: UPA trend comparison

Experimental UPA trend correlations with the FEM results are good at most frequencies as seen in Figure 41 for both spectral and modal reference frequencies. At some frequencies however the correlation is not satisfactory, although some correlation is present. It can be observed particularly in Figure 41(j) that the experimental UPA trend at the relevant spectral reference frequency seems to be the negative of the FEM trend. To investigate this phenomenon, UPA trends were calculated from the FEM using NHFA at the various reference frequencies over a range of ±5% of each frequency. The results are presented in Figure 42 in the form of colour maps indicating Φ corresponding to the provided colour bars. Specifically for the reference frequencies (f) to (j), a number of very distinct and abrupt UPA trend slope sign changes are visible within the specified ranges.

Upon further investigation it was discovered that these discrepancies typically occur at half-harmonics of the fundamental frequency, i.e. when $\varpi_{ref} = m\varpi_0/2$. This phenomenon is indicated on Figure 42. The same is observed for similar calculations on experimental ELDV measurements at the modal reference frequencies (Figure 43).

One approach to overcoming these trend slope sign discontinuities is to calculate the maxima of the absolute UPA trends or the Maximum Absolute Unwrapped Phase Angle Trends (MAUPATs) over the ±5% frequency ranges. In Figure 44, this approach is shown to be successful. With the exception of the first frequency, a good overall correlation is obtained at the various frequencies, showing comparable results at both spectral peak and modal reference frequencies. At the first frequency, some correlation is however still visible up to a damage level of 7 mm.

Furthermore, it is also evident that the results of stationary modal analysis are suitable for obtaining the experimental trends.

A flow diagram of the MAUPAT calculation procedure is given in Figure 45.

3.8 Experimental measurement uncertainty

Experimental measurement uncertainty is an issue that needs to be addressed. It was already discussed in Section 3.2.2 how misalignment effects could affect the TLDV measurements and how filtering was employed to negate its effects. Misalignment will manifest itself in the ELDV measurements as a DC offset proportional to the rotor speed.
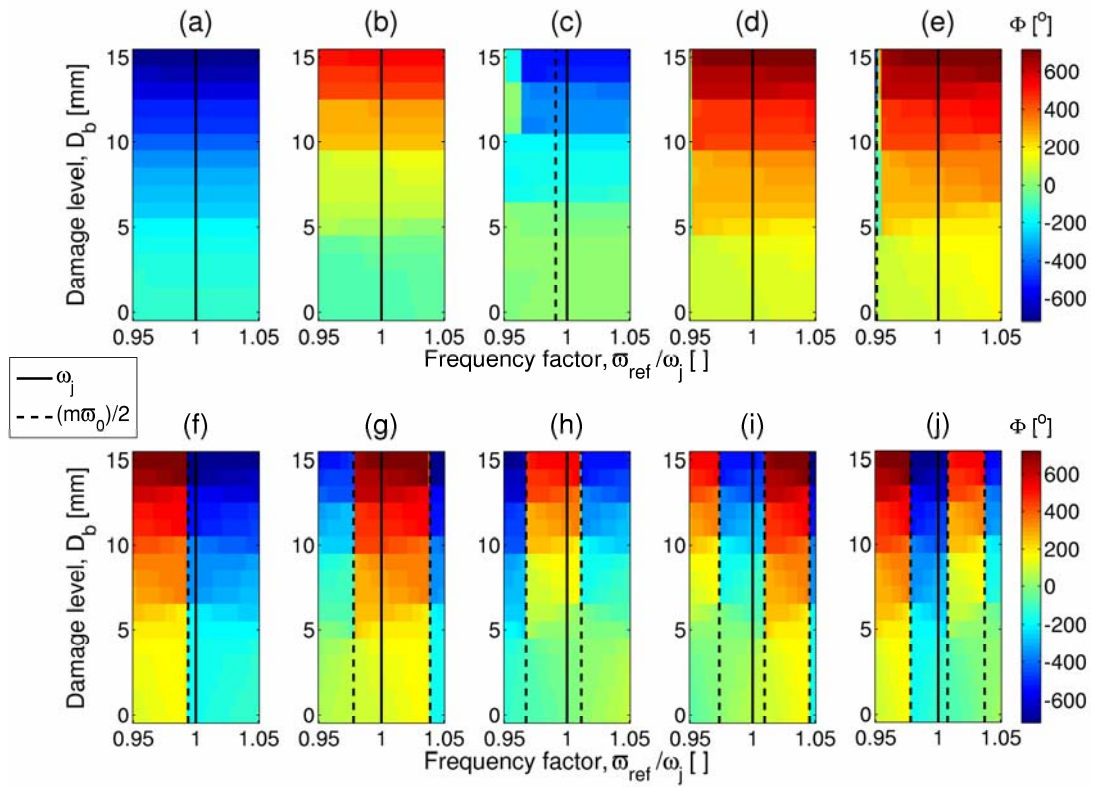
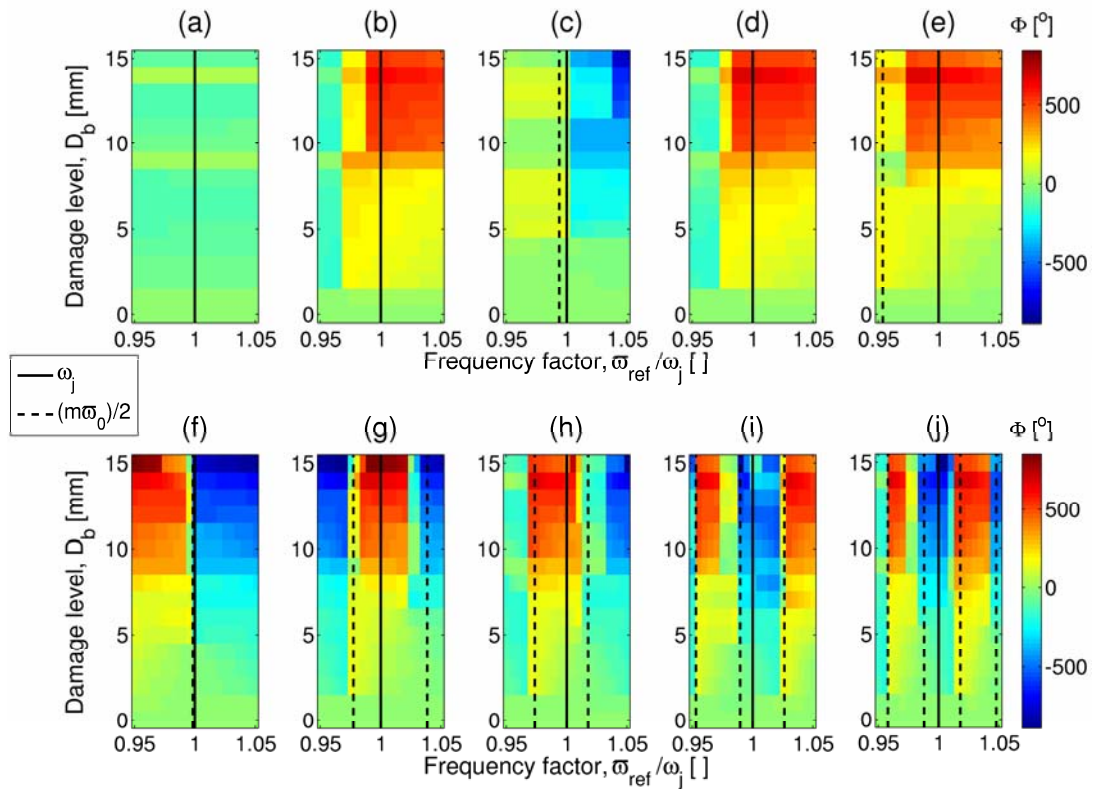**Figure 42: FEM UPA trend sensitivity analysis**

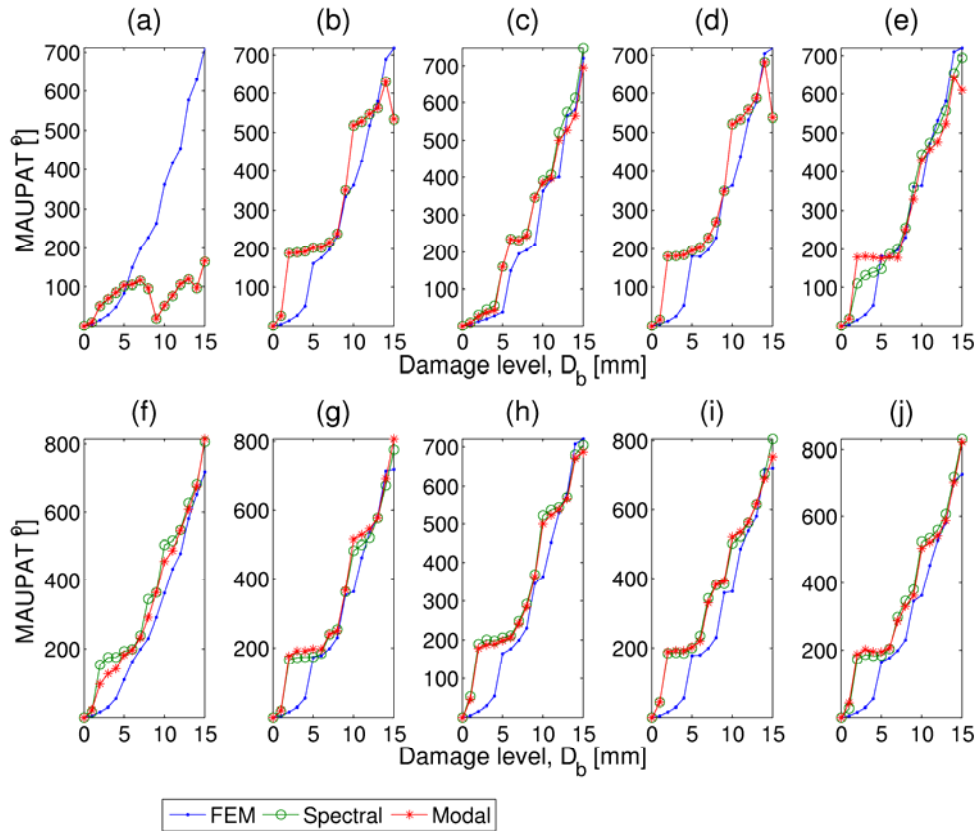**Figure 43: Experimental modal frequency UPA trend sensitivity analysis**

Figure 44: MAUPAT comparison

The major source of uncertainty in the ELDV measurements is speckle noise. It was assumed in this work that the speckle noise pattern remained largely constant for each damage level (Martarelli and Ewins, 2006). In an industrial environment, the speckle pattern of each blade may change over time due to deposit on the blade surface. Thus the isolated effect of speckle noise pattern change on the MAUPAT results needs to be investigated in further work.

The experimental ELDV results presented in Section 3.7 are thus influenced by misalignment effects as well as speckle noise. This may explain the trend incoherence observed between the experimental and FEM trends for the first reference frequency (Figure 44a). The greater majority of the experimental results are however validated by the FEM results.
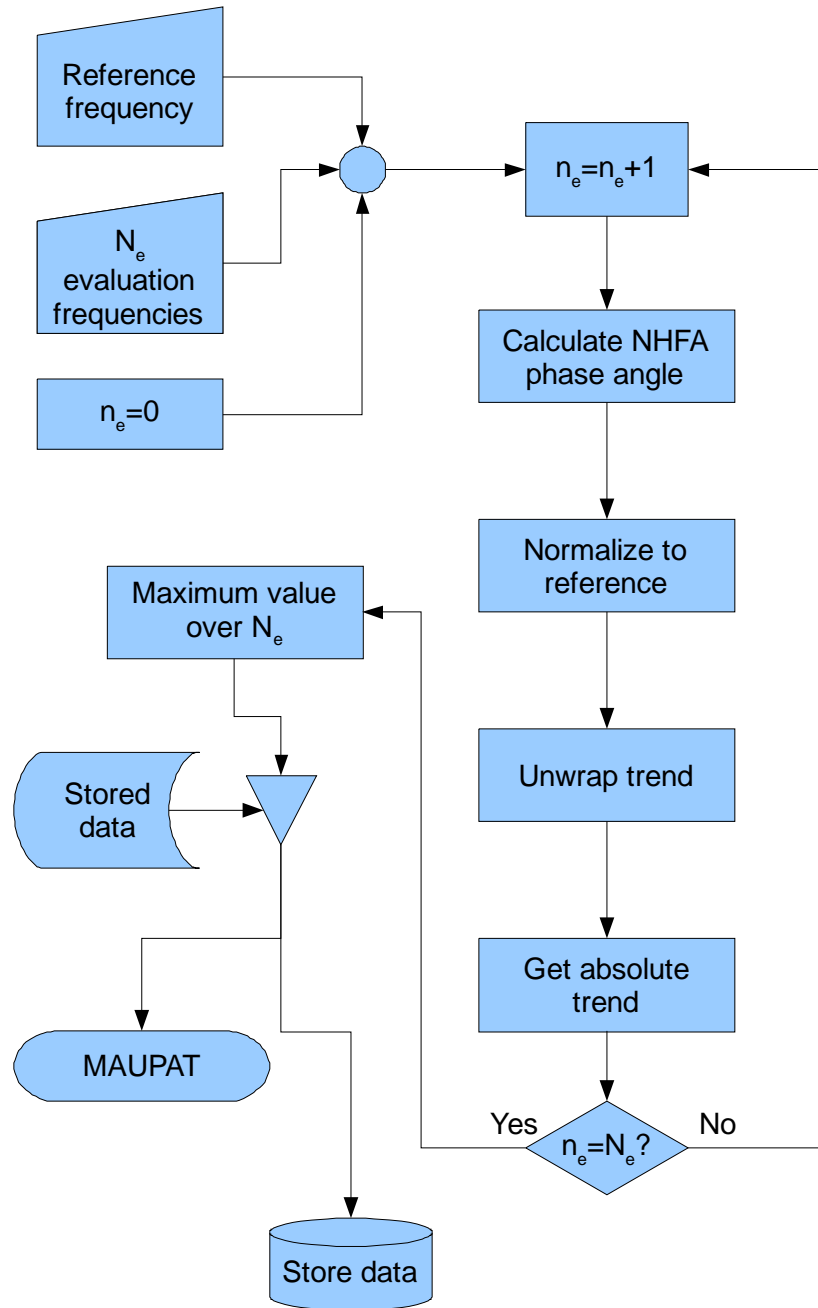
Figure 45: MAUPAT calculation flow diagram

3.9 Conclusions

This chapter serves to present new results for using ELDV on axial-flow rotor blades for the purpose of on-line condition monitoring. Some experimental results were presented for a single-blade test rotor at a rotation speed of 720 RPM. Various signal processing approaches were considered in this chapter and the NHFA technique proposed by Hirata (2005) was studied in detail.

It was shown analytically that the componential NHFA phase angle can be used to indicate signal frequency and phase angle changes when performed at reference frequencies. In a structure such as a rotor blade these changes can be brought on by damage, making NHFA phase angle trends promising as blade health deterioration indicators. With the aid of FEM predictions, this chapter shows that ELDV is a feasible measurement technique for on-line blade vibration monitoring when employing NHFA in this way.

The monitoring approach presented in this chapter should be verified at higher rotation speeds and measurements are necessary on a multi-bladed rotor to investigate whether the monitoring approach can successfully distinguish a damaged blade from amongst healthy blades.

The FEM simulation approach should also be further refined.

The work of this chapter is contained in the article titled *"Online condition monitoring of axial-flow turbomachinery blades using rotor-axial Eulerian laser Doppler vibrometry"* (Oberholster and Heyns, 2009). The results of the NHFA study (section 3.6) are summarized in the conference paper *"A study of the non-harmonic Fourier analysis technique"* (Oberholster and Heyns, 2008).

Chapter 4 Rotor-axial Eulerian laser Doppler vibrometry applied to a five-blade axial-flow test rotor

4.1 Introduction

This chapter extends the work of Chapter 3 to a multi-blade test rotor to verify the ability of the proposed technique to identify damaged blades from among healthy blades. When considering a multi-blade rotor, it becomes necessary to take into account the effects of global blade vibration modes since damage on one blade affects the dynamics of the remaining blades and *vice versa*. As a result, trends may be identified from the undamaged blades which in turn may lead to the erroneous identification of damaged blades. A robust signal processing approach that accurately indicates blade damage is therefore required.

The first section of this chapter focuses on the experimental test setup and testing procedure. The procedure was done in two separate phases to consider damage on a single blade and damage on multiple blades consecutively. The effects on the blade-forcing frequency spectrum by blade-spacing variation due to manufacturing tolerances are studied and it is shown that these effects have to be taken into account during simulations using a FEM.

During experimental testing, high response levels were observed in both TLDV and ELDV measurements at certain damage cases and rotor speeds, similar to those reported in Section 3.3. To investigate this phenomenon, a FEM of the test rotor is constructed and subsequently the Root-Mean-Square (RMS) values of the measurements are shown to be promising blade health indicators.

Results from signal processing on the experimental ELDV measurements at various rotor speeds ranging from 720 RPM to 1440 RPM, are discussed in the next section. It is shown that statistical trend properties of MAUPATs as well as RMS and correlation coefficient trends are useful parameters in identifying damaged blades and monitoring degradation in these blades. In addition, multiple ELDV measurement positions are demonstrated to be advantageous to achieving robust results. After the training of ANNs with these parameters, it is proven that ELDV measurements can be used to accurately identify and quantify blade damage from amongst healthy blades.

Finally, it is verified experimentally that the first natural frequency of the individual blades can be accurately estimated from run-up and run-down ELDV measurements.

4.2 Test setup

The test rotor of Section 3.2 was again employed and installed with five straight, flat blades. The test rotor was driven directly by the speed-controlled motor at speeds of 720, 960, 1200 and 1440 RPM during testing. As previously, a piezoelectric dynamic pressure sensor measured the back-pressure at the nozzle arising from the airflow blockage caused by the blade during rotation. Due to manufacturing tolerances of the blade-clamp interfaces, it was necessary to use epoxy to eliminate gaps between the blade and clamp surfaces prior to clamping. This was found to minimize the variation in the natural frequencies of the blades, arising from differences in the clamping boundary conditions.

Prior to ELDV and TLDV testing, the natural frequencies of the individual rotor blades were obtained from stationary modal testing. Each blade was individually tested using a modal hammer as excitation and the Polytec PSV300 laser vibrometer for response measurements. This choice of excitation and measurement technique minimized any alteration in structural mass, thereby ensuring accurate FRFs. These FRFs were furthermore used for updating the rotor FEM.

As in Chapter 3, damage was simulated in various blades by increasing the depth of a slot cut in the blades' leading edges, close to the blade roots. Testing was conducted in two phases. During the first phase, damage was introduced on blade #1 only, whereas in the second phase, damage was considered on blade #3 and blade #5 simultaneously at different damage-increment rates. The damage cases considered are schematically depicted in Figure 46.

Due to manufacturing tolerances, variation was present in the spacing of the blades in both axial and circumferential directions. This affected the forcing frequency spectrum of the blades and in particular resulted in energy being introduced at higher rotor orders (Ewald et al., 1971). This spectrum can be estimated from the measured pressure pulses as demonstrated by the PSD in Figure 47 for 720 RPM, showing the first 16 harmonics. For this reason, it was important to ensure that the relative timings between pulse peaks used in the FEM correlated with those of the measured pressure pulses.
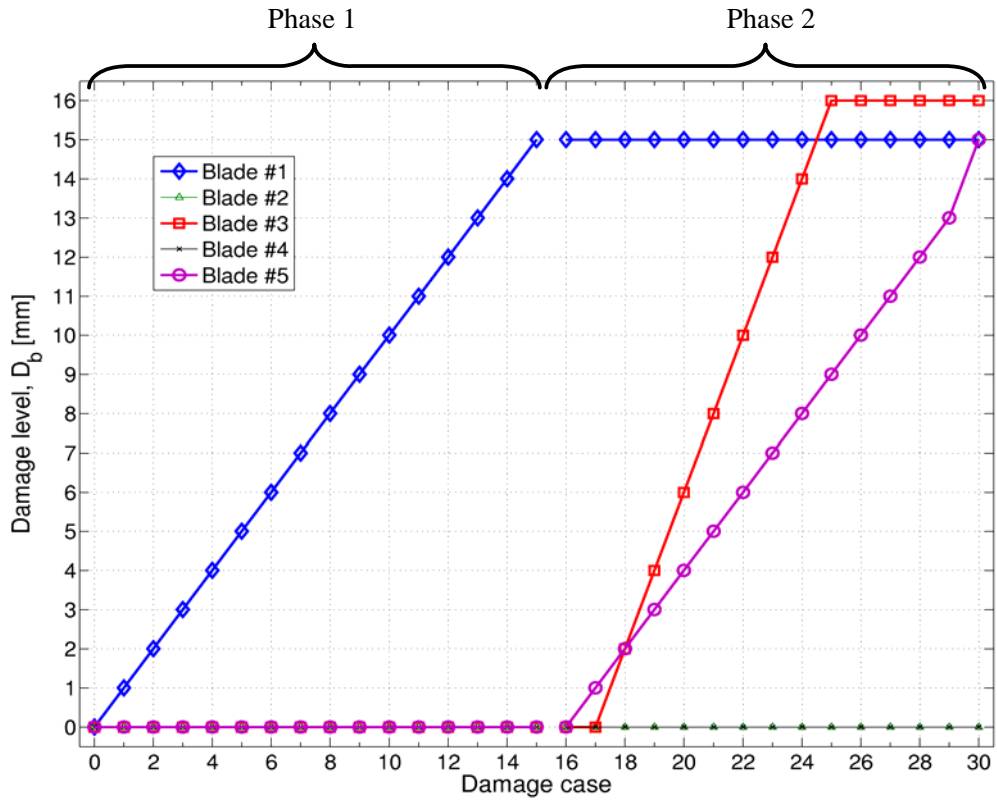
Phase 1   Phase 2

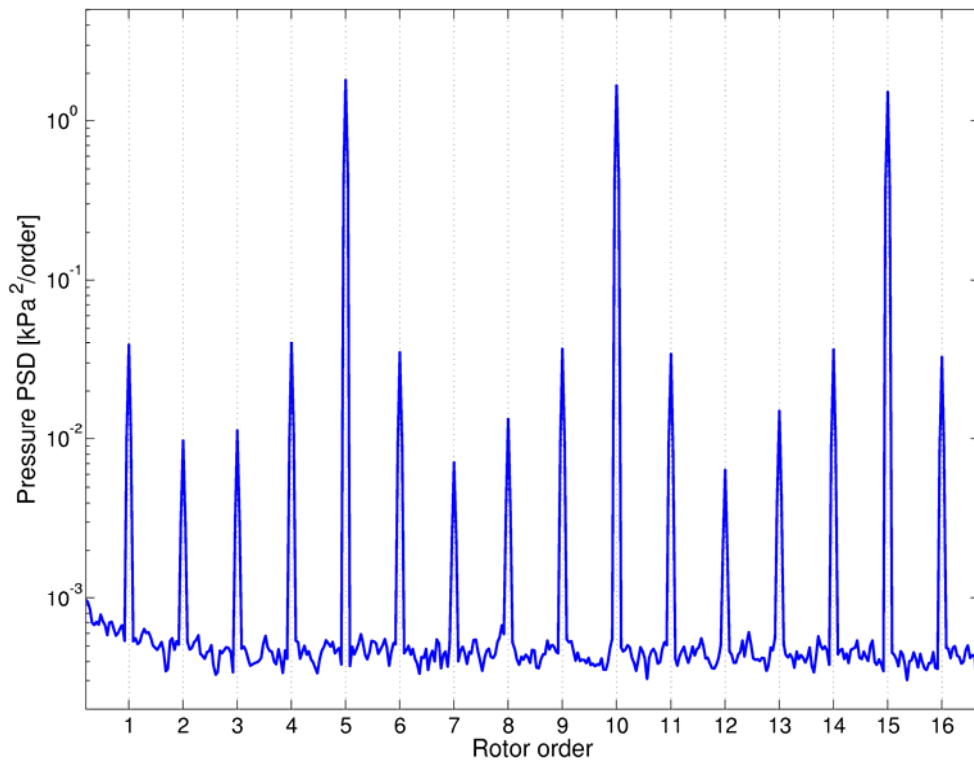**Figure 46: Damage cases considered during testing**

Figure 47: Pressure pulse harmonics

4.3 Test control and measurement

During ELDV and TLDV testing, data acquisition and vibrometer mirror control were again accomplished with LabView, using a National Instruments PCI-6110 card. The shaft encoder signal of 5000 PPR was used as a clock signal to perform position-based sampling, thus simplifying data post-processing. A schematic layout of the LabView algorithm used is given in Figure 48.
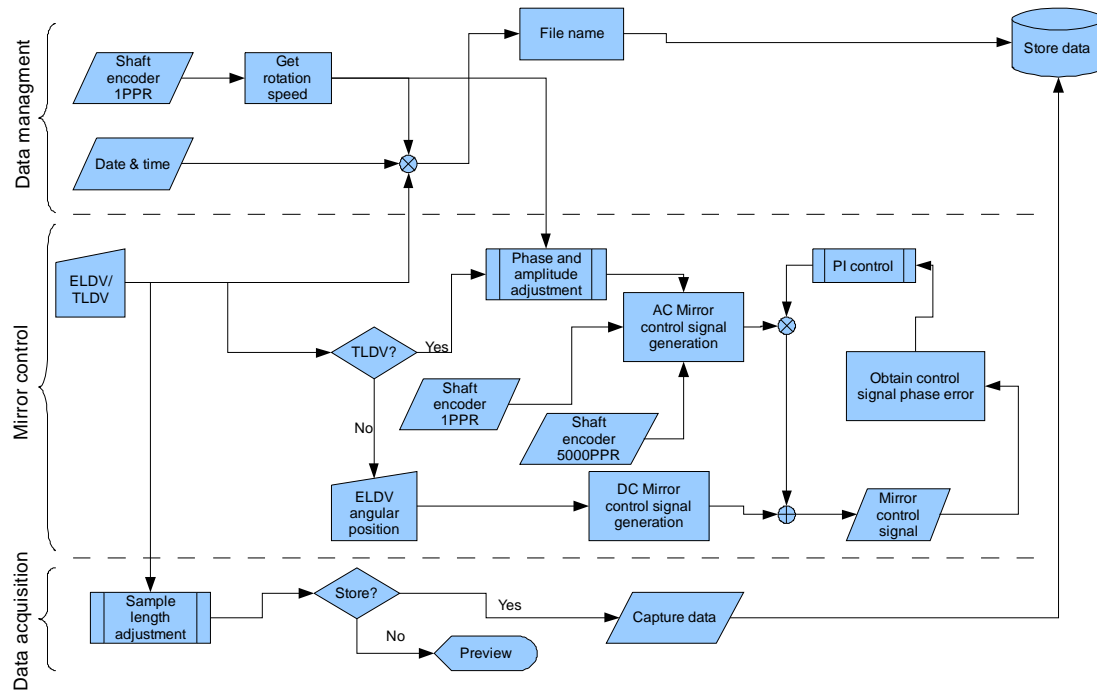
Figure 48: Schematic layout of LabView VI file for control and acquisition

TLDV measurements on the test rotor were available over nearly 180° as seen in Figure 49. Since triggering is only available in edge-detection mode for this particular National Instruments card, any spurious peaks of amplitudes as low as 0.2 V in the shaft encoder signal caused erroneous clock pulse incrementation. It was therefore necessary to incorporate a Proportional-Integral (PI) control loop in the LabView algorithm used. Figure 50 compares the control signal phase error with and without implementation of the PI control loop at a rotation speed of 600 RPM. The initial 12.6^o phase angle errors that are visible from this figure result from the dynamic phase lag of the mirror-servo system.
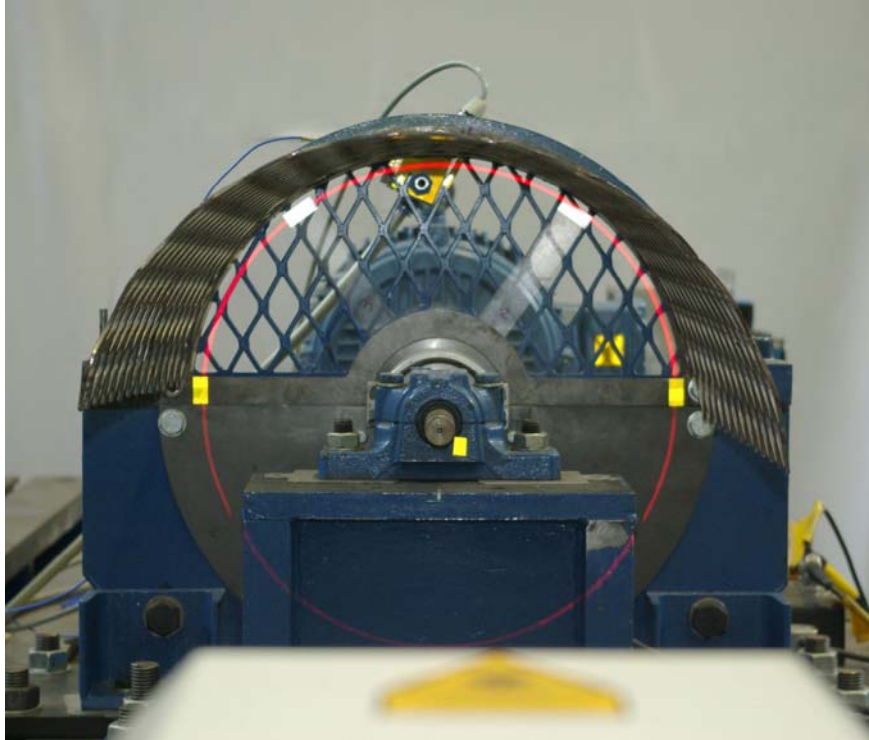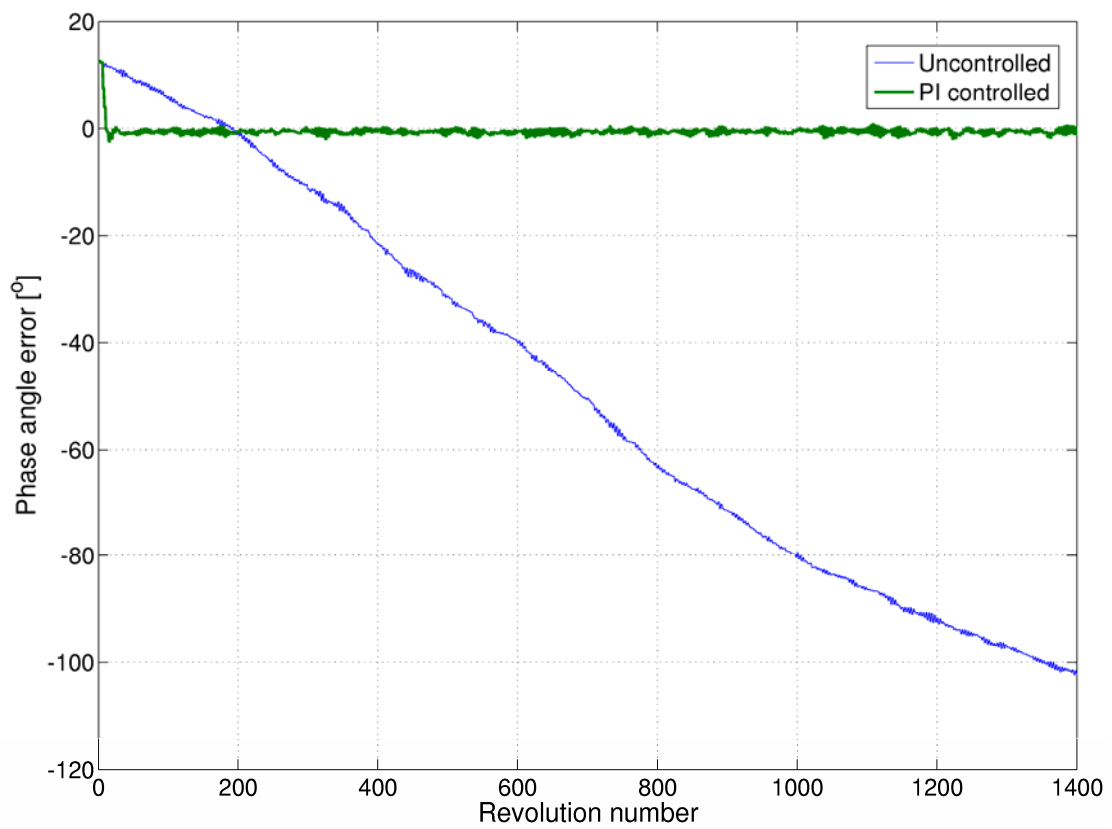
Figure 49: TLDV implementation

Figure 50: TLDV PI control

Two measurement positions, namely A and B, were considered during ELDV testing (see Figure 51(a) and Figure 51(b) respectively). At position A, the ELDV forced-vibration signature is available as the blade passes in front of the nozzle (i.e. at position A, the air impinges on the blade for the duration of each individual ELDV measurement). Just after passing the nozzle, the free vibration ELDV signature is available at position B (i.e. no impingement by the air-jet.) The purpose of considering these two positions was firstly to determine the sensitivity of the proposed data analysis approach to measurement position. Secondly, it was used to investigate possible advantages of using multiple ELDV measurement positions for on-line condition monitoring.
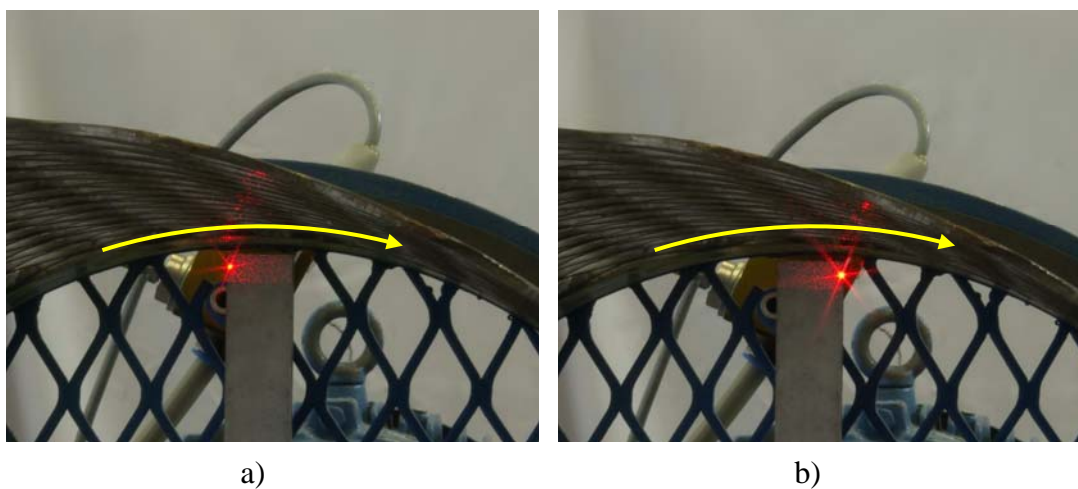

a)   b)

Figure 51: (a) ELDV position A; (b) ELDV position B

As in chapter 3, the SLDV was set to measure at a 125 mm/s/V sensitivity with the tracking filter option disabled. As mentioned earlier in section 4.3, position based sampling was performed using the shaft encoder 5000 PPR signal, resulting in the minimum sampling frequency used during testing being about 60 kHz. For this reason, the 20 kHz low-pass filter option was selected on the SLDV controller.

4.4 FEM

A FEM of the test rotor was constructed as shown in Figure 52. The blades were modelled with shell elements while the hub and shaft were modelled with solid and beam elements respectively. Beam-solid and shell-solid element coupling was accomplished with Multi-Point Constraint (MPC) elements. Damage was again simulated in the model by deleting appropriate elements in the blades.
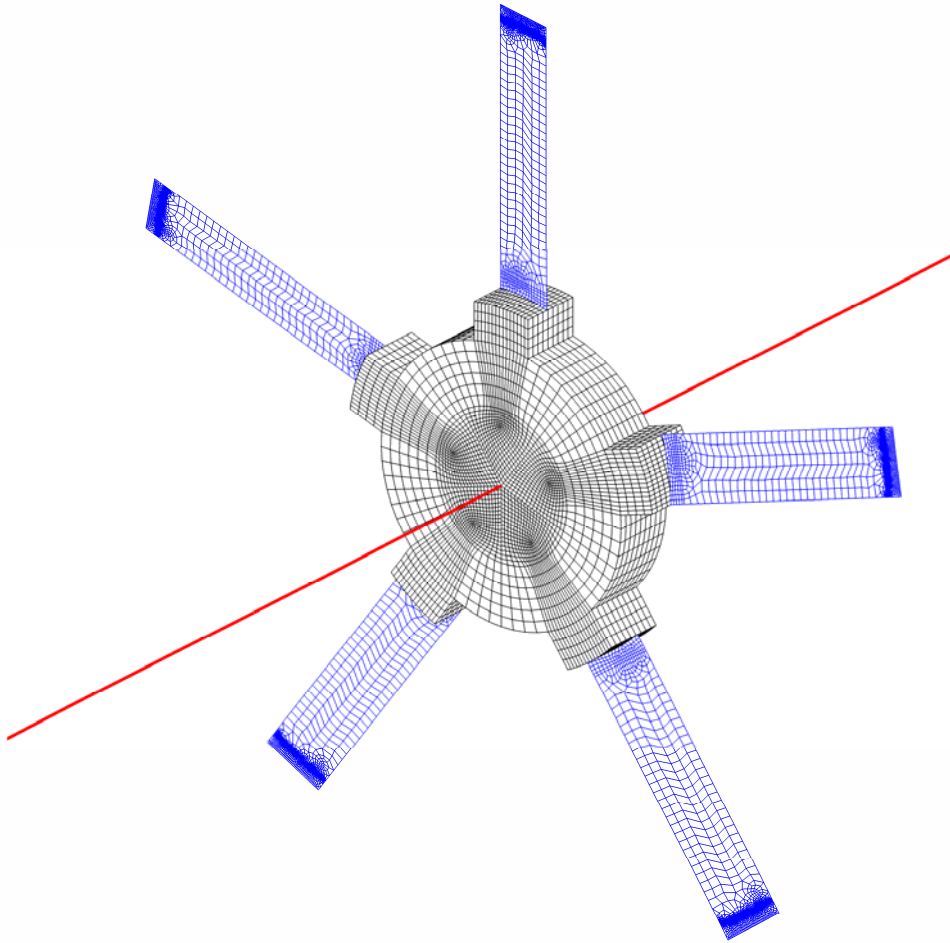
Figure 52: Finite element model

The pulses exerted on each blade by the air-jet nozzle during rotation were approximated with a concentrated force on each blade. It was assumed that these forces were directly proportional to the respective pressure signals measured. For each blade number b, a normalized force F_b was approximated from the corresponding average pressure pulse waveform P_b:

$$F_b = \mu_b P_b$$

Equation 41

where μ_b normalizes each P_b with respect to P_1:

$$\mu_b = \frac{\max(P_b)}{\max(P_1)}$$

Equation 42

4.4.1 Model updating

Model updating of the FEM was conducted based on differences between FEM and experimental FRFs (Chapter 3). Optimization was performed with four sets of material properties consisting of the Young's modulus, Poisson ratio and density for each set. The four material property sets accommodated the optimization of the material properties of the rotor hub, the individual blade clamp interfaces, the shaft and the blades. The same material properties were used for all the blades while the individual blade thicknesses served as five additional optimization variables. Optimization was performed with the utilization of the Dynamic-Q Optimization Toolbox (Hay, 2002). FEM FRFs were calculated from Nastran eigenvalue analysis results (including residuals) in Matlab using modal decomposition (Pruemont, 2002:21). Following the updating of the FEM material properties, the modal damping parameters were updated in a similar way. The FRFs of the updated FEM are compared with the experimental FRFs in Figure 53, showing very good correlation.
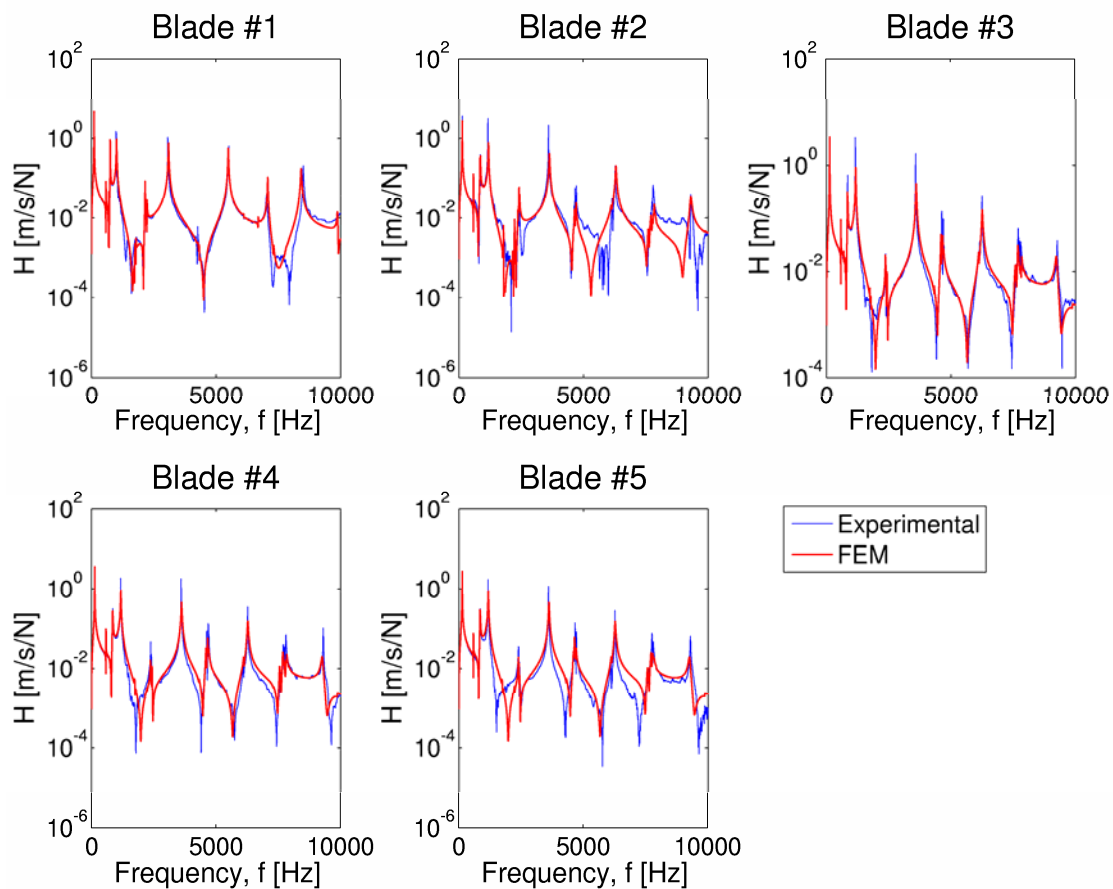

Figure 53: Updated FEM FRFs

4.4.2 TLDV simulation

TLDV was simulated in the FEM by applying F_b (Equation 41) in succession so that the peak occurrences of each F_b corresponded with that of the measured P_b signals. This is depicted in terms of rotor angle in Figure 54, with F_b obtained from P_b measured at 720 RPM. It was assumed that the F_b waveforms remained unchanged in the angular domain at the various rotor speeds and damage cases. The significant variation in the peak amplitudes of F_b shows a correlation with the variation in the blade-nozzle standoff distances measured in the test rotor blades.
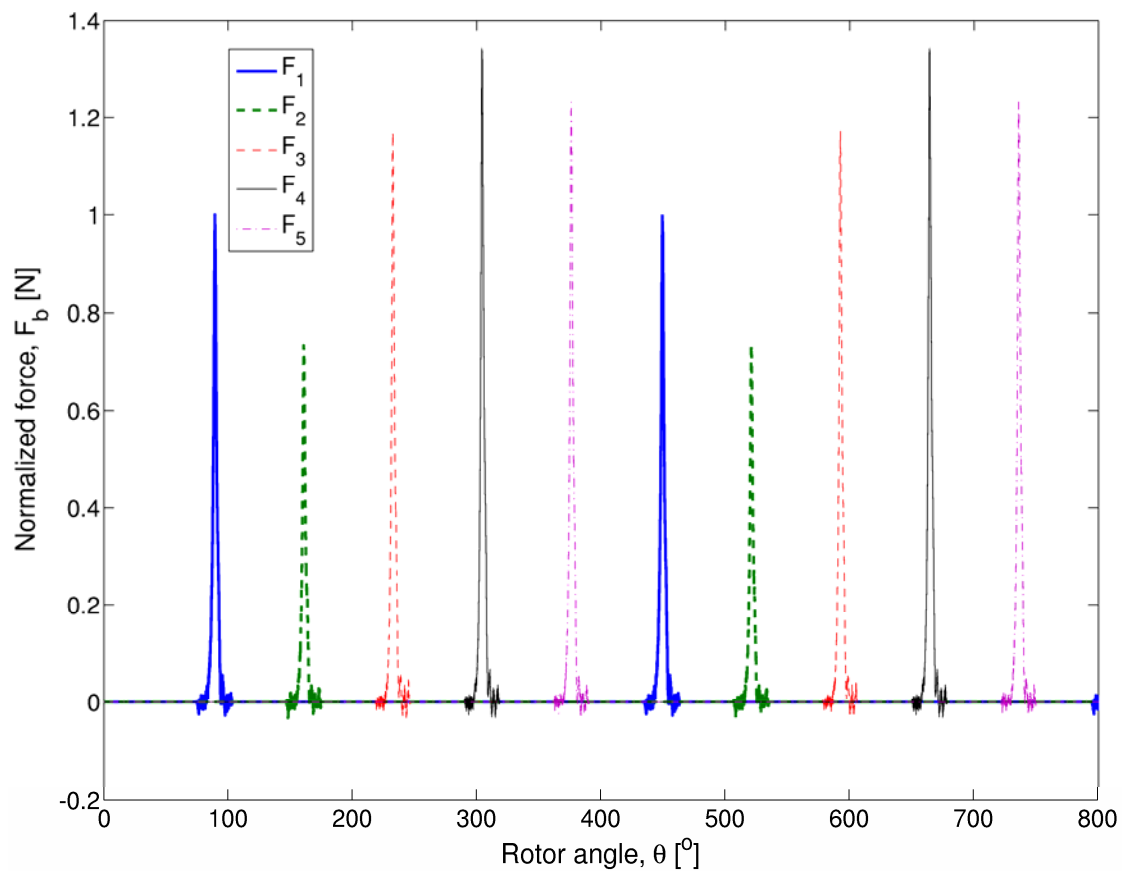

Figure 54: FEM force functions

Using initial conditions of rest, pulses were applied to the FEM over a period corresponding to 14 revolutions to allow for the development of steady-state vibration. TLDV measurements were then simulated using the FEM for the different damage levels and rotor speeds considered during experimental testing. Figure 55 depicts a comparison of the TLDV velocity results (v_L) of numerical simulations for damage cases 0-15 with the experimental measurements for blade #1, showing a close correlation. An additional damage case XVI was considered in the FEM corresponding to a blade #1 damage level of 16.7 mm.
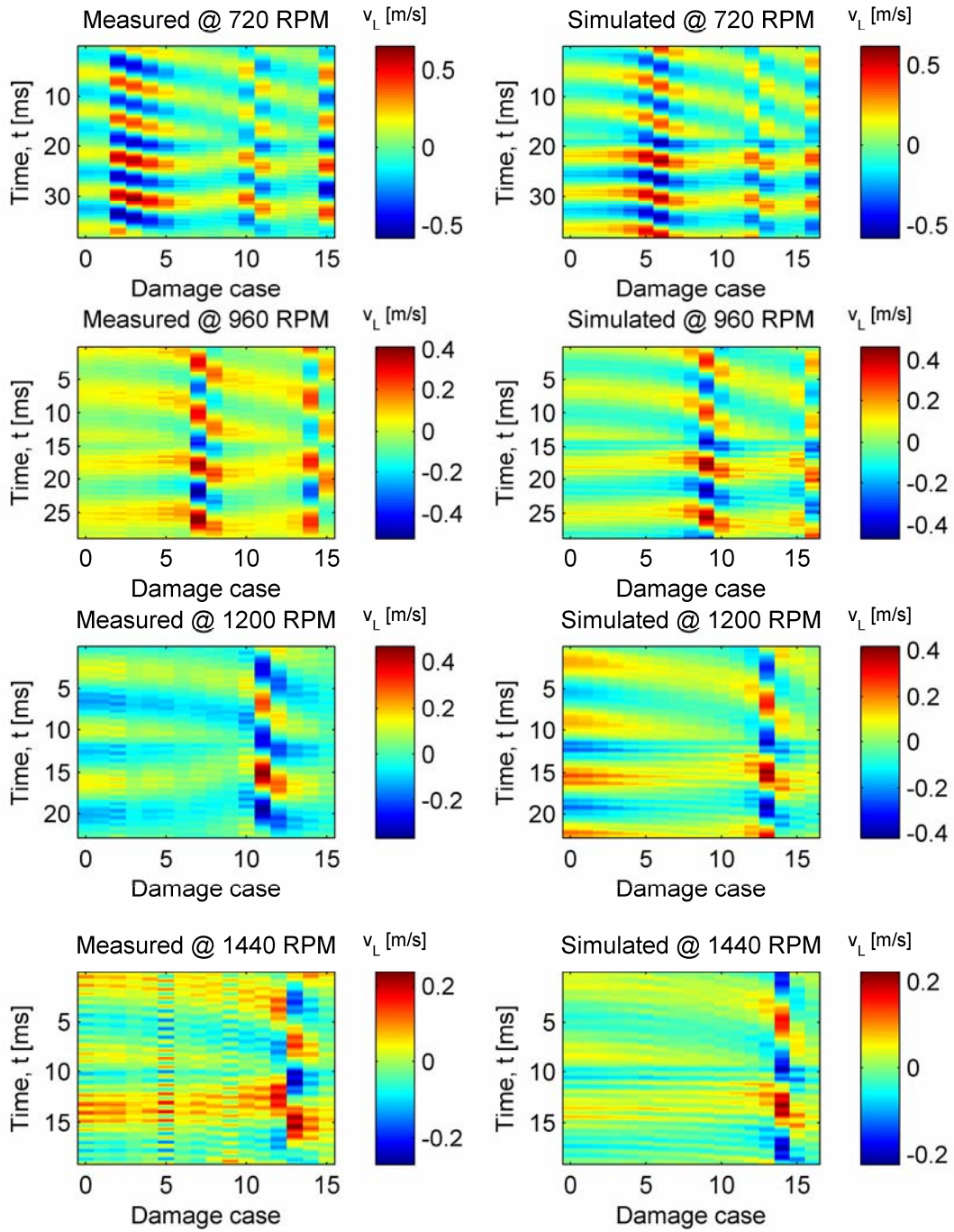
Figure 55: Time response comparison for different damage levels

At various damage cases, high response amplitudes are observed along with large phase angle changes (as can be seen from the distinct discontinuities in velocity pattern at these damage cases), e.g. the measurements for damage cases 7 and 14 at

960 RPM. This correlates with similar observations made in Section 3.3 for a single blade. To study this phenomenon, the change in the FEM first bending-mode natural frequency ω_1 of blade #1 with an increasing damage level is superimposed on various orders of the different rotor speeds in Figure 56. It can be seen from this figure that ω_1 coincides with rotor orders at damage levels in accordance with the discontinuities noted in Figure 55.
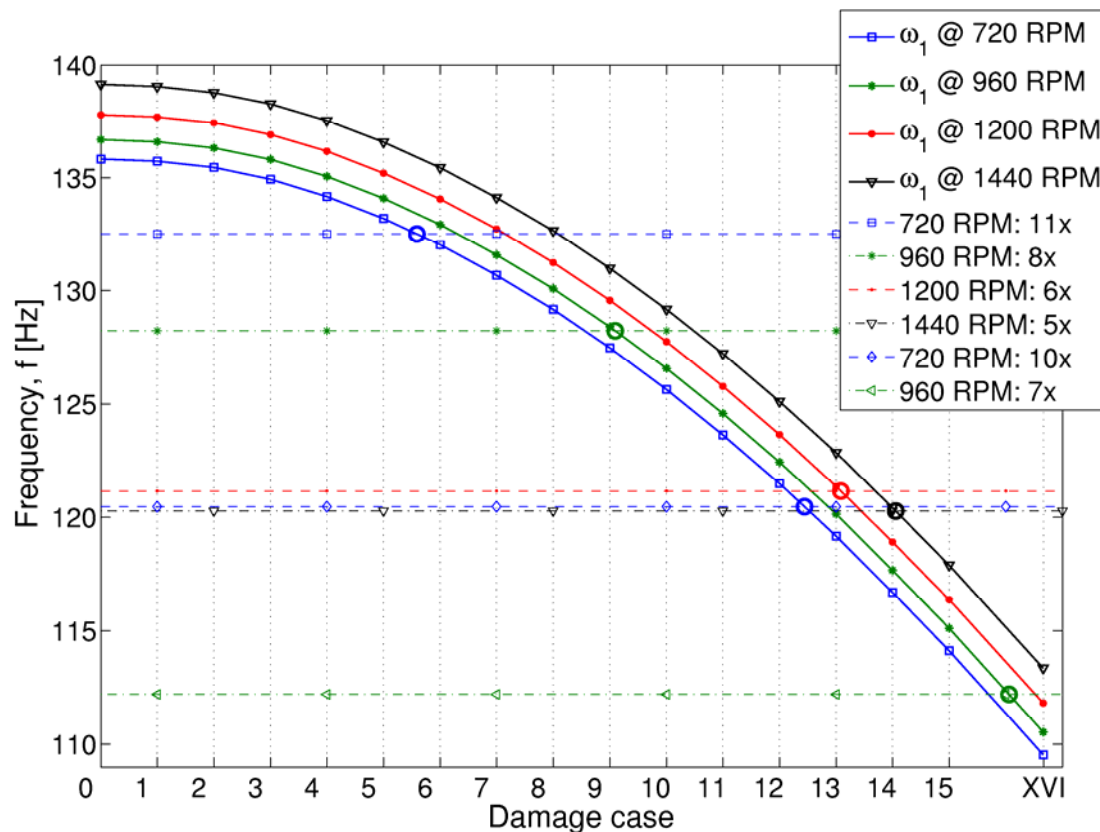

Figure 56: FEM blade #1 ω_1 comparison with rotor orders

Evaluating the velocity RMS values of the simulated results, the coinciding of high velocity response with rotor orders at the relevant damage levels are clearly demonstrated in Figure 57. It is furthermore clear from this figure that RMS holds promise as a parameter for blade condition monitoring: Not only is a systematic change in RMS value indicative of deterioration in blade health, but it can also be seen that if a sign change occurs in the RMS trend slope, ω_1 is close to a rotor order. Thus RMS can serve as an indicator of blade natural frequency shift at a fixed rotor speed on the condition that the blade loading and operational conditions remain constant. This observation also indicates that run-up and run-down ELDV records of the rotor blades along with the rotor speed are valuable for estimating the individual ω_1 values.
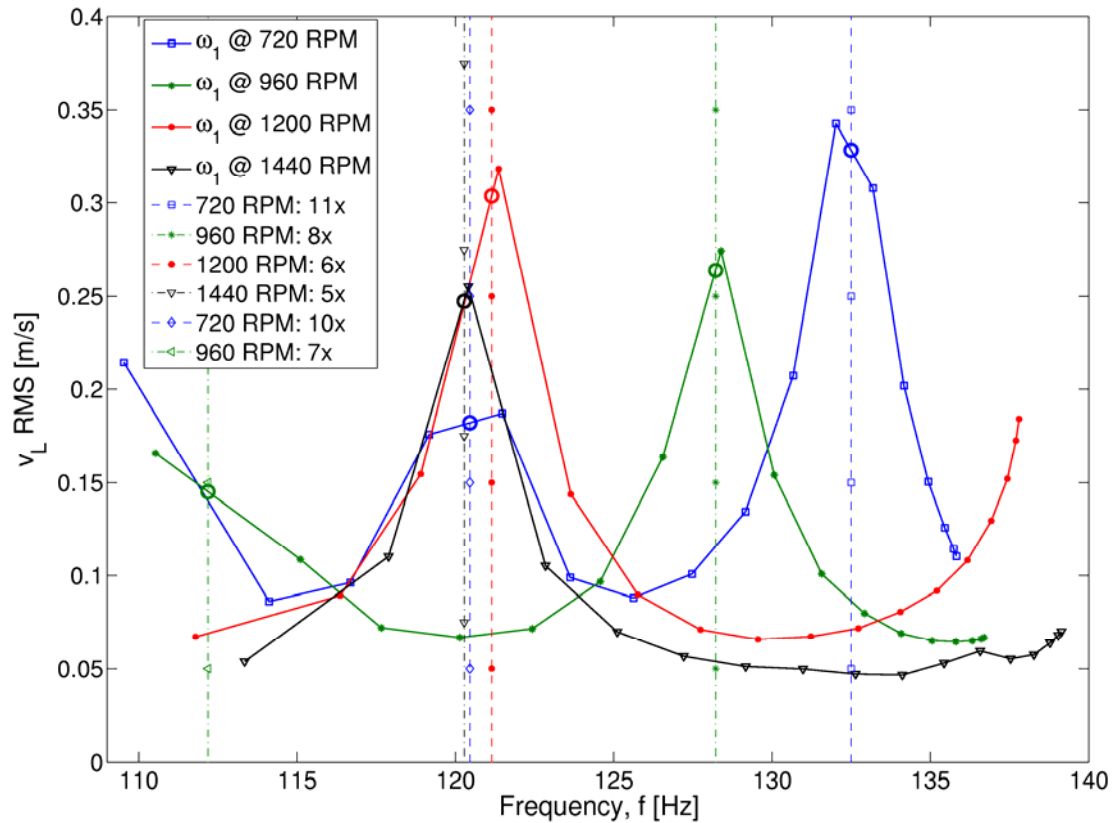
Figure 57: Blade #1 simulated RMS values as functions of FEM blade #1 ω_1

4.5 Experimental results

4.5.1 MAUPAT analysis

In Chapter 3, NHFA was performed on ELDV signals to obtain MAUPATs over ranges within 5% of the individual natural frequencies of the single blade. Due to blade mistuning and the effect of global mode shapes, groupings of mode shapes at various frequencies were present in the multi-blade test rotor. As a result, NHFA was performed in this chapter to obtain MAUPATs over ranges around the average of the blade natural frequency groupings. The individual ranges were determined from the variation around each reference frequency. The reference frequencies considered are listed in Table 6 along with the relevant ranges.

When evaluating the experimental MAUPAT results, it soon became apparent that interpreting the trends is more complicated on a multi-blade rotor than on the single-blade rotor used in Chapter 3. This is demonstrated in Figure 58 for the MAUPATs of damage cases 0-15 around f_1.

Table 6: MAUPAT reference frequencies

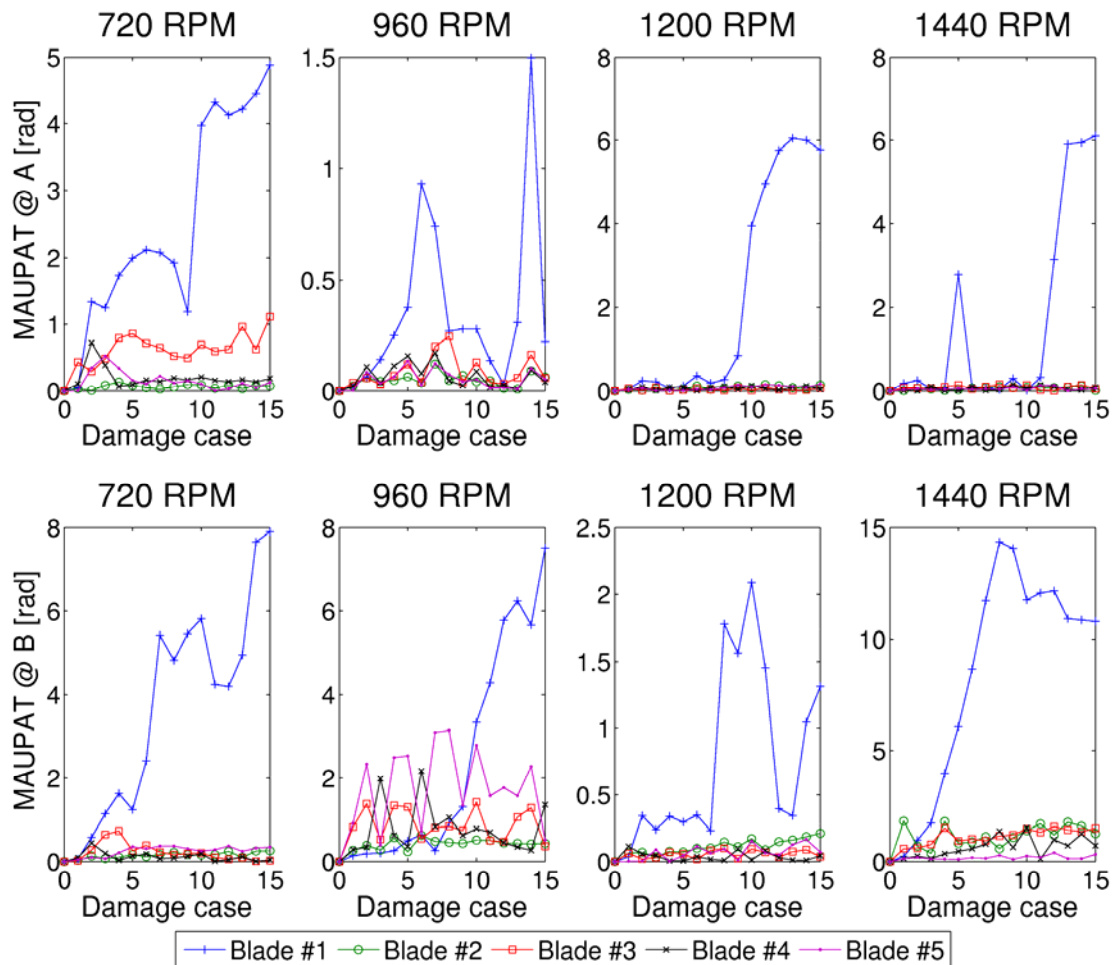| Reference number	Reference frequency, f_{ref} [Hz]	Frequency range [Hz]
1	135	±5
2	600	±50
3	865	±25
4	1167.5	±12.5
5	2390	±50
6	3590	±20
7	4600	±40
8	6260	±30
9	7750	±150
10	9270	±50

Figure 58: Damage cases 0-15 MAUPATs around f_1

This figure shows a number of blade #1 trend jumps, corresponding with the observations from Figure 55 relating to the proximity of blade #1 ω_1 and rotor order. Secondly, it is clear that ELDV measurement position (A or B) has a definite effect on the trends. It also is evident that depending on rotor speed and measurement position, it may prove difficult to identify the damaged blade. This is either due to a lack of a strong and consistent trend in the damaged blade MAUPATs (e.g. position A at 1440 RPM) or large changes in the MAUPATs of some undamaged blades (e.g. position B at 960 RPM). The trends of blade #1 furthermore do not always increase monotonically with damage.

In order to distinguish between damaged and undamaged blades, it was necessary to evaluate the statistical properties of the individual blade trends. After evaluating various statistical parameters, the trend standard deviation (σ) was found to yield the most favourable results. Figure 59 depicts the σ trends of the MAUPATs (σ_{MAUPAT}) around f_1, showing improvement in trend separation in most cases. However, strong trends are still visible in undamaged blades in some cases (e.g. position B at 960 RPM).
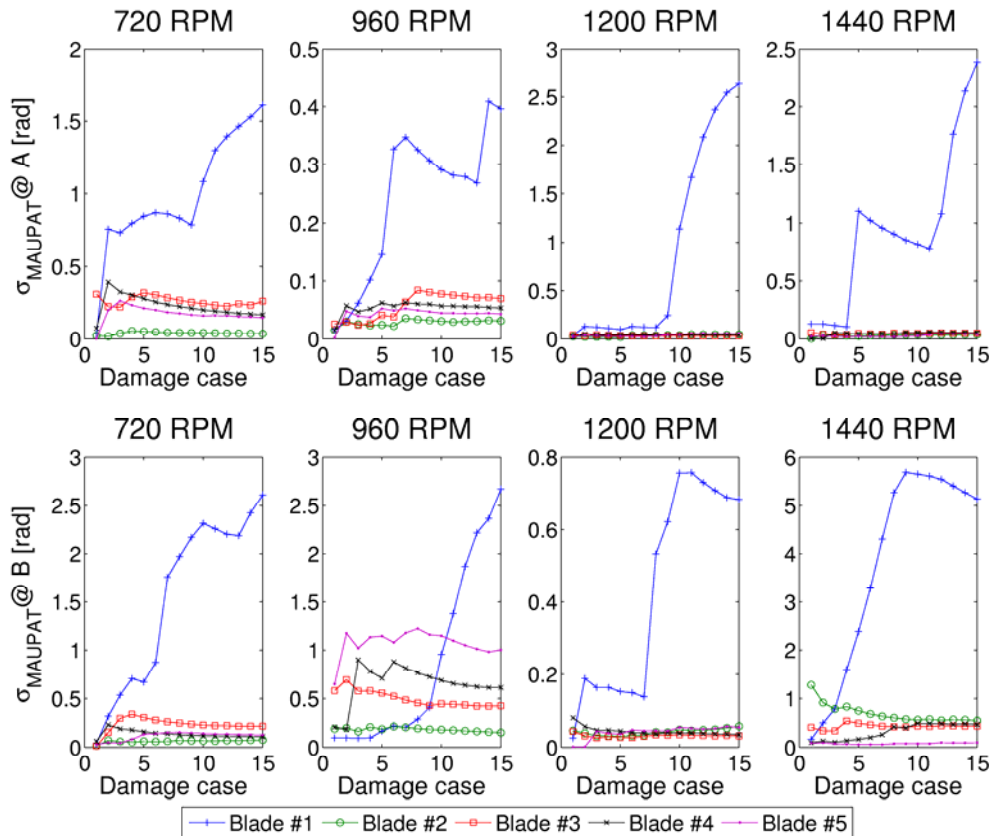

Figure 59: Damage cases 0-15 σ_{MAUPAT} trends around f_1

To obtain more robust results, the averages of the σ_{MAUPAT} trends ($\tilde{\sigma}_{MAUPAT}$) around the remaining f_Rs were calculated after normalization. The outcome is depicted in Figure 60 and it is noted that definite improvement is yielded where trend separation proved to be difficult previously (e.g. position A at 1200 RPM, position B at 960 RPM).
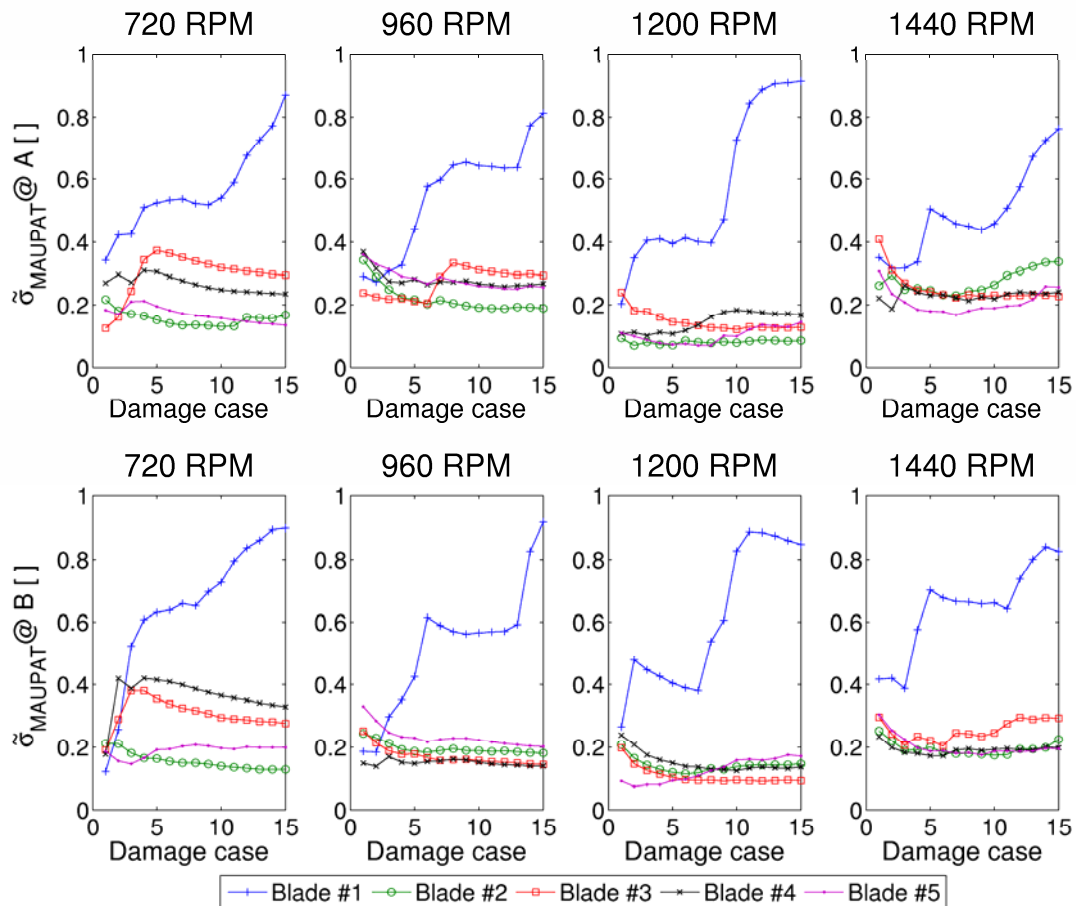

Figure 60: Damage cases 0-15 $\tilde{\sigma}_{MAUPAT}$ trends

The improvements in average trend separation of blade #1 from using σ_{MAUPAT} (Figure 59) and $\tilde{\sigma}_{MAUPAT}$ (Figure 60) are presented in Table 7 relative to the MAUPAT separation around f_1 (Figure 58). It is clear that at various instances, σ_{MAUPAT} trends yield improvement whereas $\tilde{\sigma}_{MAUPAT}$ trends yield deterioration in trend separation, and *vice versa*. Thus the choice of trend for damage detection purposes should receive some consideration, and it may be useful to use the trends in conjunction.

Table 7: Blade #1 trend separation improvement for damage cases 0-15

Rotor speed [RPM]	Trend separation improvement [%]			
	σ_{MAUPAT} @ A	$\tilde{\sigma}_{MAUPAT}$ @ A	σ_{MAUPAT} @ B	$\tilde{\sigma}_{MAUPAT}$ @ B
720	11.62	-23.88	23.89	-7.74
960	149.43	51.64	-44.63	79.89
1200	-6.25	30.57	60.29	47.93
1440	53.83	0.12	15.81	-15.85

When this approach is applied to the measurements of damage cases 16-30, Figure 61 is obtained showing the applicability of the technique when multiple blades are damaged.

To investigate whether further improvement on the trends could be obtained via frequency component isolation prior to NHFA analysis, finite-duration impulse response (FIR) filtering and Vold-Kalman filtering were applied to the signals. However no significant improvement was obtained in the results.
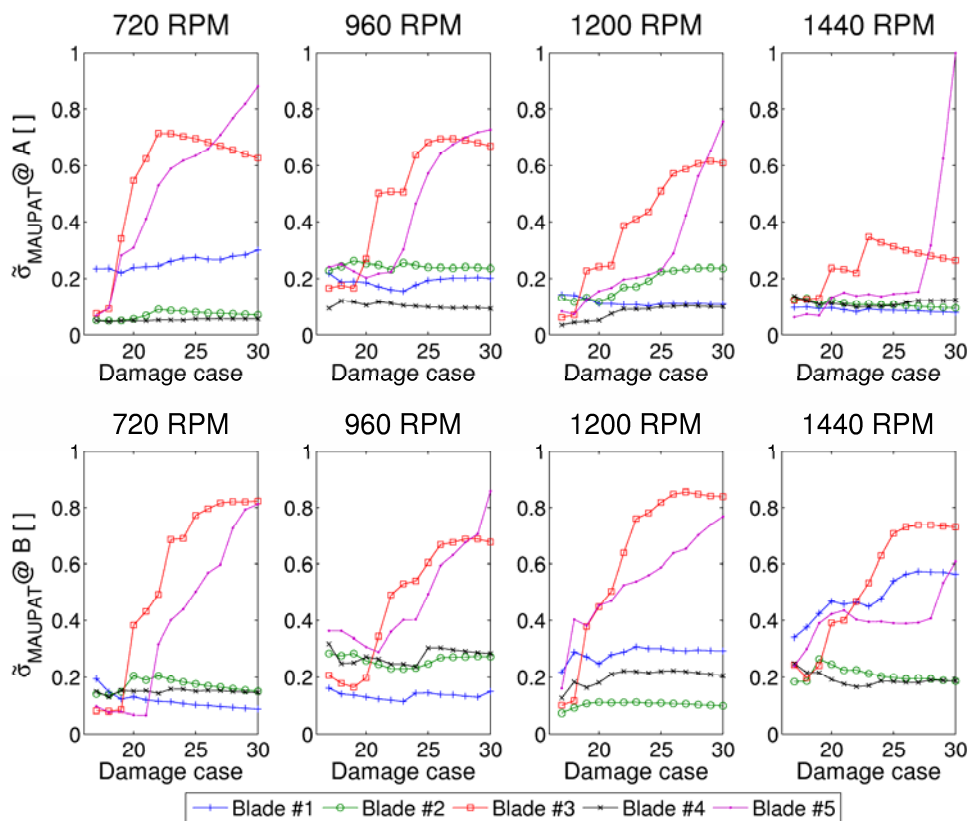

Figure 61: Damage cases 16-30 $\tilde{\sigma}_{MAUPAT}$ trends

4.5.2 Time domain analysis

Various time domain parameters were evaluated namely crest factor, kurtosis, variance, covariance (Norton and Karczub, 2003). Of these RMS and correlation coefficient yielded the best results. Figure 62 and Figure 63 depict the RMS standard deviation trends (σ_{RMS}) for damage cases 0-15 and those of damage cases 16-30 respectively. In general, good results are obtained for all the damage cases except for the lower damage cases at position A at 960 RPM and 1200 RPM. The σ_{RMS} results obtained at position B at 720 RPM for blade #4 erroneously show a strong trend for damage cases 0-15 (Figure 62). As seen from Figure 63, trend separation is poor at 1440 RPM at both measurement locations for damage cases 16-28.

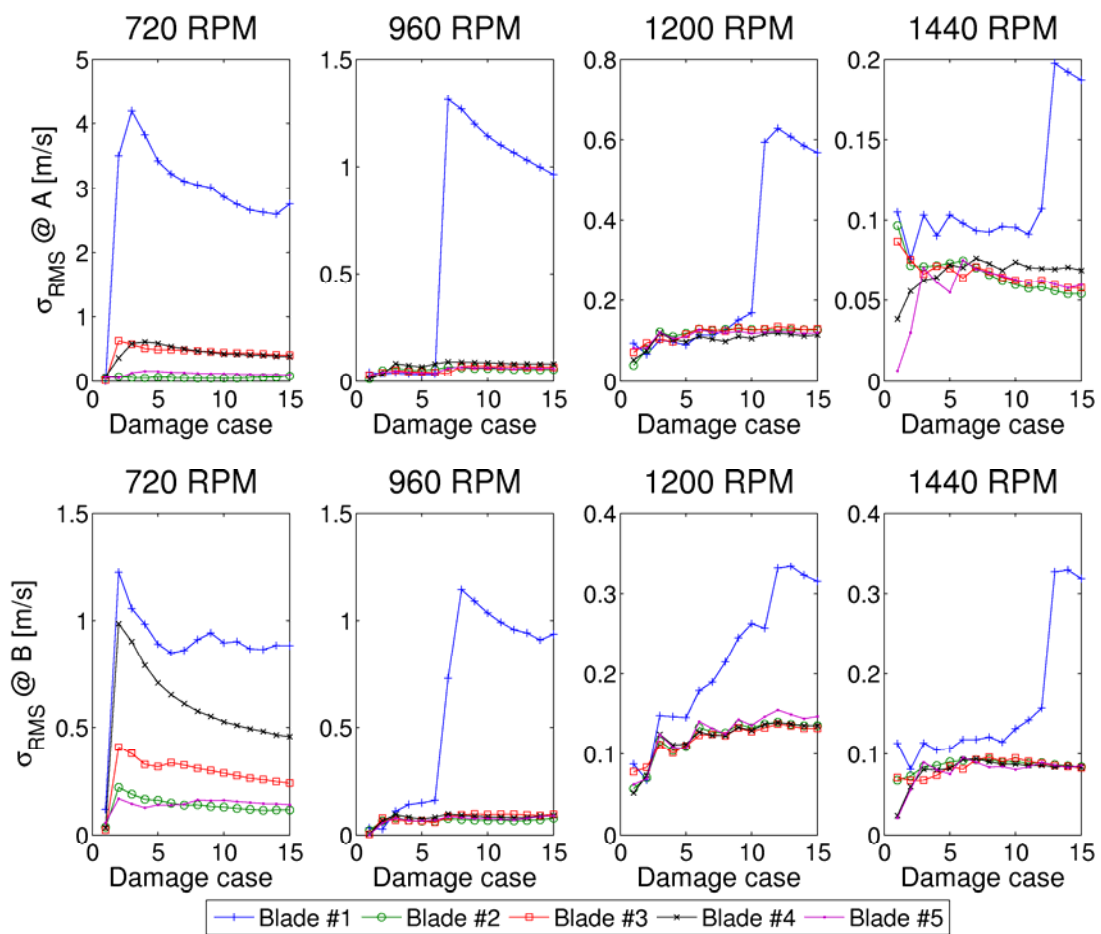**Figure 62: Damage cases 0-15 σ_{RMS} trends**

The trends of correlation coefficient standard deviation (σ_{CORR}) are considered in Figure 64 and Figure 65 for damage cases 0-15 and 16-30 respectively. Again good results are generally obtained for all damage cases.
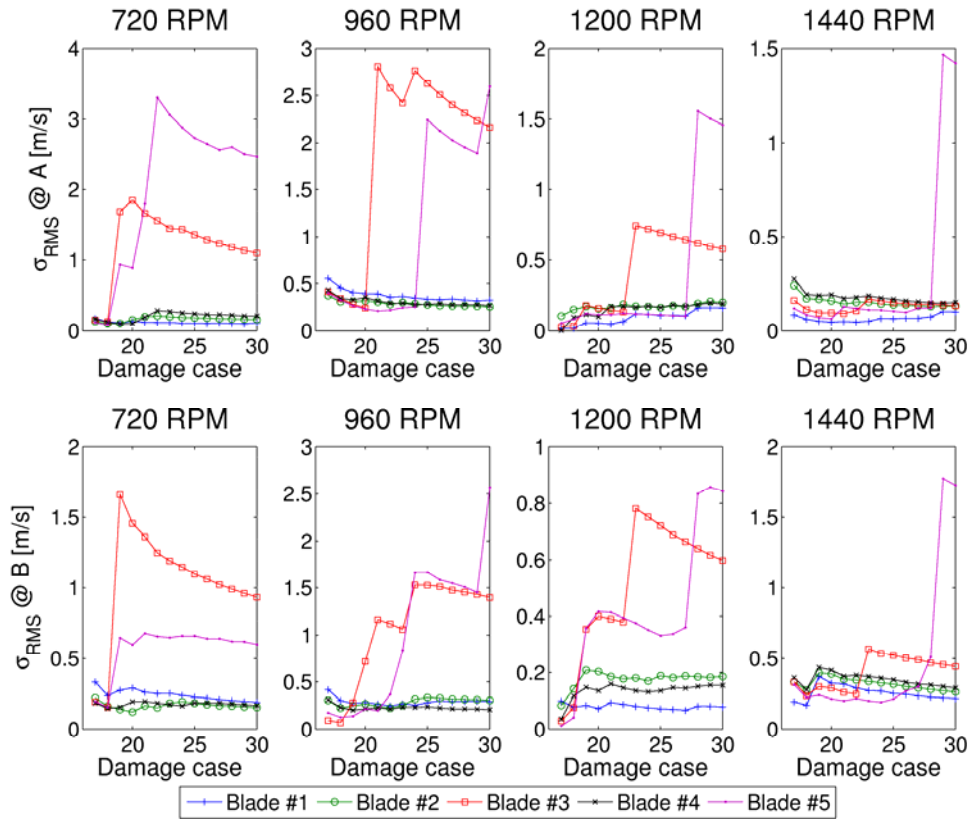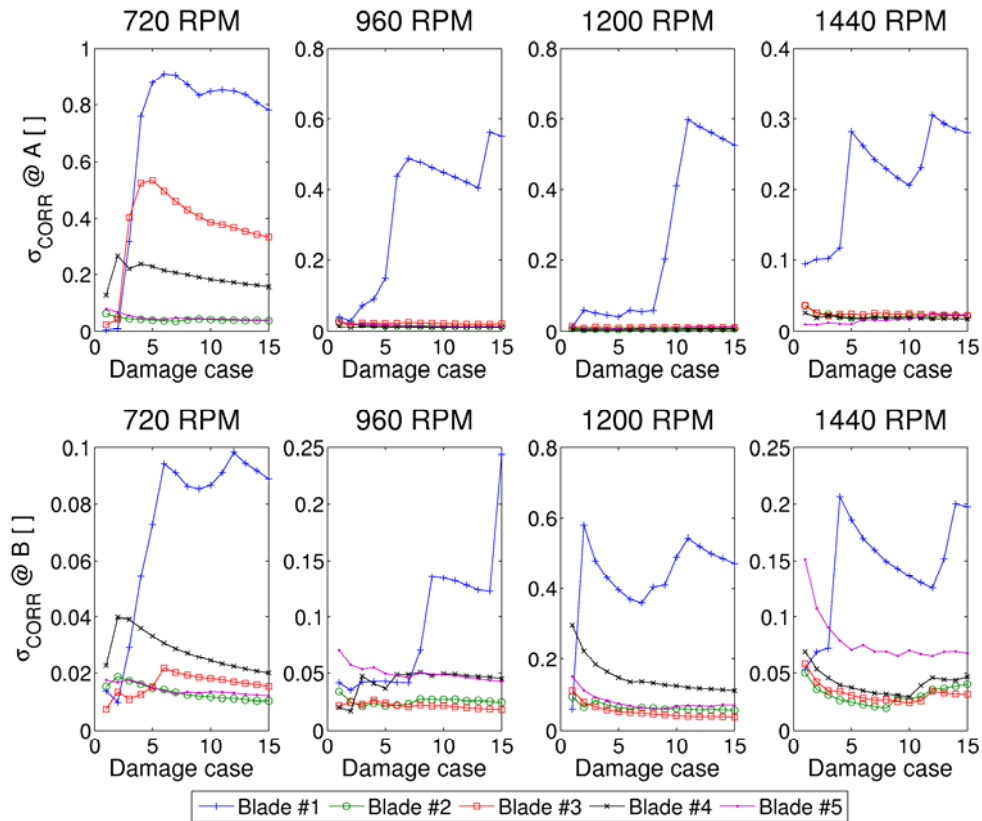
Figure 63: Damage cases 16-30 σ_{RMS} **trends**

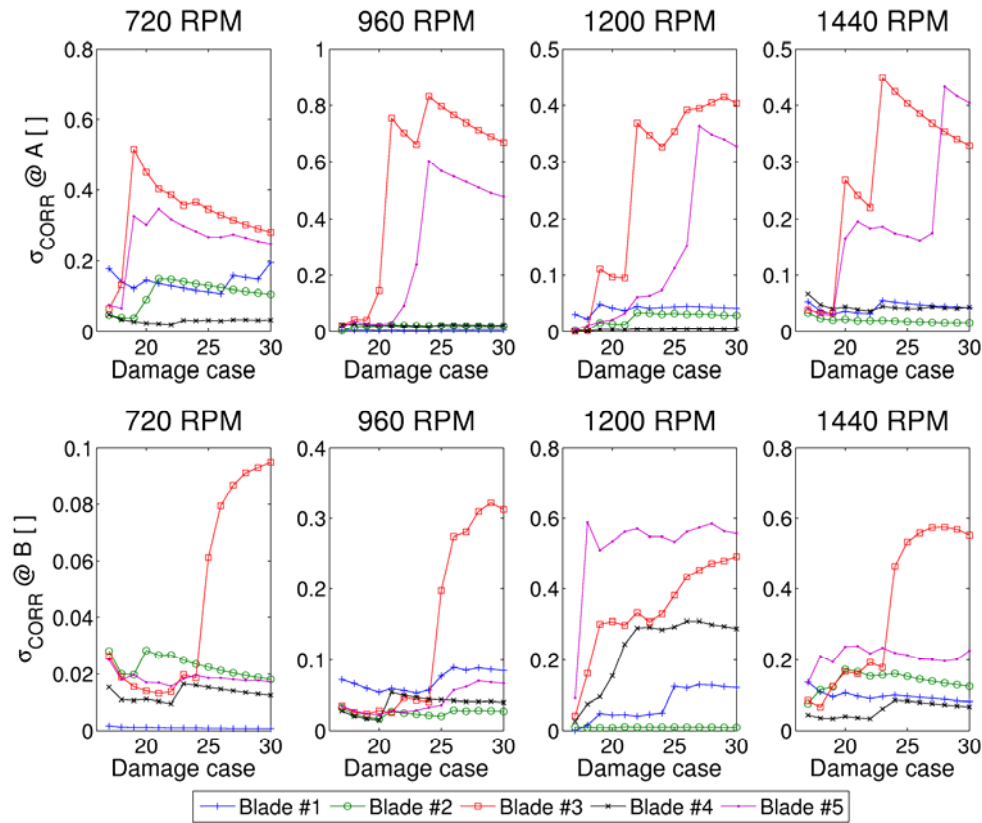**Figure 64: Damage cases 0-15** σ_{CORR} **trends**

Figure 65: Damage cases 16-30 σ_{CORR} trends

An erroneous trend is visible at damage cases 0-15 for blade #3 at position A at 720 RPM (Figure 64). Blade #4 also exhibits strong trends at 720 RPM at both measurement locations for damage cases 0-15. In Figure 65 good results are obtained at position A whereas weak trends are visible for blade #5 at position B except at 1200 RPM. However at position B, a strong σ_{CORR} trend for blade #4 is erroneously indicated at 1200 RPM. Also at both measurement locations, strong erroneous trends for blade #2 are visible at 720 RPM.

4.5.3 ANN implementation

It is evident from the results obtained for $\tilde{\sigma}_{MAUPAT}$, σ_{RMS} and σ_{CORR} that the different parameters need to be considered in conjunction to identify and quantify blade damage accurately. In addition, it is clear that the parameters from multiple ELDV measurement positions are advantageous to this purpose. One approach to efficiently harvesting the information from the diverse parameters is to employ ANNs.

Using an architecture consisting of two layers, one with 14 neurons and the other with a single neuron, a separate ANN was trained for each rotor speed. Tan-Sigmoid transfer functions were used for all the neurons.

Ten different sets of parameters were extracted for each blade from the average of ten ELDV samples for each damage case and rotor speed. Each set consisted of seven parameters, namely $\tilde{\sigma}_{MAUPAT}$ at position A and B, σ_{RMS} at position A and B, σ_{CORR} at position A and B as well as the blade number b. Each network was then trained to yield the blade-specific damage level D_b. A schematic diagram of the ANN architecture is presented in Figure 66.
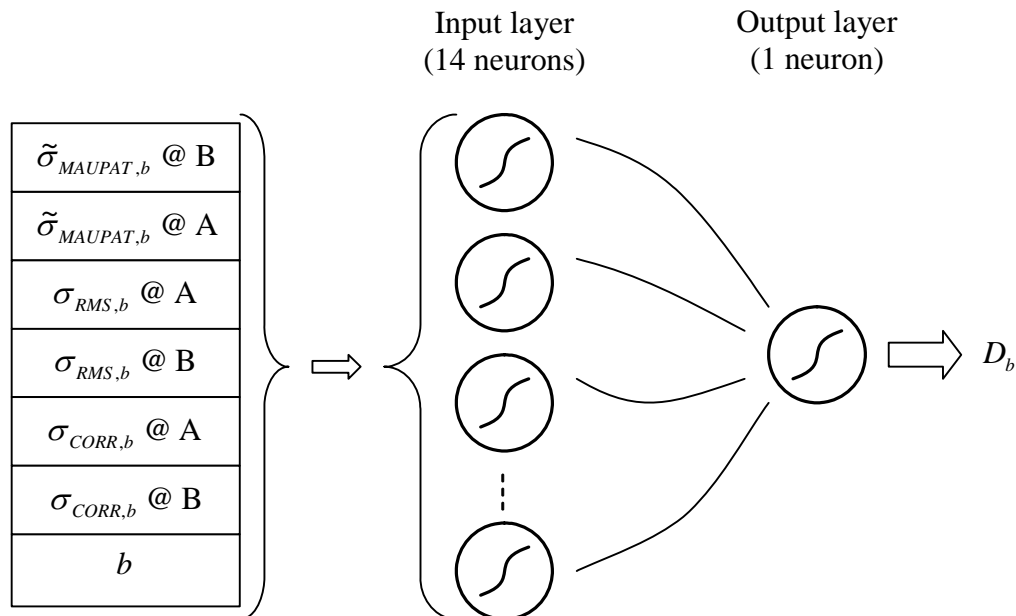

Figure 66: ANN architecture

Following training with eight sets of parameters, each ANN was evaluated with the two remaining sets and the average results are depicted in Figure 67 with the dashed lines representing the ANN training targets. Good results are observed from this figure, showing the ANNs to be capable of both identifying and quantifying blade damage.
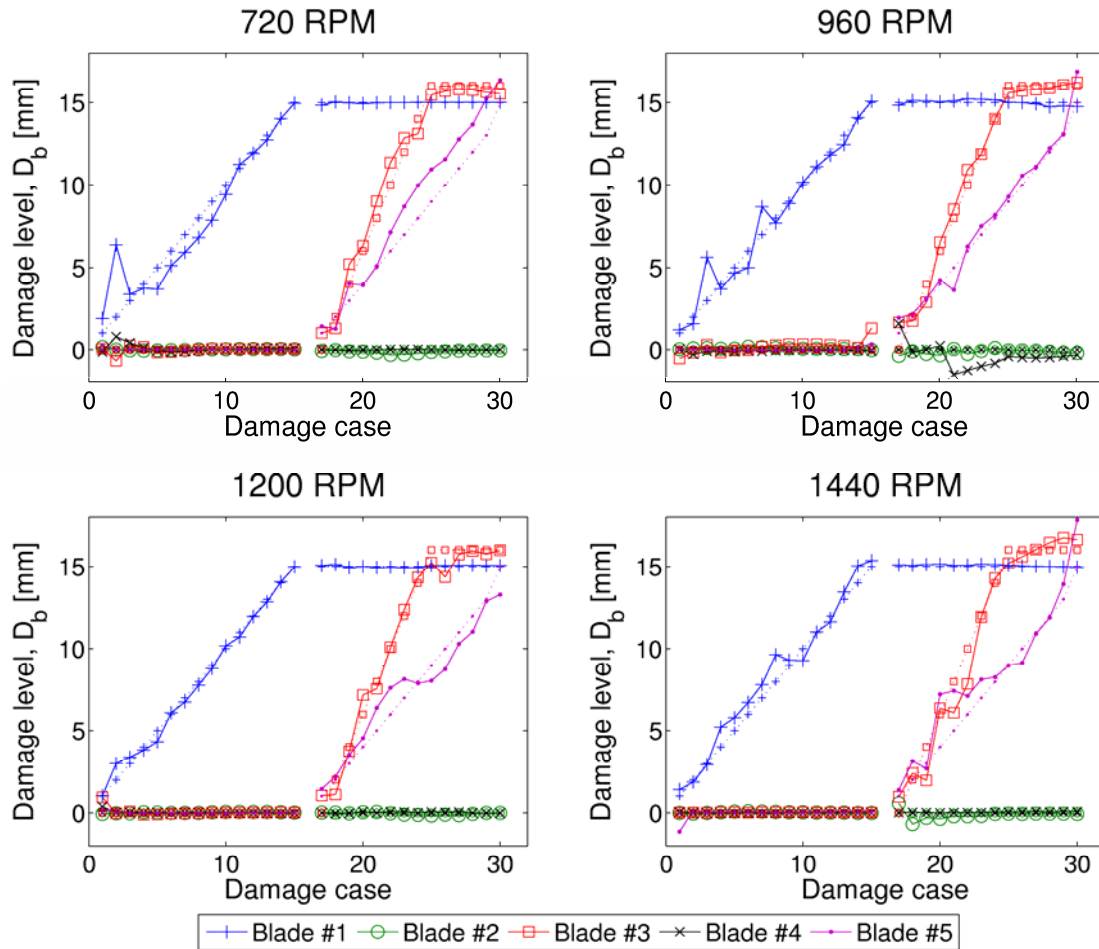
Figure 67: ANN results

4.5.4 Natural frequency estimation

The results presented in Section 4.5.1 to 4.5.3 are useful for identifying and quantifying blade damage relative to a reference point. In order to obtain that reference point, it would be most useful to know the natural frequencies of each individual blade. Although these frequencies can be obtained via offline FRF testing, this approach requires long downtimes and can typically be performed only during outages. It is therefore desirable to estimate the frequencies in an on-line fashion.

In Section 4.4.2 it was shown numerically that ω_1 can be estimated for each blade from run-up and run-down ELDV records. To validate this, ELDV measurements were taken on the test rotor at position A during run-up and run-down events over rotor speeds ranging from 340 RPM to 1440 RPM. The RMS trend of the ELDV run-down signatures of blade #1 at position A is given in Figure 68 for damage case 30, showing a number of peaks.
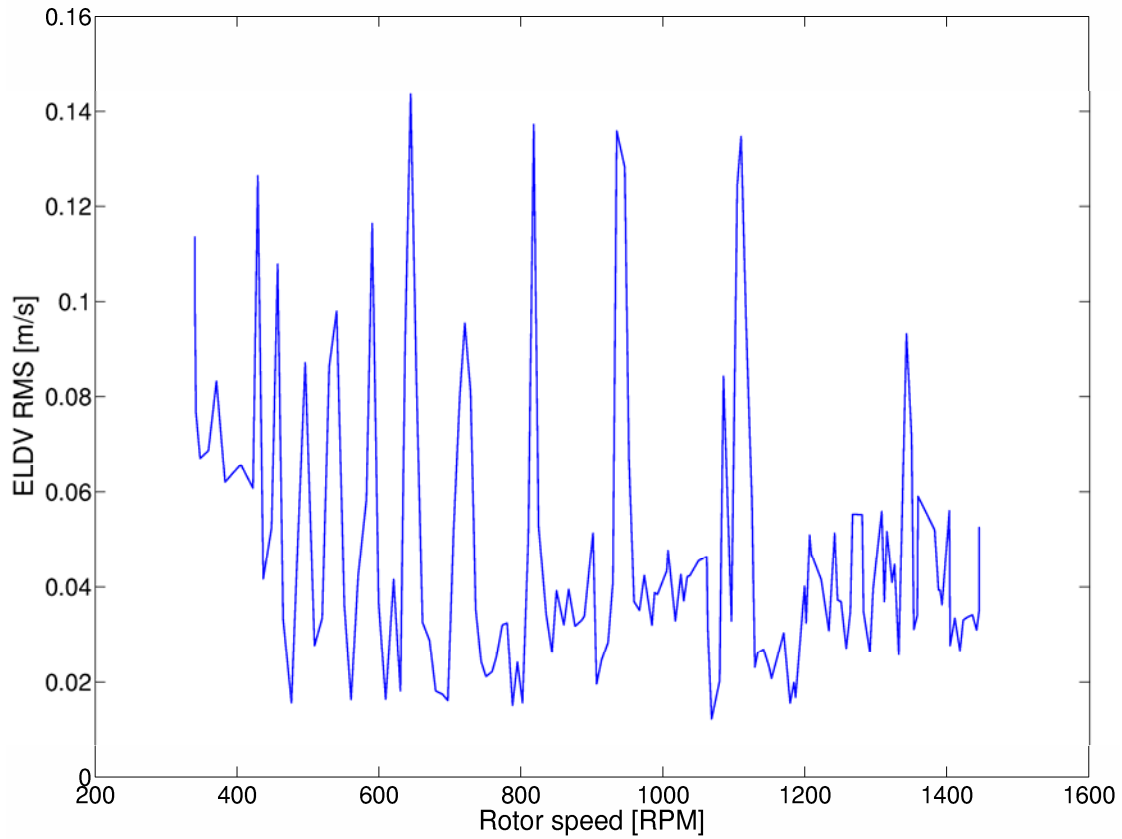
Figure 68: Blade #1 run-down ELDV RMS signature

Consider a vector $\overline{\Psi}$ containing the rotational frequencies ψ in descending order at the predominant peaks:

$$\overline{\Psi} = [\psi_1, \psi_2, ..., \psi_J]$$

<div align="right">**Equation 43**</div>

with $\psi_1 > \psi_2 > ... > \psi_J$ and J is the number of peaks considered.

Since the rotor speed changes and since it can be assumed that ω_1 of each blade remains constant during a run-up or run-down, the rotor order number at each successive RMS peak needs to be incremented. If a vector $\overline{\varepsilon}$ consisting of the rotor order numbers at the RMS peaks is defined as

$$\overline{\varepsilon} = \delta + [1, 2, ..., J]$$

<div align="right">**Equation 44**</div>

with δ an integer constant, a vector $\overline{\omega}$ can be constructed with elements approximating ω_1 by multiplying the elements of $\overline{\Psi}$ and $\overline{\varepsilon}$:

$$\overline{\omega} = \left[\overline{\varepsilon}_1 \overline{\Psi}_1, \ \overline{\varepsilon}_2 \overline{\Psi}_2, \ ..., \ \overline{\varepsilon}_J \overline{\Psi}_J \right]$$

Equation 45

By selecting δ so that the standard deviation of $\overline{\omega}$ is minimized, an estimate of ω_1 can be obtained from the mean of $\overline{\omega}$:

$$\omega_{1,est} = \frac{\overline{\varepsilon} \cdot \overline{\Psi}}{J}$$

Equation 46

Using the results from both a run-up and run-down signature, the average $\omega_{1,est}$ results are listed in Table 8 showing good correlation with the natural frequencies obtained from modal testing on the stationary rotor.

Table 8: Natural frequency estimation

b	FRF frequency [Hz]	$\omega_{1,est}$ [Hz]	% error
1	106.25	109.48	3.04
2	137.5	138.11	0.44
3	103.125	105.04	1.89
4	137.5	138.34	0.61
5	109.375	111.64	2.07

If the machine is operated in such a way that run-up and run-down events occur regularly, $\omega_{1,est}$ can be used as an additional ANN parameter.

4.6 Measurement uncertainty sensitivity analysis

To determine the effects of laser misalignment and speckle noise on the MAUPAT and time domain results, a sensitivity analysis was conducted on the signal processing techniques used in this chapter. In order to obtain a representative speckle noise signal experimentally, ELDV measurements were recorded on the blades in the absence of nozzle excitation. The same opto-reflective material used for the measurements of Section 3.3 and Section 4.5 was utilized again and a typical signal measured at 720 RPM is presented in Figure 69. From this figure, it is clear that the signal is dominated by noise. Since this signal was repeatable, it was readily assumed that noise is directly caused by the opto-reflective material's speckle pattern since speckle noise has a pseudo-random nature (Rothberg, 2006:4526). This signal was then used as part of the sensitivity analysis.
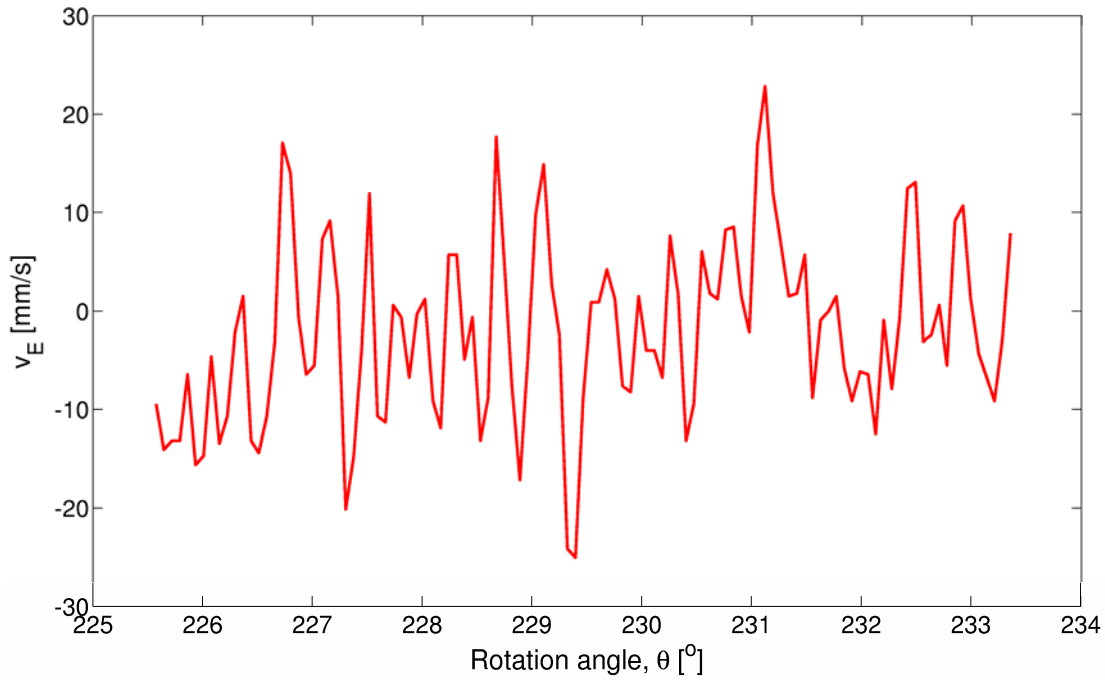
Figure 69: Speckle noise signal

The sensitivity analysis was conducted by adding noise to EVR signals simulated in the FEM at 720 RPM for damage cases 0-15. Six different cases were considered as listed in Table 9.

Table 9: Measurement uncertainty sensitivity analysis case matrix

Case #	Description
1	Stationary speckle noise signal
2	Speckle noise signal phase shift
3	Random speckle noise signals
4	Speckle noise signal frequency increase
5	$+0.227^o$ laser misalignment
6	-0.227^o laser misalignment

Case #1 involved adding the same speckle noise signal to each EVR signature, showing the direct effect of speckle noise presence on the results. With case #2, the same speckle noise signal was shifted 7 samples in time (corresponding to a 13.2^o phase angle shift) for each EVR signature to study the effects of systematic speckle noise phase shift on the results. For case #3, the FFT of the noise signal was calculated. Keeping the resulting FFT amplitudes unchanged, random phase angles were generated.

111

From these, inverse FFTs were calculated resulting in different speckle noise signals with the same frequency content, but with random time domain responses. A different speckle noise signal was then added to each EVR signature, showing the effects of random noise signal change on the results. Case #4 involved simulating a doubling in the speckle noise signal frequency by concatenating the same signal, and then resampling the resulting signal to obtain the original sample length. The same resampled noise signal was added to each EVR signature. Cases #5 and #6 simulated the effects of DC offsets in the ELDV measurements corresponding to a ±5 mm misalignment of the laser beam over the experimental standoff distance of 1.265 m (i.e. ±0.227^o misalignment).

4.6.1 MAUPAT results

The MAUPAT results of these simulations are represented in Figure 70 and Figure 71. The same reference frequencies and ranges listed in Table 6 were used during calculations. It is demonstrated that the addition of a static speckle noise signal affects the results in a limited way (Figure 70 b). However when the speckle noise signal itself changes for each damage case, the effects are more pronounced as seen in Figure 70 (c) and (d). Again in Figure 71 (b) as in Figure 70 (b), adding the same noise signal (in this case with twice the original noise signal frequency) has some effects on the results, though limited. Furthermore it is evident that the additions of DC components have clear effects on the results as demonstrated by Figure 71 (c) and (d). A positive DC component seems to increase the sensitivity of the results to damage whereas a negative DC component has the opposite effect.

When comparing the mean absolute MAUPAT errors for each analysis case over the range of damage levels considered, it becomes plain that results around the different f_{ref} s are affected differently by the different cases considered (Figure 72). In general, f_1 and f_2 are the least affected by the different disturbances whereas the higher f_{ref} s are more sensitive. Cases #2 and #3 (i.e. with dynamic speckle noise signals) yield roughly the same results with f_5, f_6, f_7 and f_9 affected the most by these. Overall does a positive DC offset (case #5) affect most of the f_{ref} s.
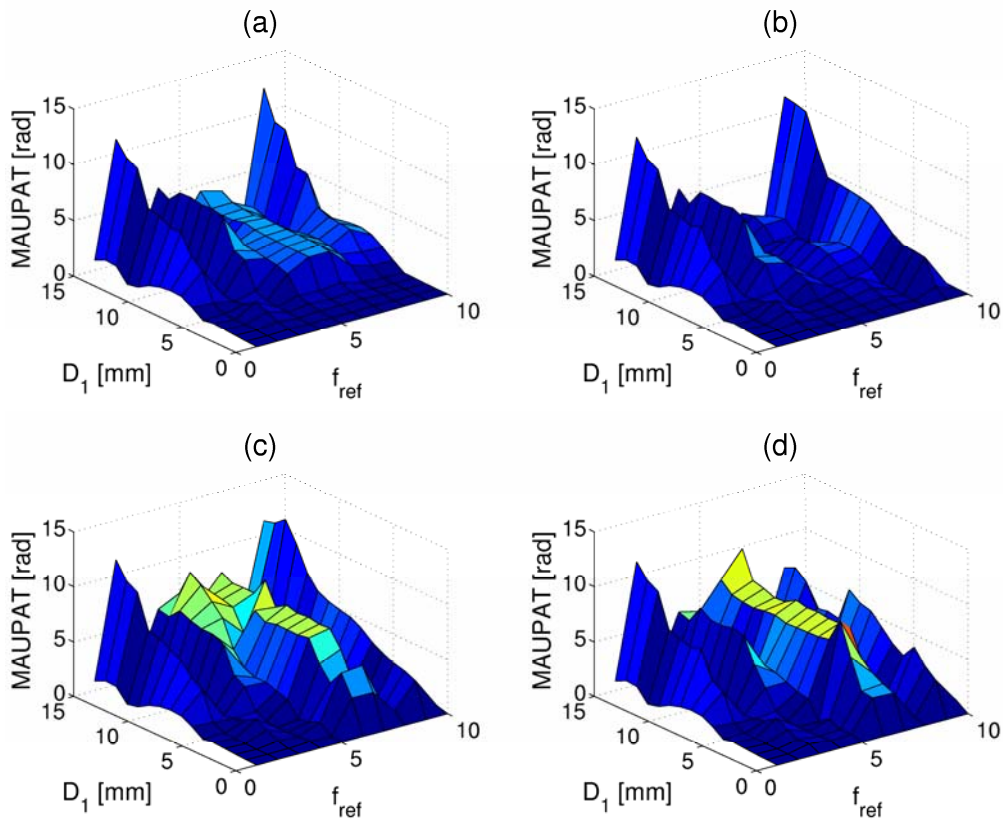
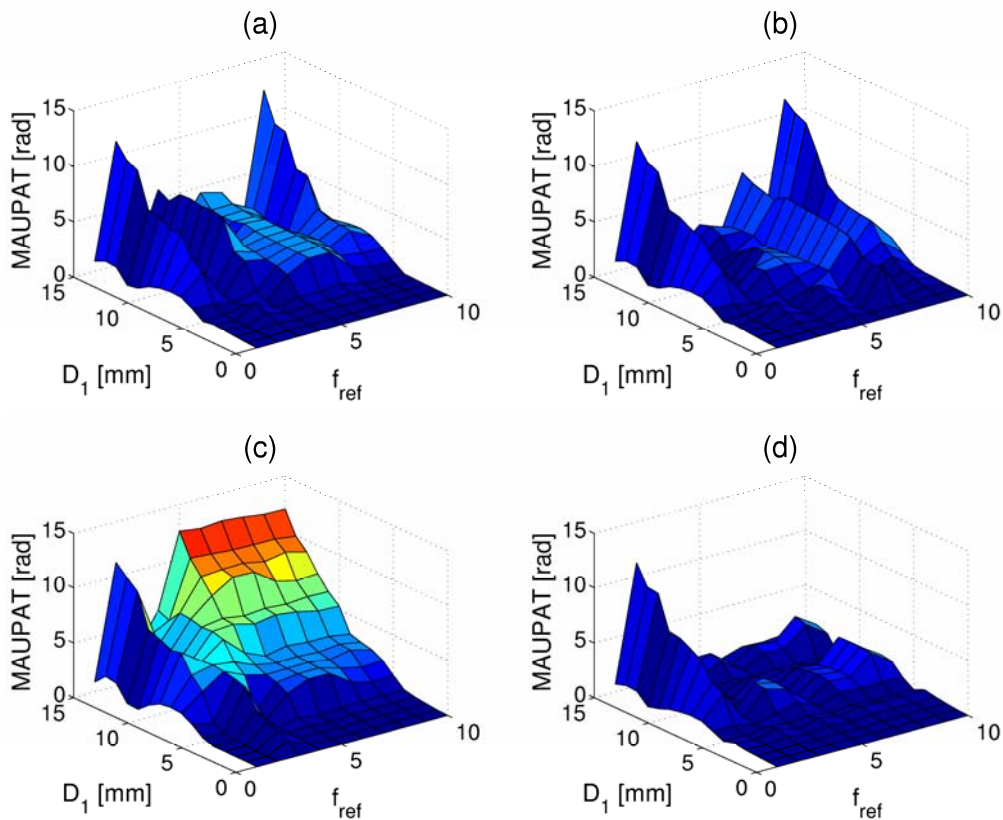**Figure 70: Sensitivity analysis MAUPAT results (a) Ideal (b) Case #1 (c) Case #2 (d) Case #3**

Figure 71: Sensitivity analysis MAUPAT results (a) Ideal (b) Case #4 (c) Case #5 (d) Case #6
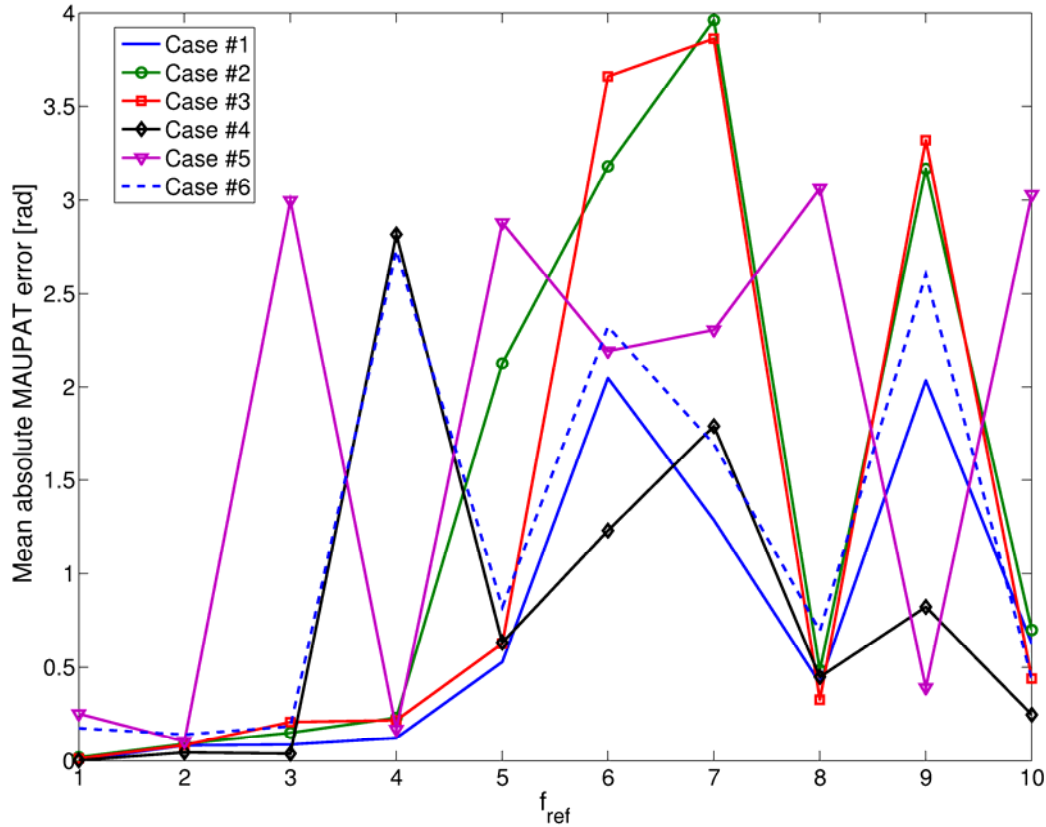
Figure 72: Mean absolute MAUPAT errors

4.6.2 Time domain results

The effects of the different sensitivity analysis cases were also studied on the time domain parameters considered in this chapter (i.e. RMS and correlation coefficient). The results are presented in Figure 73 in terms of mean absolute error.

RMS is affected only slightly for cases #1 to #4 whereas the introduction of DC offsets (cases #5 and #6) has pronounced affects on the RMS values. The opposite is observed for the correlation coefficient results.

4.6.3 Discussion

In the work presented in Chapter 3 and Chapter 4, it was assumed that the speckle noise signals were stationary for each blade for the duration of each damage level and rotor speed value. This assumption was valid since there were no changes (brought on by long term operational effects such as soiling) in the optical properties of the reflective material used during testing that had to be considered.
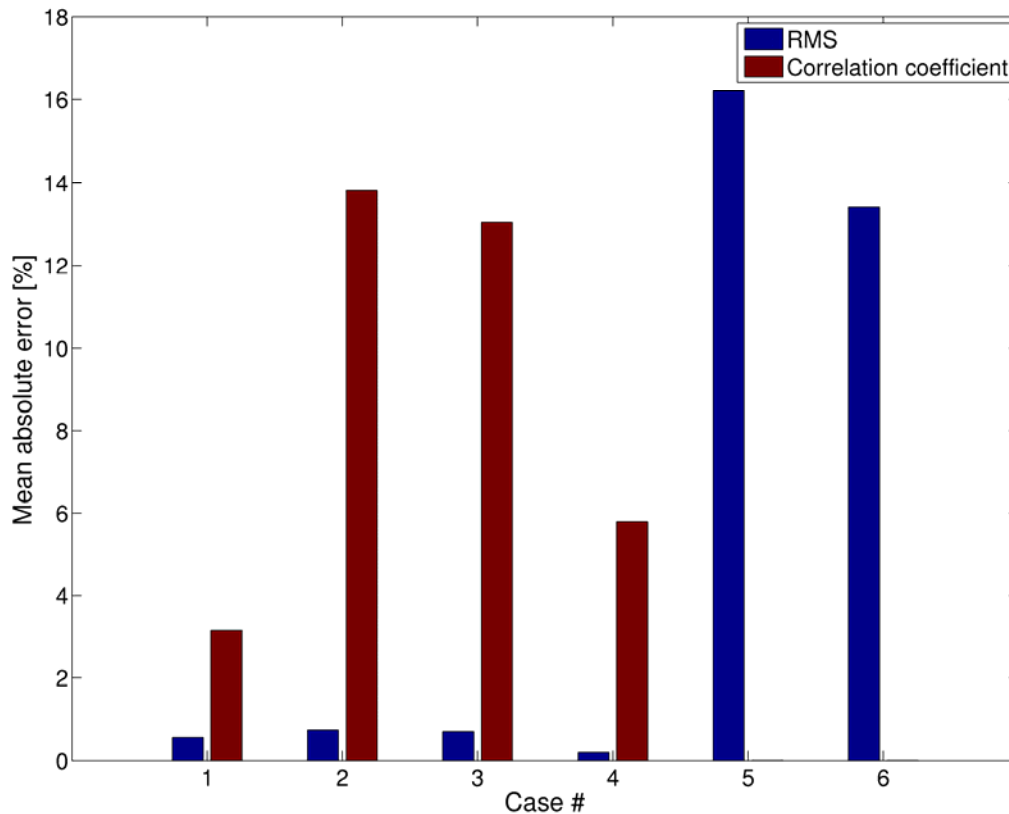
Figure 73: Mean absolute RMS and correlation coefficient errors

Furthermore no changes were made to the laser vibrometer orientation during testing, thus keeping the small misalignment effects constant during testing for each rotor speed value.

Nonetheless the results of the measurement uncertainty sensitivity analysis show that these effects do still influence the MAUPAT and time domain analysis results. In addition to global mode shape effects, this explains why some undamaged blades exhibited strong trends (e.g. Figure 58). However, the data processing approach presented in this chapter (i.e. the use of σ as a parameter) was shown to be sufficiently robust to deal with these uncertainties.

4.7 Conclusions

In this chapter it has been shown that ELDV is viable as an on-line blade condition monitoring tool for multi-blade rotors. Employing both NHFA and time domain analysis on ELDV measurements from a test rotor at two different measurement positions, the parameters yielded were successfully used to train ANNs for the purpose of identifying and quantifying blade deterioration.

It is demonstrated both numerically and experimentally that run-up and run-down ELDV signatures are valuable in approximating the first bending natural frequencies of individual blades and can serve as an additional condition monitoring parameter.

With the aid of sensitivity analyses, it was established that measurement uncertainties in the ELDV measurement techniques do affect the results significantly. The major sources of error were identified to be speckle noise signal dynamics as well as laser misalignment. However the signal and data processing approaches presented in this chapter were shown to be sufficiently robust to deal with these effects.

The work of this chapter is contained in the article titled *"Eulerian laser Doppler vibrometry: Online blade damage identification on a multi-blade test rotor"* (Oberholster and Heyns, In press).

Chapter 5 Conclusions and further work

5.1 Conclusions

This thesis focussed on developing suitable signal processing techniques for ELDV measurements performed on axial-flow turbomachinery blades for the purpose of on-line condition monitoring and damage detection.

From the literature study, it became apparent that little work has been done in the area of ELDV measurements albeit that this area has been studied since the late 1960s.

In Chapter 2, the characteristics of ELDV were analytically studied on a simple cantilever beam based on the Euler-Bernoulli theory for continuous beams. It was shown that, for the cantilever beam translating at a constant speed relative to a stationary LDV, the observed vibration response consists of the combined effects of the amplitude modulation of the various cantilever beam generalized coordinates by their respective (and now time-dependent) characteristic functions. This observation was verified experimentally for a cantilever beam excited at discrete frequencies and moving at slow speeds relative to the LDV. An interpolation approach was proposed and evaluated for the simulation of the ELDV measurement technique in a FEM. Employing reference matrices called LVRMs, it was shown that ELDV can be approximated for various scanning speeds using a fixed nodal resolution in the FEM. Following this, the damage detection capabilities of ELDV were demonstrated numerically. The interpolation demonstrated for longitudinally translating cantilever beams was extended to rotor-axial ELDV on rotating blades. Equations were also presented for rotor-circumferential ELDV measurements.

Chapter 3 focused on ELDV measurements applied to a singe-blade axial-flow test rotor with the laser aligned in the rotor-axial direction. ELDV and TLDV measurements were performed at a fixed rotor speed and increasing blade damage levels and it became apparent that phase angle could be used as a damage indicator. This was verified numerically and after a thorough investigation, NHFA was found to be suitable for extracting phase angle information from the ELDV measurements. It is shown both numerically and experimentally that MAUPATs around reference frequencies provide robust blade health deterioration indicators.

The work of Chapter 3 is extended to a five-blade test rotor in Chapter 4. ELDV and TLDV measurements are considered for multiple blade damage cases at various rotor speeds. It was shown numerically that the phase and amplitude discontinuities

observed in the TLDV measurements in both Chapter 3 and Chapter 4, are as a result of the first bending natural frequency of the damaged blade being in close proximity to one of the rotor orders. Evaluating RMS values, it was shown that ELDV Campbell diagrams of the blades are of importance in experimentally determining the blades' first bending mode frequencies.

As expected for a multi-blade rotor, it was discovered during post-processing that blade damage identification from amongst healthy blades required careful consideration. Exhibiting non-monotonic behaviour with increasing damage, it was necessary to calculate the standard deviations of the MAUPATs. By evaluating this parameter at the various reference frequencies, it was shown that it is possible to produce well defined trends indicative of blade damage. Similar results were obtained from two time domain parameters namely RMS and correlation coefficient values. It was demonstrated that multiple ELDV measurement positions are advantageous to accurately identifying blade damage. ANNs were successfully trained on these parameters and blade damage could subsequently be accurately identified and quantified.

A sensitivity analysis of different measurement uncertainties in Chapter 4 showed that these affect the MAUPAT and time domain results significantly. The signal and data processing approaches presented in this chapter were however found to be significantly robust to deal with these effects.

5.2 Further work

In order to extend the work presented in this thesis to a technique that is practically feasible for on-line blade condition monitoring in an industrial rotor, further work is needed. A research project towards this purpose is currently under way at the Eskom Research and Innovation Division in South Africa.

On the test rotor, high efficiency reflective tape was used to ensure sufficient LDV signal strength during measurements. This of course will not be feasible in an actual operating environment. Reflectivity properties will furthermore vary between new and old blades due to deposition in the blade surfaces. Due to operating environments that are not conducive to the operating conditions required for prolonged LDV operation, it will also be necessary to employ fibre optics for laser beam transmission. The flow medium itself may furthermore affect signal strength as well. All these factors need to be taken into consideration in further work.

The test work that was conducted in this thesis was performed on straight flat rectangular blades with low angles of attack. Typical turbomachinery blades are geometrically more complex and have aerofoil profiles and angles of attack varying along the blade lengths. Although these properties will not directly affect the measurements themselves, they may however prescribe the orientation of the laser beam so as to stay within a reasonable incidence angle range for rotor-axial ELDV measurements. Thus the laser beam orientation may not strictly be in the rotor-axial direction, but it will still mainly provide flap wise vibration information of the blades.

It was shown that multiple ELDV measurement positions are advantageous for accurate blade damage identification. However LDVs are expensive. One solution is to develop a fibre optic SLDV where the laser beam is directed by mirrors (as with normal SLDVs) to various fibres.

Damage was simulated in a controlled manner on the test rotor by means of slot cuts close to the blade roots. It is necessary to verify the technique on blades with true damage.

A number of parameters were presented that provided robust blade damage indicators. These parameters need to be verified at different blade operating conditions. Further work into identifying additional parameters will be valuable to increase the robustness of the technique.

The proposed condition monitoring technique was successfully demonstrated at up to 1440 RPM. The upper limitations of the technique need to be determined.

The technique presented in this thesis was proven for five blades. The technique needs to be verified on rotors such as turbines with a large number of blades.

An LDV was used to obtain on-line blade vibration measurements in an Eulerian fashion in this research. As mentioned earlier, LDVs are however expensive. It will be valuable to identify other instruments and sensors that will provide on-line Eulerian blade vibration information. The presented signal processing techniques can then be applied to these measurements.

UNIVERSITEIT VAN PRETORIA
UNIVERSITY OF PRETORIA
YUNIBESITHI YA PRETORIA

References

Afolabi, D. (1988). *Modal characteristics of turbomachine blades in a multi-stage engine*. Proceedings of the 6th International Modal Analysis Conference: Orlando, Florida, 521-527.

Al-Bedoor, B.O. (2002). Blade vibration measurement in turbo-machinery: Current status. *Shock and Vibration Digest*, 34(6), 455-461.

Antoni, J., Randall, R.B. (2004a). Unsupervised noise cancellation for vibration signals: Part I - Evaluation of adaptive algorithms. *Mechanical Systems and Signal Processing*, 18(1), 89-101.

Antoni, J., Randall, R.B. (2004b). Unsupervised noise cancellation for vibration signals: Part II - A novel frequency-domain algorithm. *Mechanical Systems and Signal Processing*, 18(1), 103-117.

Aono, H., Chikata, T., Hagiwara, Y., Iinuma, H. (1985). *Optical fan blade vibration measurement*. International Congress on Experimental Mechanics: Beijing, China, 571-576.

Aretakis, N., Mathioudakis, K., Dedoussis, V. (1998). Derivation of signatures for faults in gas turbine compressor blading. *Control Engineering Practice*, 6, 969-974.

Balda, M. (2000). *Processing of blade monitoring system data*. Proceedings of the 7th International Conference on Vibrations in Rotating Machinery: Nottingham, UK, 677-685.

Balmès, E. (1997). *Structural Dynamics Toolbox user's guide*. France: Scientific Software.

Beaumont, R. (21 October 2004). Personal communication.

Beauseroy, P., Lengellé, R. (2007). Nonintrusive turbomachine blade vibration measurement system. *Mechanical Systems and Signal Processing*, 21(4), 1717-1738.

Bell, J.R., Rothberg, S.J. (2000). Laser vibrometers and contacting transducers, target rotation and six degree-of-freedom vibration: What do we really measure? *Journal of Sound and Vibration*, 237(2), 245-261.

Bhat, M.M., Ramamurti, V., Sujatha, C. (1996). Studies on the determination of natural frequencies of industrial turbine blades. *Journal of Sound and Vibration*, 196(5), 570-692.

Boutarek, N., Saïdi, D., Acheheb, M.A., Iggui, M., Bouterfaïa, S. (2008). Competition between three damaging mechanisms in the fractured surface of an Inconel 713 superalloy. *Materials Characterization*, 59(7), 951-956.

Brincker, R, Andersen, P., Martinez, M.E., Tallavó, F. (1996). *Modal analysis of an offshore platform using two different ARMA approaches*. Proceedings of the 14th International Modal Analysis Conference: Detroit, Michigan, 1197-1203.

Caponero, M.A., Pasqua, P., Paolozzi, A., Peroni, I. (2000). Use of Holographic interferometry and electronic speckle pattern interferometry for measurements of dynamic displacements. *Mechanical Systems and Signal Processing*, 14(1), 49-62.

Castellini, P., Santolini, C. (1998). Vibration measurements on blades of a naval propeller rotating in water with tracking laser vibrometer. *Measurement*, 24, 43-54.

Cauberghe, B., Guillaume, P., Verboven, P., Parloo, E. (2003). Identification of modal parameters including unmeasured forces and transient effects. *Journal of Sound and Vibration*, 265, 609-625.

Chuckpaiwong, I. (2003). *Development of position sensor using phase-based continuous wave radar*. D.Phil. Thesis. Atlanta: Georgia Institute of Technology.

Cookson, R.A., Bandyopahyay, P. (1980). A fiber-optic laser-Doppler probe for vibration analysis of rotating machines. *Transactions of the ASME: Journal of Engineering for Power*, 102, 607-612.

Davis, Q.V., Kulczyk, K.W. (1969). Vibrations of turbine blades measured by means of a laser. *Nature*, 222, 475-476.

Denman, M., Halliwell, N., Rothberg, S. (1996). *Speckle noise reduction in laser vibrometry: Experimental and numerical optimization.* Proceedings of SPIE: The International Society for Optical Engineering, 2868: Ancona, Italy, 12-21.

Drumm, M., Haase, W.C. (2000). *High performance rotor health monitoring.* Proceedings of the 19th Digital Avionics Systems Conference, 2: Philadelphia, PA, 6E4/1-6E4/8.

Ellis, R., Gulick, D. (1994). *Calculus with analytical geometry.* 5th edition. Florida: Saunders College Publishing.

Ewald, D., Pavlovic, A., Bollinger, J.G. (1971). Noise reduction by applying modulation principles. *The Journal of the Acoustical Society of America*, 49(5A), 1381-1385.

Ewins, D.J. (2000). *Modal testing theory, practice and application.* 2nd edition. Baldock: Research Studies Press.

Fan, Y.C., Ju, M.S., Tsuei, Y.G. (1994). Experimental study on vibration of a rotating blade. *Journal of Engineering for Gas Turbines and Power*, 116, 672-677.

Fangman, C.N., Zastrow, V.A., Bobeck, J.E. (1967). High-speed-turbocharger blade-vibration measurement. *Experimental Mechanics*, 7(1), 19A-21A.

Fante, R.L. (1988). *Signal analysis and estimation: An introduction.* New York: Wiley.

Finke, C., Schmidt, R. (1996). Effizientes Lasermessverfahren zur untersuchung von shaufelschwingungen [Laser technique for efficient blade vibration measurements]. *VDI Berichte*, 1249, 125-138.

Gadala, M.S., Byrne, T.P. (1986). *Modelling of turbine blades for stress and dynamic analysis.* Proceedings of the 4th International Modal Analysis Conference: Los Angeles, CA, 1220-1227.

Gamba, J., Shimamura, T. (2005). Spectrum estimation by noise-compensated data extrapolation. *IEICE Transactions on Fundamentals of Electronics, Communications and Computer Sciences*, E88(3), 702-710.

Giordano, A.A., Hsu, F.M. (1985). *Least square estimation with applications to digital signal processing*. New York: Wiley.

Gloger (1988). *Kendal T 7353 Special Measurements during commissioning*. (WT TVL/88/018). Mülheim: Siemens AG KWU Group.

Halkon, B.J., Rothberg, S.J. (2006). Vibration measurements using continuous scanning laser vibrometry: Advanced aspects in rotor applications. *Mechanical Systems and Signal Processing*, 20(6), 1286-1299.

Halliwell, N.A. (1996). The laser torsional vibrometer: A step forward in rotating machinery diagnostics. *Journal of Sound and Vibration*, 190(3), 399-418.

Hay, A.M. (2002). Dynamic-Q algorithm for constrained optimization: General mathematical programming code (Computer software). Pretoria: University of Pretoria.

Heath, S., Imregun, M. (1998). A survey of blade tip-timing measurement techniques for turbomachinery vibration. *Journal of Engineering for Gas Turbines and Power*, 120(4), 784-791.

Hirata, Y. (2005). Non-harmonic Fourier analysis available for detecting very low-frequency components. *Journal of Sound and Vibration*, 287(3), 611-613.

Hollkamp, J.J., Gordon, R.W. (2001). Modal test experiences with a jet engine fan model. *Journal of Sound and Vibration*, 248(1), 151-165.

Holst, T.A. (2005). *Analysis of spatial filtering in phase-based microwave measurements of turbine blade tips*. Master's Thesis. Atlanta: Georgia Institute of Technology.

Hueck, U. (19 March 2004). Personal communication.

Hwang, Y., Lee, I., Lee, J.M., Lee, S.B. (2006). *A new online rotor condition monitoring method using FBG sensors and no telemetry system*. Proceedings of the 13th International Congress on Sound and Vibration: Vienna, Austria, 390-397.

Imregun, M., Visser, W.J. (1991). A review of model updating techniques. *The Shock and Vibration Digest*, 23, 9-20.

Imregun, M., Visser, W.J., Ewins, D.J. (1995). Finite element model updating using frequency response function data: I. Theory and initial investigation. *Mechanical Systems and Signal Processing*, 9(2), 187-202.

Infante, V., Silva, J.M., de Freitas, M., Reis, L. (2009). Failures analysis of compressor blades of aeroengines due to service, *Engineering Failure Analysis*, 16(4), 1118-1125.

Irretier, H. (1988). Free and forced vibrations of turbine blades. In *Rotordynamics 2: Problems in turbomachinery*. Edited by Rieger, N.F. Italy: International Centre for Mechanical Sciences, 397-422.

Jacobs, G.B., Grady, G. (1977). Turbine blade vibration sensor. *IEEE Journal of Quantum Electronics*, 13(9), 827-828.

Jacobs, S., De Roeck, G. (2003). *Dynamic testing of a pre-stressed concrete beam*. Proceedings of the 6th National Congress on Theoretical and Applied Mechanics: Ghent, Belgium.

Kadoya, Y., Mase, M., Kaneko, Y., Umemura, S., Oda, T., Johnson, M.C. (1995). Noncontact vibrational measurement technology of steam turbine blade. *JSME International Journal,* Series C, 38(3), 486-493.

Kielb, J.J., Abhari, R.S. (2003). Experimental study of aerodynamic and structural damping in a full-scale rotating turbine. *Journal of Engineering for Gas Turbines and Power*, 125(1), 102-112.

King, S., Anuzis, P., King, D., Tarassenko, L., Utete, S., McGrogan, N. (2006). *A review of applications for advanced engine health monitoring in civil aircraft engines*. Proceedings of the 13th International Congress on Sound and Vibration: Vienna, Austria, 15-22.

Kulczyk, W.K., Davis, Q.V. (1970). Laser measurements of vibrations on rotating objects. *Opto-Electronics*, 2, 177-179.

Kulczyk, W.K., Davis, Q.V. (1973). Laser Doppler instrument for measurement of vibration of moving turbine blades. *Proceedings of the Institute of Electrical Engineers*, 120(9), 1017-1023.

Kumar, S., Roy, N., Ganguli, R. (2007). Monitoring low cycle fatigue damage in turbine blade using vibration characteristics. *Mechanical Systems and Signal Processing*, 21(1), 480-501.

Leissa, A.W. (1969). *Vibration of plates* (SP-160), Washington: NASA.

Lesne, J.L., Fevrier, T., Triquigneaux, P., Le Floc'h, C. (1985). *Vibratory analysis of a rotating bladed disk using holographic interferometry and laser vibrometry*. Proceedings of SPIE - The International Society for Optical Engineering, 599, Cannes, France, 74-79.

Lobos, T., Leonowicz, Z., Rezmer, J., Schegner, P. (2006). High-resolution spectrum-estimation methods for signal analysis in power systems. *IEEE Transactions on Instrumentation and Measurement*, 55(1), 219-225.

Lv, J., Wang, J., Chen, D. (2003). *Experimental studies for micro helicopter blade dynamics*. 5th International Symposium on Test and Measurement: Shenzhen, China, 33-36.

Mansisidor, M.R. (2002). *Resonant blade response in turbine rotor spin tests using a laser-light probe non-intrusive measurement system*. Master's Thesis. California: Naval Postgraduate School.

Marple, S.L. (1987). *Digital spectral analysis with applications*. New Jersey: Prentice-Hall.

Martarelli, M., Ewins, D.J. (2006). Continuous scanning laser Doppler vibrometry and speckle noise occurrence. *Mechanical Systems and Signal Processing*, 20(8), 2277-2289.

Mathwin, K. (March 2004). Personal communication.

Maynard, K., Trethewey, M., Gill, R., Resor, B. (2001). *Gas turbine blade and disk crack detection using torsional vibration monitoring: A feasibility study*. Proceedings

of 14th International Congress on Condition Monitoring and Diagnostic Engineering Management: Manchester, UK.

Mazur, Z., Garcia-Illescas, R., Aguirre-Romano, J., Perez-Rodriguez, N. (2008). Steam turbine blade failure analysis. *Engineering Failure Analysis*, 15(1-2), 129-141.

Mazur, Z., Hernández-Rossette, A., García-Illescas, R. (2006). Investigation of the failure of the L-0 blades. *Engineering Failure Analysis*, 13(8), 1338-1350.

Muraoka, T., Nishioka, Y. (2004). *Separation of adjacent frequency components in Generalized Harmonic Analysis (GHA)*. Proceedings of the 46th IEEE International Midwest Symposium on Circuits and Systems, 2: Hiroshima, Japan, II157-II160.

Newby, M. (21 October 2004). Personal communication.

Nikolic, M., Petrov, E.P., Ewins, D.J. (2007). Coriolis forces in forced response analysis of mistuned bladed disks. *Journal of Turbomachinery*, 129(4), 730-739.

Norton, M.P., Karczub, D.G. (2003). *Fundamentals of noise and vibration analysis for engineers*. 2nd edition. Cambridge: Cambridge University Press.

Oberholster, A.J., Heyns, P.S. (2006). On-line fan blade damage detection using neural networks. *Mechanical Systems and Signal Processing*, 20(1), 78-93.

Oberholster, A.J., Heyns, P.S. (2008). *A study of the non-harmonic Fourier analysis technique*. Proceedings of the 21st International Congress on Condition Monitoring and Diagnostic Engineering Management: Prague, Czech Republic, 361-370.

Oberholster, A.J., Heyns, P.S. (2009). Online condition monitoring of axial-flow turbomachinery blades using rotor-axial Eulerian laser Doppler vibrometry. *Mechanical Systems and Signal Processing*, 23(5), 1634-1643.

Oberholster, A.J., Heyns, P.S. (In press). Eulerian laser Doppler vibrometry: Online blade damage identification on a multi-blade test rotor. *Mechanical Systems and Signal Processing*. (DOI 10.1016/j.ymssp.2010.03.007).

Orsagh, R.F., Roemer, M.J. (2002). *Examination of successful modal analysis techniques used for bladed-disk assemblies*. Proceedings of the 56th Conference Of

The Society For Machinery Failure Prevention Technology: Virginia Beach, VA, 495-506.

Pfister, T., Buttner, L., Czarske, J., Krain, H., Schodl, R. (2006). Turbo machine tip clearance and vibration measurements using a fibre optic laser Doppler position sensor. *Measurement Science and Technology*, 17(7), 1693-1705.

Pruemont, A. (2002). *Vibration control of active structures: An introduction.* 2nd edition. Belgium: Kluwer Academic Publishers.

Rao, J.S., Sreenivas, R. (2003). *Dynamics of asymmetric rotors using solid models.* Proceedings of the International Gas Turbine Congress: Tokyo, Japan, TS-016.

Rao, J.S., Vyas, N.S. (1985). *Response of steam turbine blades subjected to distributed harmonic nozzle excitation.* Proceedings of the 3rd International Modal Analysis Conference: Orlando, Florida, 618-626.

Rao, S.S. (1995). *Mechanical vibrations.* 3rd edition. New York: Addison-Wesley Publishing Company.

Reinhardt, A.K., Kadambi, J.R., Quinn, R.D. (1995). Laser vibrometry measurements of rotating blade vibrations. *Transactions of the ASME: Journal of Engineering for Gas Turbines and Power*, 117(3), 484-488.

Rieger, N.F. (1988). The diagnosis and correction of steam turbine blade problems. In *Rotordynamics 2: Problems in turbomachinery.* Edited by Rieger, N.F. Italy: International Centre for Mechanical Sciences, 453-483.

Rothberg, S. (2006). Numerical simulation of speckle noise in laser vibrometry. *Applied Optics*, 45(19), 4523-4533.

Rothberg, S.J., Baker, J.R., Halliwell, N.A. (1989). Laser vibrometry: Pseudo-vibrations. *Journal of Sound and Vibration*, 135(3), 516-522.

Schwingshackl, C., Massei, L., Zang, C., Ewins, D. (2010). A constant scanning LDV technique for cylindrical structures: Simulation and measurement. *Mechanical Systems and Signal Processing*, 24(2), 394-405.

127

Sever, I.A. (2004). *Experimental validation of turbomachinery blade vibration predictions*. D.Phil. Thesis. London: University of London.

Shen, F., Zheng, M., Feng Shi, D., Xu, F. (2003). Using the cross-correlation technique to extract modal parameters on response-only data. *Journal of Sound and Vibration*, 259(5), 1163-1179.

Simani, S. (2005). Identification and fault diagnosis of a simulated model of an industrial gas turbine. *IEEE Transactions on Industrial Informatics*, 1(3), 202-216.

Singh, M.P. (1998). Probabilistic estimation of the effect of dimensional tolerance for turbine/compressor blade attachment. *American Society of Mechanical Engineers: Pressure Vessels and Piping Division*, 381, 247-251.

Spicer, D. (03 April 2003a). Draft report on Duvha explosion next week. *Engineering News*, n.p.

Spicer, D. (18 April 2003b). Duvha set for refurb after explosion. *Engineering News*, n.p.

Sreenivasamurthy, S., Ramamurti, V. (1981). Coriolis effect on the vibration of flat rotating low aspect ratio cantilever plates. *Journal of Strain Analysis*, 16(2), 97-106.

Sriram, P., Hanagud, S., Craig, J.I. (1992). Mode shape measurement using a scanning laser Doppler vibrometer. *International Journal of Analytical and Experimental Modal Analysis*, 7(3), 169-178.

Stanbridge, A.B., Ewins, D.J. (1996). *Using a continuously-scanning laser Doppler vibrometer for modal testing*. Proceedings of the 14th International Modal Anlaysis Conference: Detroit, Michigan, 816-822.

Stanbridge, A.B., Ewins, D.J. (1999). Modal testing using a scanning laser Doppler vibrometer. *Mechanical Systems and Signal Processing*, 13(2), 225-270.

Steele, K.E. (1999). Ocean wave heave time series as the sum of nonharmonic signals. *Ocean Engineering*, 26(12), 1335-1357.

Tappert, P., Von Flotow, A., Mercadal, M. (2001). Autonomous PHM with blade-tip sensors: Algorithms and seeded fault experience. *IEEE Proceedings of the Aerospace Conference*, 7, 3287-3295.

The Mathworks. (2006). Signal *Processing Toolbox for use with Matlab: User's guide*. Natick: The Mathworks, Inc.

Truman, J.C., Martin, J.R., Klint, R.V. (1961). Pulsed-air vibration technique for testing high-performance turbomachinery blading. *Experimental Mechanics*, 1(6), 201-205.

Vanlanduit, S., Daerden, F., Guillaume, P. (2007). Experimental modal testing using pressurized air excitation. *Journal of Sound and Vibration*, 299(1-2), 83-98.

Visser, J. (20 September 2004). Personal communication.

Von Flotow, A., Mercadal, M., Tappert, P. (2000). Health monitoring and prognostics of blades and disks with blade tip sensors. *IEEE Aerospace Conference Proceedings*, 6, 433-440.

Watkins, W.B., Chi, R.M. (1989). Noninterference blade-vibration measurement system for gas turbines. *Journal of Propulsion and Power*, 5(6), 727-730.

White, F.M. (1999). *Fluid mechanics.* 4th edition. Singapore: McGraw-Hill.

Wilmshurst, T.H., Halliwell, N.A. (1993). Laser vibrometer speckle-noise cancellation. *Measurement Science and Technology*, 4(4), 479-487.

Wu, M.C., Huang, S.C. (1998). On the vibration of a cracked rotating blade. *Shock and Vibration*, 5(5), 317-323.

Yang, K., Cho, C., Bae, C., Kim, G., Lee, W., Song, O. (2006). Study on changes of dynaic characteristics according to cracked condition in a turbine blade. Proceedings of the 13th International Congress on Sound and Vibration, 468-475.

Ziegler, H. (1994). Measuring turbine blade vibration. *ABB Review*, 1(9), 31-34.

References

Zielinski, M., Ziller, G. (2000). Noncontact vibration measurements on compressor rotor blades. *Measurement Science and Technology*, 11(7), 847-856.

Appendix A Rotor-Circumferential ELDV

A.1 Introduction

Whereas rotor-axial ELDV provides information on mainly the flap-wise on torsional vibration behaviour of the blade, the question arises whether any useful information is available from sideways vibration behaviour. To investigate this, it is necessary to align the LDV to measure along the blade leading edge in the plane of rotation as given in Figure 74 for a single-blade rotor. This will henceforth be referred to as Rotor-Circumferential (RC) ELDV. Jacobs and Grady (1977) present a system that allows RC TLDV using a scanning mirror directing the laser beam on a parabolic mirror. However no literature could be found on RC ELDV.

Evaluating Figure 74, it is clear that the circumferential speed of the blade will affect the measurements. Also the incidence angle of the laser beam relative to the blade edge normal will change continuously. Furthermore it is important to establish whether the ELDV scanning speed remains constant over the blade leading edge at a constant rotation speed. To address these issues, it is necessary to employ vector-loop calculations.
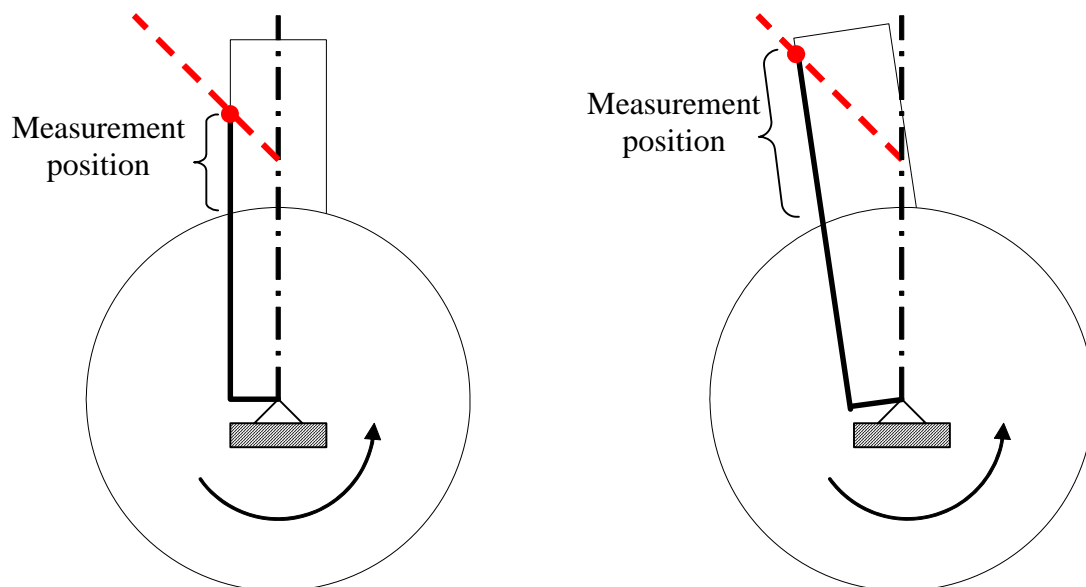

Figure 74: Effect of blade rotation on LDV measurement position

A.2 RC ELDV mathematical definition

A.2.1 Vector-loop equations

An equivalent mechanical system of the RC ELDV measurement technique is shown in Figure 75 along with its corresponding vector-loop diagram and the coordinate system used. It is important to define here the Mean Blade Leading Edge Curve (MBLEC). The MBLEC is obtained by drawing a straight line through the mean of the actual Blade Leading Edge Profile (BLEP) as demonstrated in Figure 76 for an arbitrary BLEP.
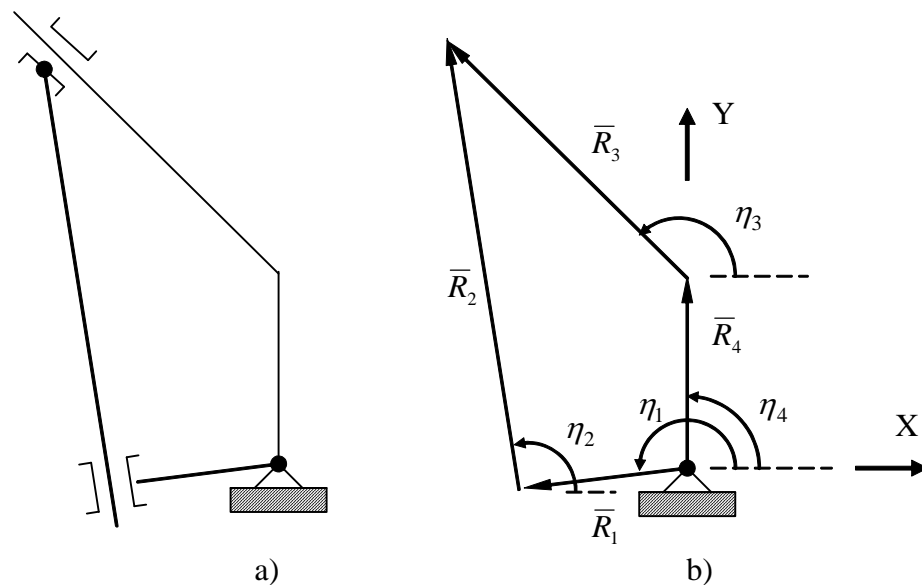

Figure 75: a) Equivalent mechanical system b) Vector-loop diagram

The vector notation used given by Equation 47:

$$\overline{R}_h = \left|\overline{R}_h\right| e^{i\angle\overline{R}_h} = R_h e^{i\eta_h}$$

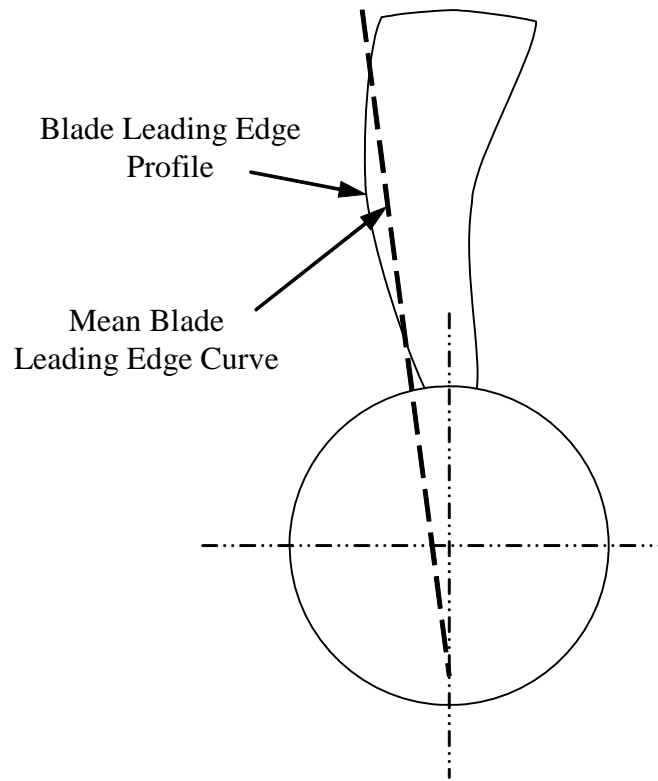**Equation 47**

with *h* the vector number.

Figure 76: Mean Blade Leading Edge Curve

The four vectors shown in Figure 75 can be defined as follows:

1. $\overline{R}_1$ describes the MBLEC offset. It starts from the rotation axis and terminates at its intersection to the MBLEC, perpendicular to that curve. This results in

$$\eta_2 = \eta_1 - 90^o$$

Equation 48

which leads to the trigonometric relationships

$$\cos\eta_2 = \sin\eta_1$$
$$\text{and} \quad \sin\eta_2 = -\cos\eta_1$$

Equation 49

2. $\overline{R}_2$ defines the instantaneous measurement position of the laser beam on the MBLEC.
3. $\overline{R}_3$ gives the laser orientation and reaches from the laser beam intersection with the ZY plane to the measurement point location, which is at the end of $\overline{R}_2$.
4. $\overline{R}_4$ is defined as the laser offset vector, starting from the rotation axis along the ZY plane to the start of $\overline{R}_3$.

Along with the vector definitions, the following assumptions are made:

1. RC blade vibration is ignored along with any motion of the centre of rotation of the shaft from the coordinate system origin. This means that $\overline{R}_1$ and $\overline{R}_2$ remain perpendicular and that $\overline{R}_4$ and R_1 are constant.

2. The LDV is furthermore assumed to be perfectly stationary. As a result, η_3 is constant as well.

Using the vector-loop method, Equation 50 is obtained:

$$\overline{R}_1 + \overline{R}_2 - \overline{R}_3 - \overline{R}_4 = 0$$

$$R_1 e^{i\eta_1} + R_2 e^{i\eta_2} - R_3 e^{i\eta_3} - R_4 e^{i\eta_4} = 0$$

Equation 50

Rearranging for the real part of Equation 50:

$$R_1 \cos\eta_1 + R_2 \cos\eta_2 - R_3 \cos\eta_3 - R_4 \cos\eta_4 = 0$$

$$R_1 \cos\eta_1 + R_2 \sin\eta_1 - R_3 \cos\eta_3 = 0$$

$$R_2 \sin\eta_1 - R_3 \cos\eta_3 = -R_1 \cos\eta_1$$

Equation 51

Rearranging for the imaginary part of Equation 50:

$$R_1 \sin\eta_1 + R_2 \sin\eta_2 - R_3 \sin\eta_3 - R_4 \sin\eta_4 = 0$$

$$R_1 \sin\eta_1 - R_2 \cos\eta_1 - R_3 \sin\eta_3 - R_4 = 0$$

$$-R_2 \cos\eta_1 - R_3 \sin\eta_3 = R_4 - R_1 \sin\eta_1$$

Equation 52

To calculate velocities, Equation 50 is differentiated with respect to time:

$$\frac{d}{dt}\left(R_1 e^{i\eta_1} + R_2 e^{i\eta_2} - R_3 e^{i\eta_3} - R_4 e^{i\eta_4}\right) = 0$$

$$i\dot{\eta}_1 R_1 e^{i\eta_1} + i\dot{\eta}_2 R_2 e^{i\eta_2} + \dot{R}_2 e^{i\eta_2} - \dot{R}_3 e^{i\eta_3} = 0$$

$$i\dot{\eta}_1 R_1 \left(\cos\eta_1 + i\sin\eta_1\right) + i\dot{\eta}_2 R_2 \left(\cos\eta_2 + i\sin\eta_2\right) + \dot{R}_2 \left(\cos\eta_2 + i\sin\eta_2\right) - \dot{R}_3 \left(\cos\eta_3 + i\sin\eta_3\right) = 0$$

Equation 53

The real part of Equation 53 can be rearranged as:

$$-R_1 \dot{\eta}_1 \sin\eta_1 - R_2 \dot{\eta}_2 \sin\eta_2 + \dot{R}_2 \cos\eta_2 - \dot{R}_3 \cos\eta_3 = 0$$

$$-R_1 \dot{\eta}_1 \sin\eta_1 + R_2 \dot{\eta}_1 \cos\eta_1 + \dot{R}_2 \sin\eta_1 - \dot{R}_3 \cos\eta_3 = 0$$

$$R_2 \dot{\eta}_1 \cos\eta_1 + \dot{R}_2 \sin\eta_1 - \dot{R}_3 \cos\eta_3 = R_1 \dot{\eta}_1 \sin\eta_1$$

Equation 54

While the imaginary part Equation 53 is rearranged as:

$$R_1 \dot{\eta}_1 \cos \eta_1 + R_2 \dot{\eta}_2 \cos \eta_2 + \dot{R}_2 \sin \eta_2 - \dot{R}_3 \sin \eta_3 = 0$$
$$R_1 \dot{\eta}_1 \cos \eta_1 + R_2 \dot{\eta}_1 \sin \eta_1 - \dot{R}_2 \cos \eta_1 - \dot{R}_3 \sin \eta_3 = 0$$
$$R_2 \dot{\eta}_1 \sin \eta_1 - \dot{R}_2 \cos \eta_1 - \dot{R}_3 \sin \eta_3 = -R_1 \dot{\eta}_1 \cos \eta_1$$

Equation 55

Combing Equation 51, Equation 52, Equation 54 and Equation 55 in matrix form:

$$
\begin{bmatrix}
\sin \eta_1 & -\cos \eta_3 & 0 & 0 \\
-\cos \eta_1 & -\sin \eta_3 & 0 & 0 \\
\dot{\eta}_1 \cos \theta_1 & 0 & \sin \eta_1 & -\cos \eta_3 \\
\dot{\eta}_1 \sin \theta_1 & 0 & -\cos \eta_1 & -\sin \eta_3
\end{bmatrix}
\begin{bmatrix}
R_2 \\ R_3 \\ \dot{R}_2 \\ \dot{R}_3
\end{bmatrix}
=
\begin{bmatrix}
-R_1 \cos \eta_1 \\
R_4 - R_1 \sin \eta_1 \\
R_1 \dot{\eta}_1 \sin \eta_1 \\
-R_1 \dot{\eta}_1 \cos \eta_1
\end{bmatrix}
$$

Equation 56

Equation 56 can then be solved as:

$$
\begin{bmatrix}
R_2 \\ R_3 \\ \dot{R}_2 \\ \dot{R}_3
\end{bmatrix}
=
\begin{bmatrix}
\dfrac{R_1 \sin(\eta_1 - \eta_3) - R_4 \cos \eta_3}{\cos(\eta_1 - \eta_3)} \\[2mm]
\dfrac{R_1 - R_4 \sin \eta_1}{\cos(\eta_1 - \eta_3)} \\[2mm]
\dfrac{2\dot{\eta}_1 R_1 - \dot{\eta}_1 R_4 \sin \eta_1 - \dot{\eta}_1 R_4 \sin(\eta_1 - 2\eta_3)}{\cos(2\eta_1 - 2\eta_3) + 1} \\[2mm]
\dfrac{2\dot{\eta}_1 R_1 \sin(\eta_1 - \eta_3) - 2\dot{\eta}_1 R_4 \cos \eta_3}{\cos(2\eta_1 - 2\eta_3) + 1}
\end{bmatrix}
$$

Equation 57

Equation 57 thus allows the calculation of the instantaneous measurement position of the laser beam on the MBLEC (R_2) along with it its instantaneous scanning speed $\dot{R}_2$ as functions of the laser beam orientation (defined by $\overline{R}_3$ and $\overline{R}_4$) as well as the rotation angle η_1.

A.2.2 Rigid Body Velocity Component

Inherent to the RC ELDV measurement approach, is the presence of a Rigid Body Velocity Component (RBVC) in the measurements due to the circumferential velocity of the blade. To study this effect, vector-loop calculations are employed yet again. A new vector, $\overline{R}_5$ is defined stretching from the rotation centre to the end of $\overline{R}_2$ as seen in Figure 77:
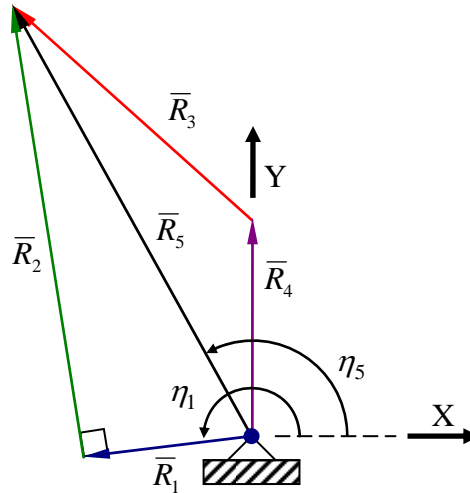
Figure 77: Vector-loop diagram for RBVC calculations

Using the vector-loop, the following relationships are obtained:

$$\overline{R}_5 = \overline{R}_1 + \overline{R}_2 = \overline{R}_3 + \overline{R}_4$$

Equation 58

Solving for the X-components yield :

$$R_5 \cos \eta_5 = R_3 \cos \eta_3$$
$$\cos \eta_5 = \frac{R_3}{R_5} \cos \eta_3$$

Equation 59

while solving for the Y-components give:

$$R_5 \sin \eta_5 = R_3 \sin \eta_3 + R_4$$
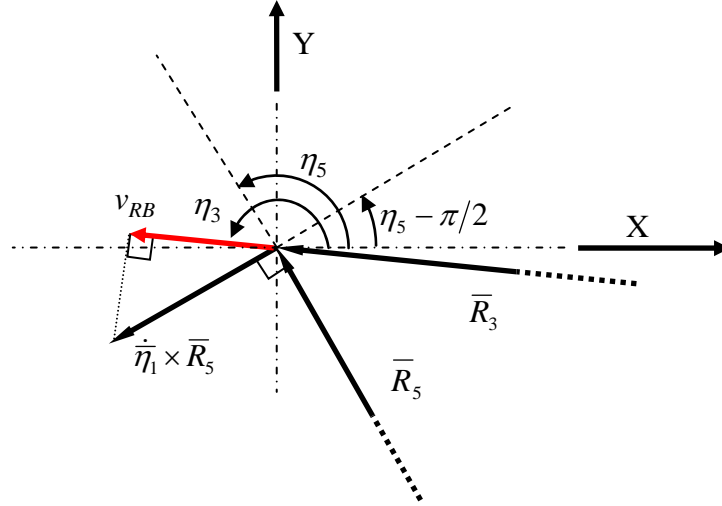$$\sin \eta_5 = \frac{R_3}{R_5} \sin \eta_3 + \frac{R_4}{R_5}$$

Equation 60

Figure 78: RBVC vector definition

Referring to Figure 78, v_{RB} can be calculated as follows:

$$v_{RB} = \dot{\eta}_1 R_5 \cos\left(\eta_5 - 90^o + 180^o - \eta_3\right)$$
$$= \dot{\eta}_1 R_5 \cos\left(\eta_5 - \eta_3 + 90^o\right)$$
$$= \dot{\eta}_1 R_5 \sin\left(\eta_3 - \eta_5\right)$$
$$= \dot{\eta}_1 R_5 \left(\sin\eta_3 \cos\eta_5 - \cos\eta_3 \sin\eta_5\right)$$

Equation 61

Substituting Equation 59 and Equation 60 into Equation 61:

$$v_{RB} = \dot{\eta}_1 R_5 \left(\sin\eta_3 \frac{R_3}{R_5}\cos\eta_3 - \cos\eta_3 \frac{R_3}{R_5}\sin\eta_3 - \cos\eta_3 \frac{R_4}{R_5}\right)$$
$$= -\dot{\eta}_1 R_4 \cos\eta_3$$

Equation 62

Since $\dot{\eta}_1 = 2\pi\psi$ is the rotor speed, v_{RB} can be expressed as:

$$v_{RB} = -2\pi\psi \cdot R_4 \cos\eta_3$$

Equation 63

From Equation 63 is can be deduced that if ψ is constant and the laser beam orientation is fixed, v_{RB} will be constant and will be manifested in the measurements as a DC offset.

A.2.3 The influence of BLEP variance from the MBLEC

The variance of the actual BLEP from the MBLEC will affect the actual instantaneous measurement position as shown in Figure 79, and as a result the scanning speed as well. Also the incidence angle of the laser beam on the surface normal will be affected by the curvature of the BLEP and may thus affect the range of η_1 for which useful measurements can be recorded.

Since v_{RB} is independent of measurement position, it remains unaffected by any variance of the BLEP from the MBLEC.
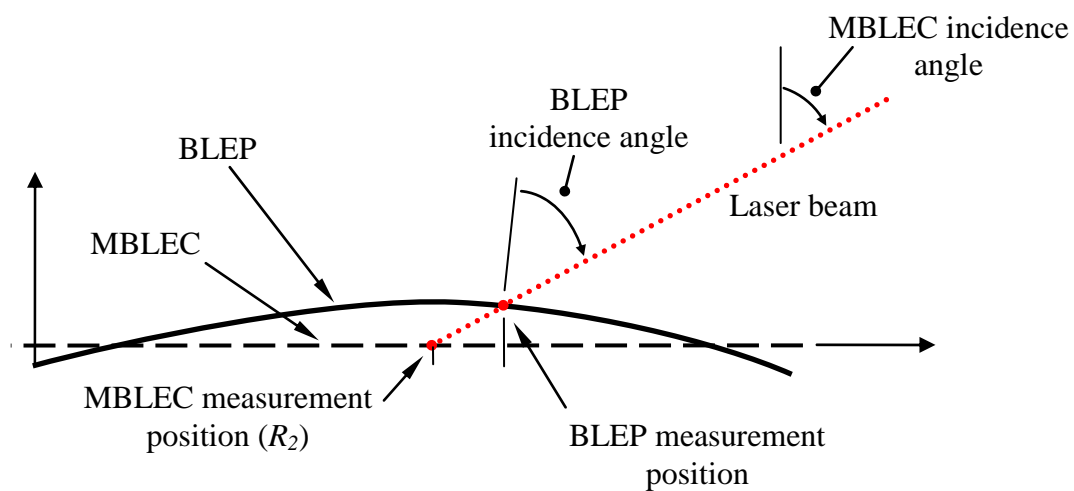

Figure 79: Effect of BLEP variance from MBLEC

A.3 Experimental verification

Figure 80: RC ELDV experimental setup

To verify the equations presented in Section A.2.2, experimental measurements were recorded on the single-blade rotor of Chapter 3. The experimental setup is demonstrated in Figure 80. To obtain the LDV orientation parameters, a tilt sensor was used to measure η_3 as well as the two values of η_2 for which $R_2 = 0.180\,\text{m}$ (i.e. when the blade tip enters and exits the laser beam). These two angles are labelled $\eta_{2,1}$ and $\eta_{2,2}$ respectively as shown in Figure 81. Since $\bar{R}_1$ and $\bar{R}_2$ are perpendicular, $\eta_{1,1}$ and $\eta_{1,2}$ is thus also known at these two positions. R_4 can then be obtained by rearranging the solution for R_2 of Equation 57 as shown in Equation 64 for $\eta_{1,1}$:

$$R_{4,1} = \frac{R_1 \sin(\eta_{1,1} - \eta_3) - R_2 \cos(\eta_{1,1} - \eta_3)}{\cos \eta_3}$$

Equation 64

Setting Equation 64 into Equation 63, v_{RB} can be expressed in terms of m/s/RPM as given for $\eta_{1,1}$:

$$v_{RB,1} = -(2\pi/60) \cdot \left[R_1 \sin(\eta_{1,1} - \eta_3) - R_2 \cos(\eta_{1,1} - \eta_3)\right]$$

Equation 65

The LDV orientation measurements and calculations are summarized in Table 10. Ideally $v_{RB,1}$ and $v_{RB,2}$ should be equal. However due to the resolution of the tilt sensor, $\eta_{2,1}$ and $\eta_{2,2}$ was measured with limited accuracy.
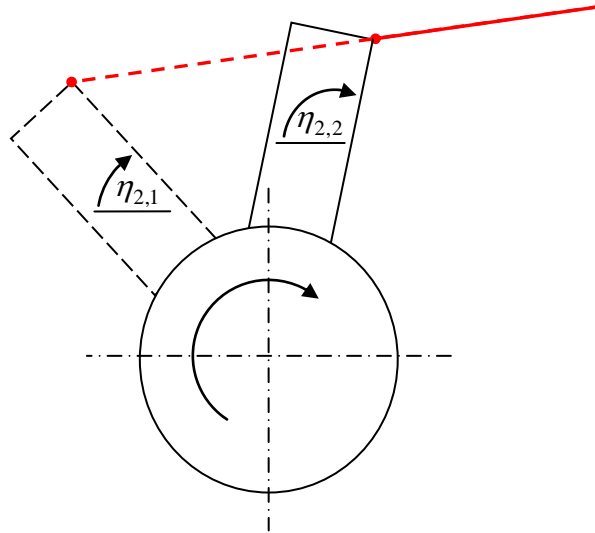

Figure 81: Experimental LDV orientation measurement

Table 10: LDV orientation measurements and calculations

	η_3	[$^{\text{o}}$]	179.0
Position 1	$\eta_{2,1}$	[$^{\text{o}}$]	32.7
	$\eta_{1,1}$	[$^{\text{o}}$]	122.7
	$R_{4,1}$	[m]	0.110
	$v_{RB,1}$	[mm/s/RPM]	11.54
Position 2	$\eta_{2,2}$	[$^{\text{o}}$]	139.1
	$\eta_{1,2}$	[$^{\text{o}}$]	229.1
	$R_{4,2}$	[m]	0.106
	$v_{RB,2}$	[mm/s/RPM]	11.10

RC ELDV measurements were recorded on the blade during rotor run-up to 960 RPM as shown in Figure 82. From this figure a lower limit DC drift can be observed in the measurements. Although the lower limit of the measurements should be at 0 m/s (as seen at the start of the measurement), the LDV measurements start to drift at the lower rotor speeds and settles after about 13 s. This phenomenon is ascribed to the LDV measurement system. Feedback from the OEM was however not available.

To compare the measured and theoretical RBVCs, the experimental measurement range for each blade passage needs to be considered. The results are shown in Figure 83 and errors of 8.9 % and 4.7 % are observed for $v_{RB,1}$ and $v_{RB,2}$ respectively. Via optimization, $v_{RB,opt}$ was obtained as 10.60 mm/s/RPM which indicates angle measurement errors in $\eta_{2,1}$, $\eta_{2,2}$ and η_3 of about 1$^{\text{o}}$. This corresponds to the errors that were measured during verification of the sensor.

From Figure 83, it is seen that a very good correlation exists between the experimental values of v_{RB} and $v_{RB,opt}$ although there is some difference at the lower rotor speeds. This discrepancy however occurs during the non-stationary phase of the measurement lower limit DC drift and is therefore probably a manifestation thereof.
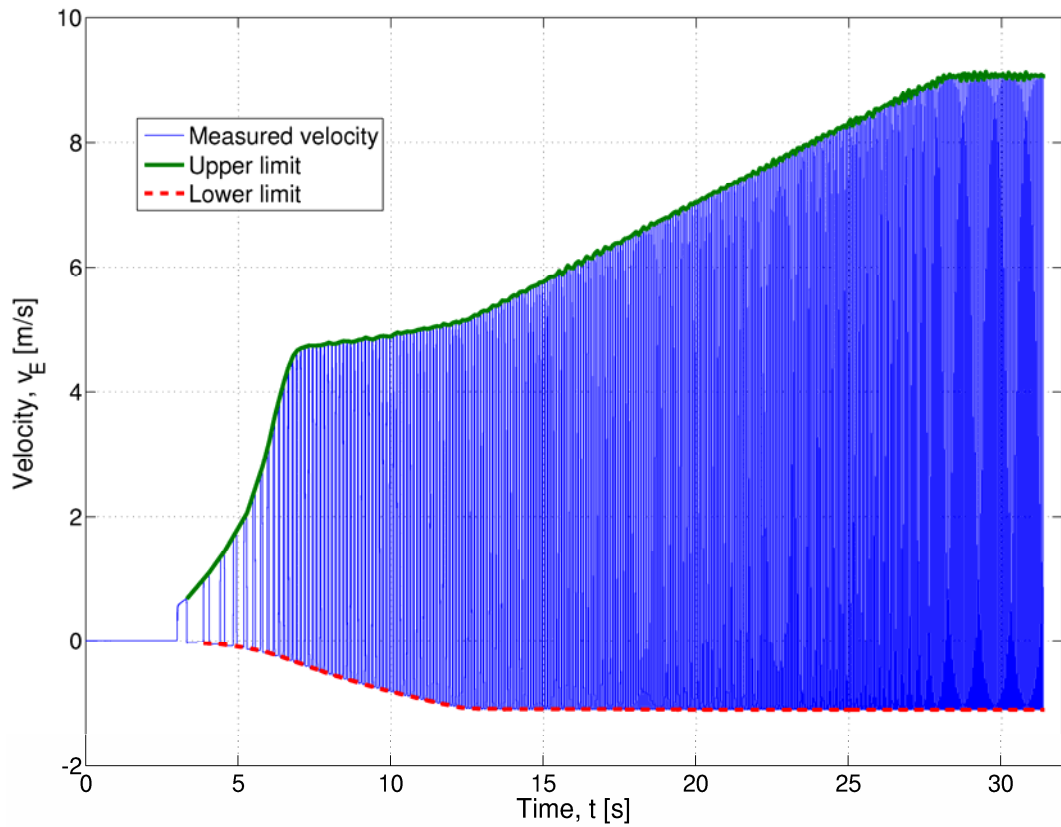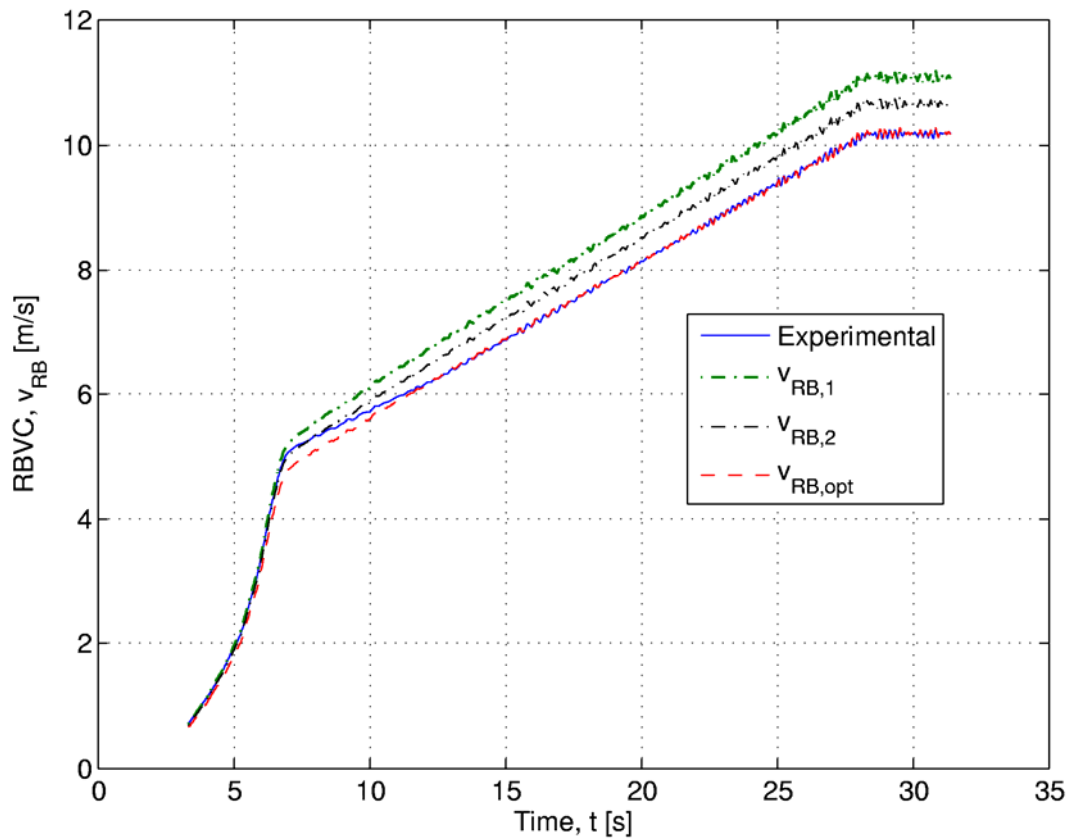
Figure 82: LDV drift

Figure 83: Comparison of measured and theoretical RBVCs

A.4 Response matrix interpolation for non-constant scanning speeds

In Equation 57, it was shown that the scanning speed along the blade edge during a single blade passage not constant:

$$c = \dot{R}_2 = \frac{2\dot{\eta}_1 R_1 - \dot{\eta}_1 R_4 \sin\eta_1 - \dot{\eta}_1 R_4 \sin(\eta_1 - 2\eta_3)}{\cos(2\eta_1 - 2\eta_3) + 1}$$

Equation 66

In Section 2.2.3 it was shown that LVRM interpolation can be successfully employed for constant scanning speeds. To perform this for a non-constant c, one approach is to construct the LVRM with a scan speed ratio $k = 1$ (i.e. $c_{ref} = c = \dot{R}_2$). Another approach is to construct the LVRM for a constant c_{ref} chosen to obtain the required interpolation tolerance.

A.5 Conclusions

In this section, the peculiarities of the RC ELDV measurement approach were studied analytically using the vector-loop method. It was shown that RC ELDV introduces to the measurements a DC offset or RBVC which is directly proportional to the rotor speed. This was verified experimentally.

Observed in the experimental measurements was a lower limit DC drift, which is contributed to the SLDV system. Further work is thus necessary to establish the feasibility of this measurement approach.

The work of this section is presented in the article titled "*On the measurement of circumferential vibration on rotating blades using laser Doppler vibrometry*" (Oberholster and Heyns, In progress).